A STUDY OF FRACTURING AND HEAT TRANSFER IN ENHANCED GEOTHERMAL SYSTEMS

by

Seth Lorenzo Craig

A dissertation submitted to the faculty of
The University of Utah
in partial fulfillment of the requirements for the degree of

Doctor of Philosophy

Department of Mechanical Engineering

The University of Utah

August 2016

The University of Utah Graduate School

STATEMENT OF DISSERTATION APPROVAL

The dissertation of **Seth Lorenzo Craig**

has been approved by the following supervisory committee members:

Kent Udell, Chair **02/29/2016**
Date Approved

Eric Pardyjak, Member **03/14/2016**
Date Approved

Kuan Chen, Member **03/14/2016**
Date Approved

Joseph Moore, Member **03/07/2016**
Date Approved

John McLennan, Member **03/07/2016**
Date Approved

and by **Tim Ameel**, Chair/Dean of

the Department/College/School of **Mechanical Engineering**

and by David B. Kieda, Dean of The Graduate School.

ABSTRACT

Enhanced Geothermal Systems (EGS) have the potential to tap vast amounts of energy. In order to improve EGS functionality, in depth experimental and computational studies of the heat transfer and fracture mechanics of bench top geothermal rock analogs were performed. These experiments contribute to the understanding of hydraulic and thermal fracturing as well as the effects of different heat transfer modes that can be used for heat mining. The work was conducted as follows:

1. Heat transfer rates in a hot dry rock analog containing a circular hole were quantified experimentally and computationally for single-phase fluid flow, and for water vaporization resulting from pore pressure reduction.
2. An experimental examination of hydraulic and thermal fracturing in plane strain was conducted to validate theoretical results and study the fracture morphologies.
3. Thermal fracturing of cement paste, acrylic, and granite was examined experimentally and computationally to understand the role of flaw orientation on resultant fracture geometry in a wellbore.

Proof of concept experiments were performed to evaluate the heat mining potential of a new and innovative way to operate an Enhanced Geothermal System. By injecting water into hot dry rock, allowing it to thermally equilibrate and then dropping the pressure, steam can be produced at a large rate of heat transfer from the rock. This process has a distinct advantage of only needing one well to function. It was found that the steam generation has around 10 times higher heat transfer rates than that of low Peclet number, single phase flow, characteristic of conditions found in the reservoir away from the wellbore and preferential flow pathways.

Experimental work was performed to evaluate the fracture morphology from hydraulic and thermal fractures. One of the purposes of this work was to validate the concept of creating thermal fractures that have faces perpendicular to the maximum horizontal earth stress. The bench top experimental analog was created to study thermal fracturing by uniaxially loading the specimen, thus creating conditions with only one principal stress which is perpendicular to the axis of the hole. Thermal fractures were created and observed with faces that are perpendicular to the maximum principal stress in 3-dimensional specimens for the first time since they were theorized in the 1970s.

Finally a finite difference thermoelastic code with a linear elastic fracture mechanics assessment was created in order to evaluate the effect of various types of heat transfer on the thermal stresses and fracture nucleation potential. It was concluded that the circumferential fractures that were created experimentally in acrylic occurred from flaws that are at least four times larger in that orientation from drilling. In order to create thermal fractures in geologic reservoirs that are perpendicular to the maximum horizontal principal stress, half an order of magnitude larger flaws or preexisting fractures would have to exist in that orientation than features parallel to the maximum horizontal principal stress.

TABLE OF CONTENTS

Chapters

Appendices

LIST OF TABLES

Tables

ACKNOWLEDGMENTS

I would like to thank Dr. Kent Udell, Ph.D. for the seven years of teaching, mentoring, and friendship. I am grateful for the time he has spent advising me. Thank you for reminding us all that life is about also seeking adventure and having fun, a lesson that has sustained me through my graduate career. I would also like to thank Dr. Joseph Moore, Ph.D. and Dr. John McLennan, Ph.D. for funding me for the past six years and obliging many of the ideas that Dr. Udell and I came up with. I appreciate your support through the rough patches. Thank you to Dr. Eric Pardyjak, Ph.D. and Dr. Kuan Chen, Ph.D. I chose you for my committee because you are both great teachers whom I admire.

It is important to note that research is not done in a vacuum. It takes many resources to accomplish large scale experimental work. I would like to start by saying thank you to Mark Bryant and the Civil Engineering Department. Thank you for your advice, help, encouragement, and the use of your lab equipment. A big thank you also is due to Tom Slowik. Thank you for your teaching, advice, and patience. Machining is so relaxing and I am grateful to you for providing a supportive environment to safely try new things and be creative. I would like to thank Jeff Kessler for the various many experimental apparatuses he let me try out over the years. Thank you to Dr. Daniel Adams, Ph.D. for the use of your acoustic equipment. Thank you to Michelle Moore for allowing me to use your time and put a lot of interesting things into your CT scanner. I would like to thank Michael Homel for lending me your computational expertise. The three simple things you pointed out to make my code function I would not have found any other way.

Lastly, I would like to thank Laurel Craig, my dearest wife, best friend, and the best editor anyone could have. Thank you for all of the late nights you took to review this and other papers

over the years; I am a lucky one. Thank you for your love and support through this incredible academic journey with me. I can truly say I would not be where I am today without you. This degree is not mine, rather it is ours. Especially thank you for doing all of this while successfully raising four wonderful children.

CHAPTER 1

GROUND BREAKING RESEARCH IN GEOTHERMAL ENERGY: A LITERATURE REVIEW

1.1 Geothermal Energy

In 1904 electricity was produced from a geothermal system at Larderello, Italy [1]. Since then, substantial research has been done to expand the reach of geothermal technology. Kutcher [2] provides an overview of the operating geothermal power plants in the United States, as well as the current research that is being undertaken to further develop geothermal resources. All current commercial geothermal electrical power plants produce from either water-dominated or vapor-dominated reservoirs. Although hot dry rock or enhanced geothermal systems (EGS) have received research funding for over thirty years, additional research is still needed for their commercial viability [3]. The reason why this type of geothermal energy (from EGS) has been so sought after is because of the sheer magnitude of its potential. Tester et al. [3] reported that 2% of the thermal energy contained within the earth between the depths of 3.5 to 7.5 km "was roughly 2,600 times the annual consumption of electric energy in the United States in 2006."

Geothermal energy is the thermal energy that comes from within the earth. Many consider geothermal energy to be sustainable because it locally accelerates the natural heat flow of the earth. The sustainable capacity of a geothermal power plant is roughly 10% of the natural heat discharge rate of the geothermal system [4]. The reservoir is the in-situ volume of earth that can be accessed for thermal energy extraction. "Reservoir research is aimed at maximizing the production rate and lifetime of the geothermal resource [2]."

Geothermal power plants operate with the same Rankine power cycle components as coal, natural gas, or nuclear power plants. All of these plants have a working fluid that is used to turn the turbine that powers the generator. As seen in Figure 1.1, fluid that exits the turbine goes through a condenser and then is pumped into the heat source to add pressure; the heat source provides enough heat to induce phase change and super heating in the fluid's gas phase. This pressurized and superheated gas is used to turn the turbine, creating work. The cycle then continues.

The major difference between generic power plants (i.e., coal) and geothermal power plants is the method of heat input. For coal and natural gas, combustion of the fuel provides the heat. Nuclear power plants have radioactive material that undergoes fission in a reactor to generate thermal energy. For geothermal power plants, a hot, subsurface reservoir heats the working fluid which is extracted and used with a Binary or Organic Rankine Cycle to enhance the energy production from low-temperature heat sources. A notable exception to the aforementioned cycles is a Steam Flash plant that uses steam from vapor-dominated geothermal reservoirs directly to spin the turbines. Afterwards, cooled water is reinjected into the reservoir to maintain working pressures.

A look at some of the many challenges and inefficiencies faced by energy extraction from geothermal reservoirs can explain why additional research for commercial expansion is still needed. From Figure 1.1, point 3 on the T-s diagram is the highest temperature reached by the working fluid. In traditional power plants, that temperature can be as high as 540°C [5]. Most of the Geysers, the largest exploited geothermal resource in the United States, has a reservoir temperature of ~240°C, and 300°C [6], but rock temperatures as high as 400°C were measured in one area [7]. Most geothermal systems have pressures of 1.03-4.14 MPa (150-600 psi) [8]. Low pressures and temperatures in geothermal reservoirs greatly diminish the quality or enthalpy of the working fluid to produce electrical energy. To accommodate this, as well as to reduce scaling of surface equipment, many geothermal plants inefficiently operate on a binary cycle. A binary cycle has a secondary working fluid that goes through the Vapor Power Cycle, and the geothermal fluid merely heats the working fluid. Another inefficiency can be the additional pumping power that is sometimes needed to inject or recover the geothermal fluid into or from the reservoir. In an ideal Rankine cycle, the pumping power is the rate of energy needed to increase the pressure of the working fluid. While traditional plants have their own inefficiencies, they do not have to overcome the distance and frictional flow loss that the geothermal plants do. In a geothermal scenario, solutions to low temperature and extended distances for fluid movement diminish the overall efficiency of the power plant. This in turn reduces the profit margin, which is necessary for commercial viability. “The performance of reservoir/wellbore systems is perhaps the major cause of uncertainty in geothermal field development decisions, at least in comparison to the performance of surface facilities and power plants.” [9] Geothermal reservoirs are heterogeneous with permeabilities varying laterally and vertically and vary drastically from site to site.

Traditional geothermal reservoirs can be classified as either liquid- or, vapor-dominated. Liquid- dominated systems are the most common. In these systems, liquid water is the convecting medium. “Wells drilled into high temperature liquid-dominated reservoirs (>250°C) typically can produce 5 MW or more of net electric power [10].” According to Woods [10] the average liquid-dominated geothermal system has a permeability of 10^{-12}-10^{-14} m^2 and a porosity of 10^{-2} in a permeable unfractured reservoir. Sometimes higher permeability or surface contact area needs to be created and it has been proposed that this might be accomplished by means of reservoir stimulation (e.g., hydraulic fracturing).

Productive vapor-dominated systems are rare geological volumes with steam filled fractures. Steam is the pressure-controlling medium in the fractures, although liquid water is present in the pores of the rock and along the fracture walls [11]. Vapor-dominated systems have a unique geologic structure made from horizontal layers of permeable and impermeable material that capture water near a heat source, like a magma plume, and then boil the water. The steam travels up but is then restricted by an impermeable cap. Wells in a vapor-dominated system produce dry steam. Consequently, the enthalpies are much higher than for wells producing from liquid-dominated systems. Few vapor-dominated systems are known. The largest are found at The Geysers, CA and Larderello, Italy, The Geysers is the largest geothermal system in the world and generated 1000 MWe in 2003 [6].

Although temperatures suitable for electric generation (> 150-200°C) [12] can be found at great depths, rocks at these depths frequently do not have permeabilities sufficient for exploitation. The creation of conductive fractures by hydraulic fracturing or other means may be required to economically extract the heat. Research is currently underway in the US, Australia, and Europe to develop Enhanced Geothermal Systems (EGS) that can be commercially produced. Once the fracture networks are developed, water can be circulated between the injection and production wells to generate electricity. The next section highlights the essential features of Enhanced Geothermal Systems.

1.2 Enhanced Geothermal Systems (EGS)

While traditional geothermal systems generally have sufficient permeability, fluid, and heat for commercial development, enhanced geothermal systems lack the necessary permeability and fluid. An EGS is essentially an underground heat exchanger. Heat exchangers have two opposing characteristics affecting their performance. These are high flow rate and large surface area. A large surface area creates a large pressure drop that requires higher pumping power to develop higher flow rates. Pumping requirements and development of adequate surface area are challenging to do in enhanced geothermal systems. Even if adequate surface area is developed, it may not be efficiently used. For example, short circuiting is a problem in some geothermal systems. It occurs when the cool injected fluid reaches the production well before it has had time to reheat to reservoir temperatures [13]. Indeed, the major challenge of EGS development is creating an optimal heat exchanger. Ogino and Yamamura [14] concluded that the key to optimizing an EGS reservoir is to maximize the surface area between the injection and production wells.

The major identifying characteristic of an enhanced geothermal system reservoir is the need to be manipulated in some way, in order for it to function adequately for commercial power generation. The general idea is that a deep geothermal reservoir has sufficient heat but lacks the permeability or the flow rate to be effective. Hydraulic fracturing can be used to provide conducive pathways in-situ. Most EGS field projects have used hydraulic fracturing for just this purpose. Fenton Hill and Rosemanowes EGS sites are two examples where hydraulic fracturing was used but created short circuiting along preferential flow pathways [15]. These examples illustrate the challenging nature of reservoir stimulation. It is also important to understand the fracture network to evaluate heat transfer from the resource.

1.3 Heat transfer in Geothermal Systems

Heat extraction from geothermal systems has been studied analytically, numerically and experimentally. Heat transfer varies significantly depending on the reservoir characteristics (e.g. porosity, permeability, rock density, thermal conductivity, specific heat, degree of fracturing, reservoir pressure, and fluid phase). Much of the current EGS research is focused on granite with negligible permeability (below 10^{-17} m^2) [16] [17] but are fractured to allow fluid flow.

1.3.1 Conduction in the Fracture Wall

While calculating conduction through a rock matrix can be quite complicated, it can be done by using the heat conduction equation that is derived from Fourier's Law and the conservation of energy in impermeable material. In order to develop efficient models, several simplifying assumptions are commonly made. When analyzing the heat transfer of an impermeable fractured geothermal system a common assumption made by Bodvarsson [18], Woods [8], Murphy et al. [19], and Pruess and Bodvarsson [13] is that for short times, the only important heat transfer term in the rock matrix is 1-D conduction normal to the fracture face. Kohl et al. [16] modeled the thermal penetration from a fracture face over the lifetime of a reservoir and determined that the 1-D conduction model normal to the fracture face is unsuitable for long time periods. Ghassemi et al. [20] also conducted work on geothermal reservoirs that applies the heat transfer model to fully 3-dimensional geometries.

1.3.2 Double Porosity

Conduction heat transfer in the rock is only part of the system. Advective heat transfer in the flowing fluid presents a more challenging problem. Most research for traditional geothermal reservoirs considers porous media or fractured porous media. To correlate fracture flow with porous media flow, Witherspoon et al. developed the cubic law, which applies Darcy's equation of fluid flow to fractures [21]. This is accomplished by using the equation for flow between two parallel plates and coupling that to Darcy's law. They conducted experiments on samples of granite, basalt, and marble that were fractured under tension [21]. More sophisticated approaches have used dual and triple porosity approaches. The double porosity method is a process by which one can model fractures as porous media with a higher porosity and permeability than that of the unfractured media. This method has been used by Bai and Roegiers [22], Pruess and Narasimhan [17], and Bodvarsson et al. [23]. It was expanded on by Pruess and Wu [24].

1.3.3 Porosity in EGS Reservoirs

Many researchers have studied the heat transfer of geothermal systems to evaluate thermal drawdown (cooling of the reservoir). In general, the drawdown period has presumed a plant life of 30 or more years [25], [26], [27]. Whiting and Ramey developed thermodynamic equations for production from a two-phase, porous geothermal reservoir [28]. They successfully predicted the production history of the Wairakei, New Zealand geothermal field. Robinson and Kruger compared two heat transfer methods for estimating the EGS lifetime at Fenton Hill [29]. The first method was an analytical solution while the second used calculations based on empirical tracer tests [29]. They later published their findings from a long term flow test at Fenton hill that validated the previous calculations [30].

1.3.4 Permeability in EGS Reservoirs

Many early models of EGS reservoirs considered a hydraulically created penny-shaped fracture in impermeable rock that is intersected by two wells. These models assumed that heat transfer in the rock matrix is dominated by conduction normal to the fracture. This is acceptable for short time periods. 2-dimensional flow could be specified into and along the radial fracture. One such analytical model was developed by Heuer et al. [25] for a horizontal fracture. Another model of a vertical hydraulically stimulated penny shaped fracture was published by Murphy et al. [19]. That system was a closed loop. They discovered that after the inlet and outlet wells were installed, further extension of the fractures did not aid the heat transfer process [19].

1.3.5 Boiling in Porous Media

Boiling is a form of heat transfer that entails a phase change from liquid to vapor. This process utilizes both latent (phase change) and sensible (temperature change) forms of energy. During boiling latent energy accounts for more than 95% of the energy transfer [20]. Also, steam (or a two-phase fluid) has a higher enthalpy than a liquid at the same temperature. Significant research has been devoted to boiling in porous media. Woods [7] and Satik [31] have both observed that gravity plays a significant role on boiling in two-phase zones. Pruess et al. [32] as well as Woods and Fitzgerald [33] developed analytical solutions for boiling fronts that form when liquid water is injected into a hot porous reservoir.

1.3.6 Boiling in Impermeable Media

Boiling in fractures in an impermeable media provides added complications for simulation since it is not possible to assume a homogeneous geometry as is commonly done in simplified porous media representations. Due to this difficulty, less research has been conducted on this topic and analytical solutions required to describe the fluid behavior in this environment are more challenging. Moench [34] created a finite difference code to analyze thermal conduction from impermeable blocks in a fractured reservoir during pressure buildup and drawdown. Since this was performed for a vapor dominated system, fluid in the fractures was assumed to consist of steam and liquid. Analytical work by Woods [7] characterized the temperature distribution and location of different phase zones of boiling when water was injected into fractured superheated media. That work was compared to experiments performed by Fitzgerald et al. [35] and Woods et al. [36] who used glass to simulate the walls of the fractures. An important observation of these experiments was the long length of the two phase zone compared to the single phase zones [7]. This is interesting because permeable systems generally have short two phase zones.

Tsypkin and Woods [37] analyzed a similar situation in porous media using similarity solutions to the analytical problem. Their work is unique in that it assumes that the liquid pressure above the boiling pressure of water is present only as a liquid [37]. When the pressure is lowered in a wellbore in an axisymmetric, porous reservoir, boiling commences [37]. The location of the boiling depends on the permeability of the reservoir, which is the main focus of Tsypkin and Woods' [37] work. Wang and Horne [38] developed a boiling heat transfer coefficient for flow in horizontal fractures. To cause radially symmetric flow, a vacuum was induced in a hole in the center of one of two sheets of glass. Wang and Horne [38] concluded that linear functions of relative permeability were the most appropriate for modeling multiphase flow of a liquid and its vapor in a fracture. They also found that the overall boiling heat transfer coefficient for their experiment can most closely be analytically deduced from the work of Chen [39]. Wang and Horne's [38] research is taken further in my dissertation by coupling thermal stresses and a failure criterion with the heat transfer.

1.4 Reservoir Stimulation

When stimulating a reservoir, the primary metric of success is the conductivity of the created fracture network along with the mass flow rate of water or steam that is discharged by the well. Improved deliverability resulting from hydraulic and thermal fracturing is the primary focus of this work.

1.4.1 Rock Fracture Mechanics

Fracture mechanics provide mathematical criteria for forecasting fracture initiation and growth. The induced fracturing in a geothermal reservoir will depend on the in-situ stress conditions, the rock type, preexisting fractures, and the permeability. When rock is stressed micro-cracks develop, which often merge into macroscopic rock fractures [40]. Macroscopic rock fractures or "fractures whose dimensions are much larger than the characteristic grain size of the rock [41]" are of key interest because they form the pathways for high fluid flow.

Predicting fracture initiation and growth requires knowledge of in-situ stress, which can be elusive in a geothermal reservoir. Stress orientations in some geothermal fields are different than the regional stress [42]. What is considered the average or normal stress orientation, with the greatest principal stress being vertical, is common in Basin and Range, and volcanic environments [42]. A strike-slip faulting region has both the greatest and least principal stress regions horizontally oriented [42]. These three regions are the most common geologies for geothermal systems [42]. Hydraulic fractures open with the face being normal to the least principal stress, these typical regions will all produce vertical fractures. According to Sibson [43], geological settings that have a difference between horizontal stresses (or a stress ratio >1), and where the pore fluid pressure is equal to or greater than the least principal stress, will develop a directional permeability in the bearing of maximum horizontal stress [43].

1.4.2 Hydraulic Fracture

Hydraulic fracturing initiates artificial tensile joints by high pressure and high flow rate injection of water into geological media. The final results of a successful hydraulic fracturing are a reservoir with higher permeability, causes higher fracture surface area, and/or a connection to another reservoir, fracture, or well. The primary method to measure a well's connection to the reservoir is by its injectivity or productivity, which is the rate of flow divided by the delivery pressure. Failed hydraulic fracturing is characterized by insufficient deliverability, short circuiting, excessive leak-off, and/or fracture growth to undesirable areas within or outside of the reservoir. Entingh [44] contends that some of the failed hydraulic fracturing projects in geothermal wells are caused by inadequate knowledge about the reservoirs and in-situ fracture geometries. For this reason fracture initiation and geometry are experimentally studied in this dissertation.

Hydraulic fracture initiation or the stress state needed to start a hydraulic fracture has been studied by many researchers, but only a few of the more important will be reviewed here. Haimson and Fairhurst developed a criterion for hydraulic fracture initiation [45]. Presuming elasticity, the state of stress around a wellbore aligned with a principal stress is found by superimposing: (1) the farfield stress and formation pore pressure; (2) the increase in pressure in the wellbore; and (3) the flow of hydraulic fluid (with the same viscosity as the formation fluid) into the formation [45]. The fracture is assumed to initiate once the tensile stress in the rock is greater than the tensile strength of the rock. Equation 1.1 is for an impermeable media [45].

$$P_c = \sigma_t + 3\sigma_{hmin} - \sigma_{Hmax} \tag{1.1}$$

where P_c is the critical pressure in the wellbore, σ_t is the tensile strength of the rock, σ_{hmin} is the least principal stress, and σ_{Hmax} is the maximum horizontal principal stress with compression positive [45]. The fracture initiation criterion developed by Haimson and Fairhurst [43] is one of the most used due to its simplicity. In 1991, Haimson and Zhao [46] evaluated the accuracy of four failure criterion on benchtop hydraulic fracture experiments. They concluded that the point stress criterion, derived by Ito et al. [47], provides the most accurate borehole scale effect calculations. The criterion assumes that the hydraulic fluid is pressurizing an area of the reservoir. This is accomplished by incorporating, T_{hf}, the tensile strength during hydraulic fracture and the radial distance, *d'*, both of which are material properties. For impermeable media the point stress failure criteria is equation 1.2 [47].

$$P_c = \frac{T_{hf}}{I^2} + \frac{\sigma_{Hmax}\left(1-3I^2\right)}{2} + \frac{\sigma_{hmin}\left(1+\frac{2}{I^2}+3I^2\right)}{2} \tag{1.2}$$

where $I = d/(d+2d')$.

Fracture geometry is one of the most important and yet hardest to predict results of geothermal reservoir stimulation. The following research has been conducted in this area. Existing faults, fractures, or joints can prevent the extension of new fracture growth by taking fluid from the growing fracture [48]. This phenomenon was believed to have happened during a hydraulic stimulation of the EGS in Soultz, France by Grecksch et al. [49]. In a 2002 paper by Slevinsky [50], an analytical solution was used to develop an empirical equation in which the flow rate and pressure data are utilized to determine if the well is undergoing fracture lengthening, plugging, or the injection rate was the same as the leak-off rate during reservoir injection. While the reservoir response to injection was calculated, no treatment for geometry or different stress regimes was performed.

Bowie [51] analyzed fracture growth analytically and determined that the stresses negligibly affect the fracture when it is longer than the diameter of the wellbore. Boreholes that are not aligned axially with one of the principal stresses tend to produce features inclined to the far-field principal stresses when hydraulically initiated [52]. These features reorient to an inclination perpendicular to the least principal stress [52]. In a computational study carried out by Min et al. [53], 2-dimensional hydraulic fractures were propagated in homogeneous and heterogeneous sandstones [54]. The Weibull distribution function was used to apply the heterogeneity to the matrix [53]. The fracture geometry that was created in the heterogeneous simulations showed crack branching [53]. This branching however is predominantly in the direction perpendicular to the least principal stress. Min et al. [53] concluded that this branching increases the crack's tortuosity. No quantitative results were reported for the crack geometries or the tortuosity. These works are all very informative but no research has been conducted on the affect of hydraulically fracturing on a well that has been previously thermally fractured.

1.4.3 Thermal Stress

Thermal stresses are caused the rock matrix expanding or contracting in relation to the neighboring rock from thermal gradients. Thermal stresses play a major role in the geothermal reservoir characteristics over time. They can change or create directional permeability, increase or decrease fracture apertures, and even facilitate the creation of new fractures. Thermal stresses strongly depend on the thermal gradients which are controlled by the heat transfer. 2-dimensional conduction analyses by Kohl et al. demonstrated lower thermal stresses since additional mass is encountered for the temperature gradients to diffuse in, as opposed to 1-dimensional conduction [16]. Due to thermal cooling, a compressive stress cage is developed around the active reservoir. According to Kohl [16], this aids production by minimizing far field fluid loss due to a decrease in permeability at the boundary of the cage. In 2005, Ghassemi et al. [54] computationally solved for the thermal stresses in a single fracture in an impermeable reservoir when cold water is injected. They concluded that the thermal stresses would affect the pre-existing fracture aperture favorably by increasing it [54]. In 2008, Ghassemi et al. [55]

created a computational model of an EGS with a single planer fracture that is subjected to poroelastic and thermoelastic stresses. Their model focuses on aperture change from the injection of cold water into a hot reservoir [55]. The aperture change from thermal stresses near the wellbore caused a drop in injectivity [55]. Analytical solutions are also derived for the aperture change from this numerical modeling [55].

1.4.4 Thermal Stress on Hydraulic Fracturing

Hydraulic fracturing results from stress changes that can be induced by hydraulic, thermal, mechanical or chemical initiators. Many researchers have studied the effect of thermal stresses on hydraulic fractures. The works of Slevinsky [50], Gonzalez et al. [56], Nygren and Ghassemi [57], and Perkins and Gonzalez [58] emphasize how thermal stresses change the initiation pressure of hydraulic fractures. The conclusions of these works are fairly similar in that the hydraulic fracture initiation pressure change is approximately the change in tangential stress produced by the thermal stresses. Perkins and Gonzalez also concluded that the hydraulic fracture that initiates at a lower pressure will “stay confined to the low-stress region that lies within the region cooled by the injected fluid [58].” Ghassemi et al. modeled the Coso geothermal field to study the effect of thermal stresses on reservoir performance [20] and concluded that a pre-existing fracture can slip and cause seismicity because of thermal stresses [20]. Clifford et al. developed a code for predicting the size of thermally enhanced hydraulic fractures [59]. The main focus of Clifford, Berry, and Gu was the size of the fracture, using the vertical and horizontal permeabilities as the independent variable [59].

From the previous literature it is evident that any hydraulic fracturing that is caused by pressure and thermal stress is merely initiated at a lower pressure and orients in the same direction as the hydraulic fracture would have under pressure initiation alone. This is especially true if one considers the short time during which thermal gradients grow into the reservoir during a hydraulic stimulation in impermeable media. This dissertation, on the other hand, is centered on the fracture geometries that are created from independent but sequential hydraulic and thermal stimulation.

1.4.5 Thermal Fracturing

Thermal fracturing, caused predominately by thermal stress, is a phenomenon that occurs in geothermal reservoirs from thermal drawdown under low pore pressure conditions. This phenomenon is rarely sought after and scarcely evaluated. It has been theorized to occur in many geothermal fields. When thermal stresses cause sufficient tensile stress in the rock, it fractures. Because the root cause of the fracturing is from temperature differentials and not pressure, it has the potential to create fracture geometries that are different from those created hydraulically.

Theories abound for the creation of secondary thermal fractures on the face of a parent hydraulic fracture. “Creation of the primary crack also produces numerous microcracks perpendicular to the faces of the primary crack. These may grow into secondary cracks as the rock is cooled by heat extraction [60].”

Perkins and Gonzalez [61] theorized that when a hydraulic fracture is cooled a thermal boundary will develop in an elliptical cross section. Within the boundary, if the area is cooled sufficiently a realignment of the stresses can occur [61]. This altered stress state has the potential to create fractures with faces perpendicular to the maximum horizontal principal stress. They created a closed form solution for the stresses in permeable media [61]. Like Perkins and Gonzalez [61], Ghassemi theorizes about thermal fractures being created in the elliptical cooled region [62].

Several computational and a few experimental studies have been performed to clarify thermal fracturing. Tao and Ghassemi [63] considered single phase fluid flow in a matrix comprised of fractures and porous material, using a poro-thermoelastic, displacement discontinuity method. In an injector, the injectivity increased due to thermal contraction of the rock matrix [63]. Tran et al. [64] studied thermal fracturing when cold water is injected into a hot reservoir. They simply used tensile strength as the failure criterion and concluded that “thermal stresses are the dominant cause of secondary fracturing.” They further advocated that these thermally-induced secondary fractures could evolve over short time periods, i.e. several days [64]. Much earlier, Bazant et al. [65] performed a finite element analysis and determined that thermal fracturing in brittle solids will destabilize at certain lengths, and every other crack will stop growing. This process repeats itself in a periodic fashion. This has also been shown to happen in the experimental work of Nemat-Nasser [60]. In work similar to that performed by Nemat-Nasser, Finnie et al. [66] analytically and experimentally studied exposure of a semi-infinite rock surface to liquid nitrogen. Since Finnie et al. [66] were evaluating surface mining, stress-free boundary conditions were assumed. Due to the low heat transfer rates of film boiling and the unpredictability of fracture geometry, the technique was not found to be economically feasible for rock mining [66].

A few long term field test results have demonstrated the in-situ creation of thermal fractures. Tester et al. analyzed a prototype EGS, Fenton Hill, and concluded that thermal fractures were the likely cause of the shallower than expected thermal drawdown [67]. Bruel [68] computationally analyzed the results of a four month long experiment done at the EGS site at Soultz sous Foret, France. Bruel [68] concluded that thermal fracturing lowered injection pressures and was significant enough that it should be included in future work on EGS reservoirs. Bradford et al. [69] conducted a thermal stimulation at the Raft River, ID EGS site and concluded that the injectivity of the stimulated well increased during the test.

1.5 Adding to the Body of Scientific Research

This dissertation evaluates heat extraction from geothermal systems occurring by boiling a fluid in the reservoir through depressurization. Conduction is considered to be the only significant form of heat transfer in the rock matrix. Fluid flow is restricted to induced fractures and the fluid is considered to be single phase and comprised of a single componant. Experiments were carried out to determine the fracture geometries that form as a consequence of thermal stressing induced by cooling the reservoir.

Significant research has been done in the field of geothermal energy. Heat transfer, stress mechanics, and fracture growth have all been studied to great success analytically, computationally and experimentally. However, there is still a need in some key areas to understand more about the phenomenon’s that occur deep in the earth where observation is difficult. Tester stated: “Specifically, it is largely unknown how thermal contraction caused by local cooling of the rock at and near fracture channels affects fluid losses and dynamic fracture propagation [70].” This illustrates the need for added research in thermal fracture morphology. Wang and Horne’s [38] research is taken further in my dissertation, as well, by coupling thermal stresses and a failure criterion with the heat transfer. Entingh [44] contends that some of the failed hydraulic fracturing projects in geothermal wells are caused by inadequate knowledge about the reservoirs and in-situ fracture geometries. For this reason fracture initiation and geometry are experimentally studied in this dissertation.

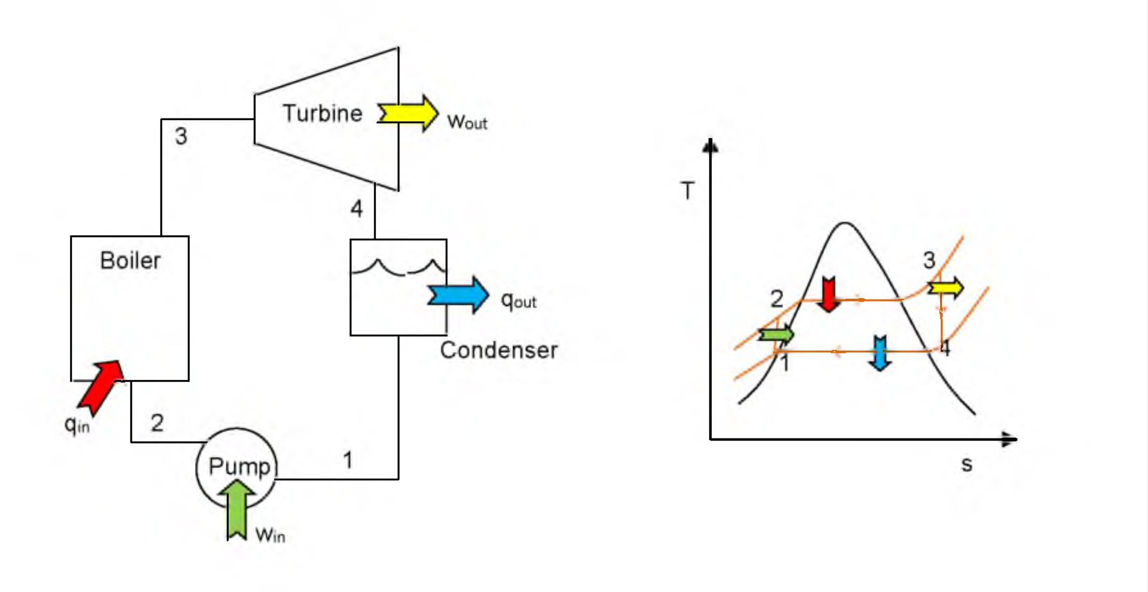

Figure 1.1: Left is a physical schematic and right is a temperature (T) entropy (s) diagram for a simplified ideal Rankine vapor cycle using water as the working fluid. The defining heat source for the power plant is q_{in}. W_{in} is the work energy needed to power the pump, W_{out} is the work energy extracted by the turbine, and q_{out} is the heat taken out of the system by the condenser.

1.6 References

[1] Lund, J.W., 2004, “100 Years of Geothermal Power Production,” GHC Bulletin, September, pp. 11-19.

[2] Kutscher, C.F., 2000 , “The Status and Future of Geothermal Electric Power,” *The American Solar Energy Society (ASES) Conference Report*, Madison, WI, pp. 1-6.

[3] MIT, 2006. The Future of Geothermal Energy. Impact of Enhanced Geothermal Systems (EGS) on the United States in the 21st Century. Assessment by a Massachusetts Institute of Technology-led interdisciplinary panel (J.F. Tester, Chairman), 372 from http://geothermal.inel.gov/publications/future_of_geothermal_energy.pdf

[4] Sanyal, S.K., 2005, “Sustainability and Renewability of Geothermal Power Capacity,” *Proc. World Geothermal Congress*, Antalya, Turkey, pp. 1-13.

[5] El-Wakil, M.M., 1984, *Powerplant Technology*, McGraw-Hill, San Francisco, pp. 38, Chap. 2.

[6] Lowenstern, J.B. and Janik, C.J., 2003, The origins of reservoir liquids and vapors from The Geysers geothermal field, California (USA), *in* S. F. Simmons and I. Graham (ed). Volcanic, geothermal and ore-forming fluids: Rulers and witnesses of processes within the Earth: Society of Economic Geologists Special Publication 10, p. 181-195.

[7] Lutz, S.J., Walters, M., Pistone, S., and Moore, J.N., 2012, “New Insights Into the High-Temperature Reservoir, Northwest Geysers,” *GRC Transactions*, Geothermal Resource Council, **36**, pp. 907-916.

[8] Woods, A.W., 1999, “Liquid and Vapor Flow in Superheated Rock,” Annu. Rev. Fluid Mech., **31**, pp. 171-199

[9] Gudmundsson, J.S., and Marcou, J.A., 1986, “Deliverability and its Effect on Geothermal Power Costs,” *Proc. 11th Stanford Geothermal Workshop*, Stanford University, Stanford, pp. 217-222.

[10] MIT, 2006. The future of Geothermal Energy. Impact of Enhanced Geothermal Systems (EGS) on the United States in the 21st Century. Assessment by a Massachusetts Institute of Technology-led interdisciplinary panel (J.F. Tester, Chairman), 372 pp.5-3 from http://geothermal.inel.gov/publications/future_of_geothermal_energy.pdf

[11] White, K.E., Muffler, L.J.P., and Truesdell, A.H., 1971, “Vapor-Dominated Hydrothermal Systems Compared with Hot-Water Systems,” Econ. Geo., **66**, pp. 75-97.

[12] MIT, 2006. The future of Geothermal Energy. Impact of Enhanced Geothermal Systems (EGS) on the United States in the 21st Century. Assessment by a Massachusetts Institute of Technology-led interdisciplinary panel (J.F. Tester, Chairman), 372 pp.1-15 from http://geothermal.inel.gov/publications/future_of_geothermal_energy.pdf

[13] Pruess, K., and Bodvarsson, G.S., 1984, “Thermal Effects of Reinjection in Geothermal Reservoirs With Major Vertical Fractures,” J. Petroleum Tech., **36**(9), pp. 1567-1578.

[14] Ogino, F., and Yamamura, M., 1998, “Pressure Drop of Water Flow Between Injection and Production Wells Intersected by a Circular Fracture,” Geothermics, **27**(1), pp. 25-41.

[15] MIT, 2006. The future of Geothermal Energy. Impact of Enhanced Geothermal Systems (EGS) on the United States in the 21st Century. Assessment by a Massachusetts Institute of Technology-led interdisciplinary panel (J.F. Tester, Chairman), 372 from http://geothermal.inel.gov/publications/future_of_geothermal_energy.pdf

[16] Kohl, T., Evans, K.F., Hopkirk, R.J., and Rybach, L., 1995, “Coupled Hydraulic, Thermal and Mechanical Considerations for the Simulation of Hot Dry Rock Reservoirs,” Geothermics, **24**, (3), pp. 345-359.

[17] Pruess, K., Narasimhan, T.N., 1985, “A Practical Method for Modeling Fluid and Heat Flow in Fractured Porous Media,” SPE J., **25**(1), pp. 14-26.

[18] Bodvarsson, G., 1969, “On the Temperature of Water Flowing Through Fractures,” J. Geophys. Res., **74**(8), pp. 1987-1992.

[19] Murphy, H.D., Tester, J.W., Grigsby, C.O., and Potter, R.M., 1981, “Energy Extraction From Fractured Geothermal Reservoirs in Low-Permeability Crystalline Rock,” J. Geophysical Res., **86**(B8), pp. 7145-7158.

[20] Ghassemi, A., Tarasovs, S., and Cheng, A.H.-D., 2007, “A 3-D Study of the Effects of Thermomechanical Loads on Fracture Slip in Enhanced Geothermal Reservoirs,” Int. J. Rock Mech. Mining Sci., **44**, pp. 1132-1148.

[21] Witherspoon, P.A., Wang, J.S.Y., Iwai, K., and Gale, J.E., 1980, “Validity of Cubic Law for Fluid Flow in a Deformable Rock Fracture,” Water Resour. Res., **16**(6), pp. 1016-1024.

[22] Bai, M., Roegiers, J.C., 1994, “Fluid Flow and Heat Flow in Deformable Fractured Porous Media,” Int. J. Eng. Sci., **32**(10), pp. 1615-1633.

[23] Bodvarsson, G.S., Pruess, K., O’Sullivan, M.J., 1985, “Injection and Energy Recovery in Fractured Geothermal Reservoirs,” SPE J., **25**(2), pp. 303-312.

[24] Pruess, K., Wu, Y., 1993, “A New Semi-Analytical Method for Numerical Simulation of Fluid and Heat Flow in Fractured Reservoirs,” SPE Advanced Technology Series, **1**(2), pp. 63-72.

[25] Heuer, N., Küpper, T., and Windelberg, D., 1991, “Mathematical Model of a Hot Dry Rcok System,” Geophys. J. Int., 105, pp. 659-664.

[26] Kolditz, O., 1995, “Modelling Flow and Heat Transfer in Fractured Rocks: Conceptual Model of a 3-D Deterministic Fracture Network,” Geothermics, **24**(3), pp. 451-470.

[27] Kolditz, O., Clauser, C., 1998, “Numerical Simulation of Flow and Heat Transfer in Fractured Crystalline Rocks: Application to the Hot Dry Rock Site in Rosemanowes (U.K.),” Geothermics, **27**(1), pp. 1-23.

[28] Whiting, R.L., Ramey, H.J. Jr., 1969, “Application of Material and Energy Balances to Geothermal Steam Production,” J. Petroleum Tech., **21**(7), pp. 893-900.

[29] Robinson, B.A., Kruger, P., 1988, “A Comparison of Two Heat Transfer Models for Estimating Thermal Drawdown in Hot Dry Rock Reservoirs,” *Proc. 13th Stanford Geothermal Workshop*, Stanford University, Stanford, pp. 113-120.

[30] Kruger, P., Robinson, B., 1994, “Heat Extracted From the Long Term Flow Test in the Fenton Hill HDR Reservoir,” *Proc. 19th Stanford Geothermal Workshop*, Stanford University, Stanford, pp. 51-56.

[31] Satik, C., 1997, “Experiments of Boiling in Porous Media,” *Proc. 22nd Stanford Geothermal Workshop*, Stanford University, Stanford, pp. 343-350.

[32] Pruess, K., Calore, C., Celati, R., and Wu, Y.S., 1987, “An Analytical Solution for Heat Transfer at a Boiling Front Moving Through a Porous Medium,” Int. J. Heat Mass Transfer, **30**(12), pp. 2595-2602.

[33] Woods, A.W., Fitzgerald, S.D., 1997, “The Vaporization of a Liquid Front Moving Through a Hot Porous Rock. Part 2. Slow Injection,” J. Fluid Mech., **3443**, pp. 303-316.

[34] Moench, A.F., 1978, “The Effect of Thermal Conduction upon Pressure Drawdown and Buildup in Fissured, Vapor-Dominated Geothermal Reservoirs,” *Proc. 3rd Stanford Geothermal Workshop*, Stanford University, Stanford, pp. 112-117.

[35] Fitzgerald, S.D., Pruess, K., van Rappard, D.M., 1996, “Laboratory Studies of Injection into Horizontal Fractures,” *Proc. 21st Stanford Geothermal Workshop*, Stanford University, Stanford, pp. 113-118.

[36] Woods, A.W., Fitzgerald, S.D., Wang, C., 1998, “The Vaporization of Liquid Injected into a Fracture Bounded by Superheated Rock,” *Proc. 23rd Stanford Geothermal Workshop*, Stanford University, Stanford, pp. 176-179.

[37] Tsypkin, G.G., and Woods, A.W., 2004, “Vapour Extraction from a Water-Saturated Geothermal Reservoir,” J. Fluid Mech., **506**, pp. 315-330.

[38] Wang, C.T., Horne, R.N., 2000, “Boiling Flow in a Horizontal Fracture,” Geothermics, **29**, pp. 759-772.

[39] Chen, J.C., 1966, “Correlation for Boiling Heat Transfer to Saturated Liquids in Convective Flow,” Ind. Eng. Chem., Process Design Dev., **5**(3), pp. 322-329.

[40] Pellet, F.L., Keshavarz, M., and Amini-Hosseini, K., 2011, “Mechanical Damage of a Crystalline Rock Having Experienced Ultra High Deviatoric Stress up to 1.7 GPa,” Int. J. Rock Mech. Mining Sci., doi: 10.1016/j.ijrmms.2011.09.006.

[41] Mandi, G., 2005*, Rock Joints: The Mechanical Genesis*, Springer, New York, Chap. 1.

[42] Nielson, D.L., 1989, “Stress in Geothermal Systems,” *Transactions GRC*, **13**, pp. 271-276.

[43] Sibson, R.H., 1996, “Structural Permeability of Fluid-Driven Fault-Fracture Meshes,” J. Struct. Geo., **18**, (8), pp. 1031-1042.

[44] Entingh, D.J., 2000, “Geothermal Well Stimulation Experiments in the United States,” *World Geothermal Congress 2000*, Kyushu – Tohoku, Japan, pp. 3689-3694.

[45] Haimson, B., and Fairhurst, C., 1967, “Initiation and Extension of Hydraulic Fractures in Rocks,” SPE J., pp. 310-318.

[46] Haimson, B.C., and Zhao, Z., 1991, “Effect of Borehole Size and Pressurization Rate on Hydraulic Fracturing Breakdown Pressure,” Rock Mech. Multidiscip. Sci., pp. 191-199.

[47] Ito, T., Hayashi, K., and Abe, H., 1990, “Scale Effect in Breakdown Pressure of Hydraulic Fracturing Stress Measurements,” Scale Effects Rock Mass., pp. 289-294.

[48] Tenzer, H., 2001, “Development of Hot Dry Rock Technology,” GHC Bulletin, December, pp. 14-22.

[49] Grecksch, G., Jung, R., Tischner, T., and Weidler, R., 2003, “Hydraulic Fracturing at the European HDR/HFR Test Site Soultz-sous-Forets (France) – a Conceptual Model,” *Proc. European Geo. Conf.*, Szeged, Hundary, pp.1-8.

[50] Slevinsky, B.A., 2002, “A Model for Analysis of Injection-Well Thermal Fractures,” SPE 77568, *Proc. SPE*, San Antonio, pp. 1-9.

[51] Bowie, O.L., 1956, “Analysis of an Infinite Plate Containing Radial Cracks Originating at the Boundary of an Internal Circular Hole,” J. Math. Phy., **35**, pp. 60-71.

[52] Daneshy, A.A., 1973, “A Study of Inclined Hydraulic Fractures,” SPE Journal, pp. 61-68.

[53] Min, K.S., Zhang, Z., and Ghassemi, A., 2010, “Hydraulic Fracturing Propagation in Heterogeneous Rock Using the VMIB Method,” *Proc. 35th Stanford Geothermal Workshop,* Stanford University, Stanford, pp. 230-239.

[54] Ghassemi, A., Tarasovs, S., and Cheng, A.H.-D., 2005, “Integral Equation Solution of Heat Extraction-Induced Thermal Stress in Enhanced Geothermal Reservoirs,” Int. J. Numer. Anal. Meth. Geomech., **29**, pp. 829-844.

[55] Ghassemi, A., Nygren, A., Cheng, A., 2008, “Effects of Heat Extraction on Fracture Aperture: A Poro-Thermoelastic Analysis,” Geothermics, **37**, pp. 525-539.

[56] Gonzalez, M.E., Bloys, J.B., Lofton, J.E., Pepin, G.P., Schmidt, J.H., Naquin, C.J., Ellis, S.T., Laursen, P.E., 2004, “Increasing Effective Fracture Gradients by Managing Wellbore Temperatures,” 87217, *IADC/SPE Drilling Conference*, *Proc. SPE*, Dallas, pp. 1-14.

[57] Nygren, A., Ghassemi, A., 2005, “Influence of Cold Water Injection on Critically Stressed Fractures in Coso Geothermal Field, CA,” 05-727, Alaska Rocks 2005, The 40th USRMS, ARMA, Anchorage, pp. 1-8.

[58] Perkins, T.K., and Gonzalez, J.A., 1984, “Changes in Earth Stresses Around a Wellbore Caused by Radially Symmetrical Pressure and Temperature Gradients,” J. SPE, **24**(2), pp. 129-140.

[59] Clifford, P.J., Berry, P.J., Gu, H., 1991, “Modeling the Vertical Confinement of Injection-Well Thermal Fractures,” SPE Prod. Eng., **Nov.**, pp. 377-383.

[60] Nemat-Nasser, S., 1983, “Thermally Induced Cracks and Heat Extraction From Hot Dry Rocks,” Hyd. Frac. Geotherm. Energy Mech. Elastic Inelastic Solids, **5**, pp. 11-31.

[61] Perkins, T.K., and Gonzalez, J.A., 1985, “The Effect of Thermoelastic Stresses on Injection Well Fracturing,” J. SPE, **25**(1), pp. 78-88.

[62] Ghassemi, A., 2007, “Stress and Pore Pressure Distribution Around a Pressurized, Cooled Crack in Low Permeability Rock,” *Proc. 32nd Stanford Geothermal Workshop*, Stanford University, Stanford, pp. 1-7.

[63] Tao, Q., and Ghassemi, A., 2010, “Simulation of Fluid Flow in Fractured Poro-Thermoelastic Reservoirs,” *Proc. 35th Stanford Geothermal Workshop*, Stanford University, Stanford, pp. 105-111.

[64] Tran, D., Settari, A., and Nghiem, L., 2012, “Initiation and Propagation of Secondary Cracks in Thermo-Poroelastic Media,” *46th US Rock Mechanics/Geomechanics Symposium*, Chicago, ARMA 12-252, pp. 1-11.

[65] Bazant, Z.P., Ohtsubo, H., and Aoh, K., 1979, “Stability and Post-Critical Growth of a System of Cooling or Shrinkage Cracks,” Int. J. Fracture, **15**(5), pp. 443-456.

[66] Finnie, I., Cooper, G.A., Berlie, J., 1979, “Fracture Propagation in Rock by Transient Cooling,” Int. J. Rock Mech. Min. Sci. Geomech., **16**, pp. 11-21.

[67] Tester, J.W., Murphy, H.D., Grigsby, C.O., Potter, R.M., and Robinson, B.A., 1989, “Fractured Geothermal Reservoir Growth Induced by Heat Extraction,” SPE Res. Eng., pp. 97-104.

[68] Bruel, D., 2002, “Impact of Induced Thermal Stresses During Circulation Tests in an Engineered Fractured Geothermal Reservoir,” Oil Gas Sci. Tech., **57**(5), pp. 459-470.

[69] Bradford, J., Ohren, M., Osborn, W.L., McLennan, J., Moore, J., Podgorney, R., 2014, “Thermal Stimulation and Injectivity Testing at Raft River, ID EGS Site,” *39th Stanford Geothermal Workshop*, Stanford University, Stanford, pp. 1-9.

[70] MIT, 2006. The future of Geothermal Energy. Impact of Enhanced Geothermal Systems (EGS) on the United States in the 21st Century. Assessment by a Massachusetts Institute of Technology-led interdisciplinary panel (J.F. Tester, Chairman), 372 pp. 5-10. <http://geothermal.inel.gov/publications/future_of_geothermal_energy.pdf>

CHAPTER 2

ENHANCED HEAT TRANSFER FROM GEOTHERMAL SYSTEMS USING PRESSURE CYCLING: A THEORIZED SINGLE WELLBORE EGS

2.1 Abstract

Energy found in the earth's crust as heat can be extracted through a network of fractures carrying a working fluid in a process termed Enhanced Geothermal Systems (EGS). Harnessing that energy to produce electricity will require significant heat transfer from the rock to the working fluid. This research examines the possible enhancement of the heat transfer at locations in the reservoir removed from the wellbore and preferential flow pathways using a bench-top experiment simulating a single flow-path in hot rock. Analytical and computational models are also utilized to better understand the transient heat transfer process and ascertain deterministic variables.

The bench-top laboratory experiment consisted of a mortar cylinder with a small hole (6.35 mm) along the axis, and thermocouples embedded at four radial locations. Heat transfer from the simulated hot dry rock (SHDR) to the liquid water flowing through the hole was first evaluated to assess the heat transfer analogous to flow through a connected fracture. Experiments were then rerun under conditions where depressurizing the water resulted in the production of steam. It was found that depressurization heat transfer rates are an order of magnitude higher than typical Peclet number (0-5) single phase flow heat rates in geothermal reservoirs. For the single phase flow experiments the axial distance to the location where the fluid temperature matches the initial mortar temperature limits the heat transfer, whereas the limit for depressurization heat transfer is either the mass of water in the void volume or the thermal

conduction from the SHDR. These results imply that the rate of production of energy from some geothermal systems might be dramatically improved if operated cyclically with respect to pressure inducing flashing.

2.2 Introduction

The necessity of clean energy can be clearly seen in the beautiful smoggy sunsets of every metropolitan city. This need drives the quest for new and innovative ways of obtaining the heat needed for electrical energy production and geothermal energy answers that call.

Enhanced geothermal systems require inter-well connectivity of injection and production wells. The elimination of well connectivity would aid the growth of the geothermal industry as the percentage of “nonproducing wells” is dramatically decreased. One approach to eliminating the need for inter-well connectivity is as follows. First, inject high-pressure water into a single well to open fractures and distribute the water phase throughout the fracture network. After the water comes to thermal equilibrium with the surrounding hot dry rock, the pressure is lowered to generate steam throughout the fracture volume. This can be considered a reverse “Huff and Puff” system. Johnson [1] concluded in his research that approximately 40% of the liquid water will flash as a result of the drop in pressure and the thermal energy stored in the water. In order for complete vaporization to occur, thermal energy must be transferred from the rock matrix to the water [1]. The vaporization and cooling of the rock will continue until all the water is gone or until the rock surface temperature is below the boiling point of the water at local pressure. It is hypothesized that enhanced heat transfer rates can be obtained from a single wellbore EGS through vaporization caused by pressure cycling compared to an identical system with single phase flow.

Precipitation of dissolved minerals during the water vaporization process in the single wellbore systems described above may be a concern. It is expected that as the saturation and vaporization of the reservoir undergoes many cycles some minerals will dissolve into the water phase. These minerals will then precipitate when vaporization occurs. Depending on the movement of the high mineral content water, precipitation could cause a decrease in reservoir performance, this is known as scaling. Proper management of the system “may insure that the flashing zone moves abruptly from the wellbore to a position remote from the wellbore where deposition is not detrimental [1].” Johnson continues to explain that as the boiling occurs and the rock cools an elongated flashing front will form [1]. Any dissolved minerals would precipitate at the fracture face as the water evaporates. Thus, scaling in the wellbore would not be expected because the vaporization will occur away from the well along the elongated flashing front. Thermal fracturing will also help to counteract the effects of scaling. As the reservoir cools, the rock will shrink and crack, creating new fluid pathways. Thermal fracturing was shown to have positive effects on the reservoir in this regard by Sigurdsson et al., Tester et al., Perkins and Gonzalez, and Barr [2-5].

Note that no inter-well connectivity would be needed to facilitate the energy production from the single well EGS. Thus, it is not susceptible to preferential flow pathways or short circuiting. Preferential flow pathways occur due to heterogeneity [6] and are the cause of premature thermal breakthrough. They drastically influence fluid flow and reduce heat transfer. The volume of these preferential channels can be orders of magnitude smaller than the total void volume and are a well-known issue [7] [8]. Preferential flow pathways are reported by Grant and Garg [9] to be responsible for the low recovery factor in the Cooper Basin EGS in Australia. The recovery factor is the total heat extracted from the production well divided by the total heat in the reservoir. Acoustic emissions from Cooper Basin determined a reservoir size that was used with standard models that assume equal fracture spacing to find a recovery factor of 50-70%. Grant and Garg [9] used Tracer Sweep Data and determined a more accurate recovery factor of 1.6%. The steady fluid flow and preferential flow pathways are generated by the pressure differential between the injection and production wells. A single wellbore system has the advantage of accessing a higher volume of the reservoir by “diffusing,” increasing and decreasing pressures, radially from one well.

This type of system would also have great load-following potential. As demonstrated by a field experiment done by Brown, EGSs have rapid response times to electric load by dropping the production pressure [10]. Further, in addition to increasing the heat transfer, daily cyclic modes of operation might match the operation of a solar thermal plant, either by complimenting the power production during the night or as a mode of energy storage. Such synergy might be found at a location near Milford, Utah, where both solar and geothermal resources coexist.

This paper describes an experimental and numerical study of the possible heat transfer rates from reservoirs using pressure cycles to cause vaporization compared to the heat transfer that may be expected during typical cold water injection, hot water extraction thermal energy recovery processes. For the bench-top laboratory experiment, mortar was used as a medium to emulate hot dry rock. The mixture consists of small aggregate (sand), cement, water, and silica fume to make the final product as impermeable and homogeneous as possible. The shape of the simulated hot dry rock (SHDR) was cylindrical with a concentric small hole (6.35 mm) along the axis. The thermal conductivity was inferred using a temperature buildup and drawdown method developed by Carslaw and Jaeger [11]. The SHDR was then used to run experiments after being heated in an oven. Heat transfer from the SHDR to the liquid water flowing through the hole was first evaluated to assess the heat transfer similar to that found in flow through a connected fracture network. Experiments were then rerun under conditions where depressurizing the water resulted in the production of steam. A new application of the Thermal Build-Up Method outlined by Jaeger [12] was used to find the heat transfer rate of steam production when the thermal conductivity of the SHDR material is known. The numerical simulation involved the solution of the fluid and heat equations using an explicit 2-dimensional finite difference model. The model simulates axisymmetric heat transfer in the r-z plane with coupled heat transfer between the solid and the fluid flowing in the central hole. Through these simulations dominant parameters determining the heat transfer and thermal energy recovery are identified. Thermal penetration is also studied by comparing three working fluids. The thermal properties are found at in-situ conditions for Raft River geothermal field. The Raft River geothermal field has an Elba Quartzite reservoir and is the subject of current studies on heat transfer and fracture mechanics. Part of this research was funded by the U.S. Department of Energy to study the Raft River reservoir.

2.3 Experimental and Computational Materials and Methods

2.3.1 Experimental Methodology

A benchtop laboratory experiment was constructed to emulate a single flow path in hot rock. The experiment consisted of a 30 cm radius, 30 cm long mortar cylinder with a concentric small hole (6.35 mm) along the axis. Sheathed T-type thermocouples were imbedded at four radial locations. In order to produce a homogeneous media, no large aggregate was used. Silica fume was mixed with the small aggregate (sand), cement and water to make the mortar as impermeable as possible. The mortar was wet cured for 3 weeks then allowed to dry cure for a month. Thermocouple arrangements and physical dimensions of the experiment are in Figure 2.1. An epoxy-phenolic tank lining (Amercoat 90HS) was applied to the outside surfaces of the cylinder to reduce air infiltration. Exterior cracks that later formed from cyclic heating and pressurization were sealed using epoxy anchoring adhesive.

An identical composition mortar sample, roughly 0.1 m in diameter by 0.2 m in height, was fabricated for thermal property testing. The density was calculated from the mass and cylindrical dimensions. The specific heat was found by heating the sample, placing it in a beaker of water, then observing the temperature change in a well-insulated box. The initial temperatures of the cylinder and water, and then the final temperature once the water and cylinder came to thermal equilibrium, were used to calculate the specific heat. All other fluid and solid properties used for calculations came from The Thermophysical Properties of Matter Data Series [13].

The thermal conductivity of the mortar used in the flow experiments was inferred using the temperature build up and drawdown method developed by Jaeger [12]. In this method transient temperature measurements near a cartridge heater were used. The technique is similar to that practiced using pressure buildup and drawdown data for in-situ permeability measurements and those practiced by Jaeger, Carslaw and Jaeger, and Xu et al. [12, 11, 14]. A cartridge heater with nominally the same diameter as the central hole in the cylinder was used as the constant power source for the experiment. The thermocouples were connected to an Omega-3000 Portable Datalogger. The electrical resistance of the cartridge heater measured before the experiment was 77.6 ohms. The alternating current voltage of the outlet was also measured to be 119 volts. The calculation to find the thermal conductivity of the mortar cylinder is derived from governing equation 2.1 and boundary and initial conditions found in equations 2.2, 2.3, and 2.4, respectively. This solution is for a semi-infinite cylinder with a line heat source at $r = 0$. It is a 1-dimensional problem in the radial direction. Equation 2.2 is the semi-infinite boundary condition. Equation 2.3 is the line heat source, represented physically by the cartridge heater. Equation 2.4 is the initial condition.

$$\frac{1}{r}\frac{\partial\left(r\frac{\partial T}{\partial r}\right)}{\partial r} = \frac{\rho C_p}{k}\frac{\partial T}{\partial t} \tag{2.1}$$

$$T(r = \infty, t) = T_i \tag{2.2}$$

$$\lim_{r \to 0} 2\pi rkh\frac{\partial T}{\partial r} = q \tag{2.3}$$

$$T(r, t = 0) = T_i \tag{2.4}$$

This set of equations is solved using a Boltzmann's transformation of $z = r^2/4kt$ resulting in equation 2.5. The dummy variable s is used in equations 2.5 and 2.6. It is recognized that the integral of equation 2.5 is the Exponential Integral (equation 2.6) [16].

$$\frac{\partial T}{\partial t} = \left(\frac{q}{4\pi kh}\right)\int_z^{\infty}\frac{e^{-s}}{s}ds \tag{2.5}$$

$$-E_i(-z) = \int_z^{\infty}\frac{e^{-s}}{s}ds \tag{2.6}$$

Equation 2.7 is the result of using the principle of superposition along with a series expansion of the exponential integral for positive, small z.

$$\frac{\partial T}{\partial t} = \left(T_i - T_{(r_w, t_1+t_2)}\right) = \frac{q}{4\pi kh}\, ln\frac{t_1+t_2}{t_2} \tag{2.7}$$

where the thermal conductivity in watts per meter kelvin is k, h is the height of the cylinder in meters, q is the heat rate in watts, T_i is the initial temperature in Kelvin at t_1, t_1 is the total time of heat input in seconds, and t_2 is the time since heat input stopped, also in seconds. $T_{(r_w, t_1+t_2)}$ is temperature at the radius of the hole after t_1 and transient t_2. Knowing q from the power to the heater the slope of a graph of T versus $\ln((t_1 + t_2)/t_2)$ allows for the measurement of k. Thus, the temperature buildup analysis will infer the thermal conductivity if the heat rate is known.

However, if the thermal conductivity is known and it is valid to assume constant heat transfer along the axis and for small time, equation 2.1 can infer the heat rate.

The single phase constant flow experiments were conducted to evaluate the base heat transfer rates found in flow through a connected fracture in hot dry rock. The experiment was set up as illustrated in Figure 2.2. The SHDR was heated in an oven until the internal thermocouples all arrived at equilibrium around 90℃. The experiments were conducted with the block being insulated from the ambient environment. A syringe pump was used to inject room temperature tap water into the SHDR. The temperatures of the water at the inlet and outlet of the SHDR were recorded at a rate of 30 Hz with T-type sheathed thermocouples. The heat transfer from the SHDR was calculated simply using equation 2.8:

$$q = \dot{V}\rho C_p \Delta T \tag{2.8}$$

where q is the heat rate, $\dot{V}$ is the volumetric flow rate, p is the density, Cp is the specific heat, and ΔT is the temperature difference between the inlet fluid temperature and the outlet value. The heat rate was recorded after thermal breakthrough which varies with flow rate. Thermal breakthrough for this instance is defined as a time when the temperature of the outlet fluid changed by 10% of the difference between the initial temperature of the SHDR and room temperature. The volumetric flow rate was recorded from the syringe pump and checked for accuracy in a graduated cylinder (see Figure 2.2).

The cyclic pressure experiment was set up to measure heat transfer by vaporizing water within the SHDR (see Figure 2.3). The experiment was initiated by filling the SHDR with water. A valve was then closed so that the SHDR became a sealed vessel. The entire system was initially at atmospheric pressure, and the SHDR was heated to 90 ± 3°C for every experiment. Once the water and the SHDR came to thermal equilibrium the vacuum pump was activated and the system inside the SHDR became depressurized. When the SHDR was depressurized, the water vaporized at a rate related to the heat transfer from the SHDR divided by the enthalpy of vaporization of the water. The dramatically increased specific volume of the steam displaced some of the liquid water out of the SHDR. Thus evaporation fluxes could not be directly measured by condensate collection. The cyclic pressure experiments were conducted with the axis of the SHDR vertical and an insulated vapor separator at the hole outlet to allow the liquid to flow back.

The heat flux from the SHDR was calculated using the same temperature buildup and drawdown method that was used to find the thermal conductivity. Since thermal conductivity was previously inferred, the slope of the line through data on a plot of temperature versus the natural log of the ratio of time intervals during boiling as related by equation 2.8, is equal to the average heat transfer rate divided by the $4\pi k_s h$.

2.3.2 Numerical Model Methodology

The numerical model used to simulate the physical experiments was created by discretizing the heat equations. A cylindrical coordinate system was chosen because it best represents a circular hole and surrounding media. The assumption of axisymmetry is used to simplify the geometry to a 2-dimensional (r-z plane) point of interest. Axisymmetry is valid when there is no change in temperature or stress with angle. To determine the temperature distribution in the solid media, conduction heat transfer was solved by means of Fourier's Law in conjunction with the conservation of energy principle. Equation 2.9 is the Heat Equation for cylindrical coordinates solved assuming axisymmetry.

$$\frac{1}{r}\frac{\partial}{\partial r}\left(r\frac{\partial T_s}{\partial r}\right)+\frac{\partial^2 T_s}{\partial z^2}=\frac{1}{\alpha_s}\frac{\partial T_s}{\partial t} \tag{2.9}$$

where T_s is temperature, r is radius, z is the axial length, t is time, and α_s is the thermal diffusivity of the solid. The control volume approach was used to discretize equation 2.9. Each control volume balances the energy stored with the energy conducted through its faces. This provides an explicit dynamic solution of temperature that is solved for each node in ascending order. For the application of using this code to simulate a geothermal reservoir, the semi-infinite condition is used. In this state, the boundary conditions at z equal to zero and length are insulated (Neumann). At r equal to the outer radius, the boundary condition is insulated. The outer radius has to be set large enough that the code has enough time to run so that the temperature gradient does not interact with it. This is dependent on the thermal diffusivity of the material.

The temperature within the fluid was calculated using the assumption of plug fluid flow that is driven based on equilibrium of momentum, which accounts for advection and conduction between surrounding nodes. Plug flow is used because it is representative of fluid flow in a geologic fracture. Equation 2.10 is the partial differential equation that represents the transient conservation of energy in the fluid.

$$\frac{1}{r}\frac{\partial}{\partial r}\left(r\frac{\partial T_f}{\partial r}\right)+\frac{\partial^2 T_f}{\partial z^2}-\frac{v}{\alpha_f}\frac{\partial T_f}{\partial z}=\frac{1}{\alpha_f}\frac{\partial T_f}{\partial t} \tag{2.10}$$

where v is the fluid velocity and α_f is the fluid thermal diffusivity. The nodes at the hole inlet are held at a constant temperature and are coded as a fluid source. Equation 2.10 accounts for axial advection, axial, and radial conduction, but assumes negligible radial advection. This is acceptable for the small radius (0.3175 cm) tube and extremely low Reynolds number flows (Re < 10^{-6}). The boundary between the rock and water is represented by having a boundary node on the wall represent the volume. These boundary nodes at the hole radius are split and represent the fluid on the inner half and the solid for the outer half. This was chosen to meet the boundary condition requirements of the fluid and solid having the same temperature. This is accomplished using the control volume approach to discretization. For simulating the physical experiments, a uniform grid spacing of 1 mm in both the radial and axial direction was used.

The heat equations for the solid and the fluid were discretized using the central differencing Taylor-series formulation. Equation 2.11 and 2.12 are the matlab discretized forms of equations 2.9 and 2.10 for the central nodes of the solid and the fluid, respectively. The left-hand side of equations 2.9 and 2.10 represent the derivative of temperature with respect to time.

$$\begin{aligned}\left(T^{new}_{s(i,j)}-T_{(i,j)}\right)=\frac{1}{\rho_s Cp_s V_{s(i,j)}}\Bigg(&\frac{-2\pi k_r r_{(i+1)}dz}{dr}\left(T_{(i,j)}-T_{(i+1,j)}\right)+\frac{-2\pi k_r r_{(i)}dz}{dr}\left(T_{(i,j)}-T_{(i-1,j)}\right)\\&+\frac{-2\pi k_r\left(r^2_{(i+1)}-r^2_{(i)}\right)dz}{dr}\left(T_{(i,j)}-T_{(i,j+1)}\right)+\frac{-2\pi k_r\left(r^2_{(i+1)}-r^2_{(i)}\right)dz}{dr}\left(T_{(i,j)}-T_{(i,j-1)}\right)\Bigg)\end{aligned} \tag{2.11}$$

$$\left(T^{new}_{f(i,j)} - T_{(i,j)}\right) = \frac{1}{\rho_f Cp_f V_{f(i,j)}} \left(\frac{-2\pi k_f r_{(i+1)} dz}{dr}\left(T_{(i,j)} - T_{(i+1,j)}\right) + \frac{-2\pi k_f r_{(i)} dz}{dr}\left(T_{(i,j)} - T_{(i-1,j)}\right) \right.$$
$$+ \frac{-2\pi k_f \left(r^2_{(i+1)} - r^2_{(i)}\right) dz}{dr}\left(T_{(i,j)} - T_{(i,j+1)}\right) + \frac{-2\pi k_f \left(r^2_{(i+1)} - r^2_{(i)}\right) dz}{dr}\left(T_{(i,j)} - T_{(i,j-1)}\right)$$
$$\left. + \left(-v\pi\left(r^2_{(i+1)} - r^2_{(i)}\right)\rho_f Cp_f\left(T_{(i,j)} - T_{(i,j-1)}\right)\right) \right) \tag{2.12}$$

where *V* is the volume of the node, *dz* is the axial node distance and *dr* is the radial node distance, *i* represents the radial direction and *j* the axial, *v* is the velocity of the fluid flow.

The heat transfer numerical model was verified using analytical solutions with simplified geometries to assure that the heat equations were solved correctly using numerical simulation as explained in detail in Appendix D. Seven verifications were performed. Verifications 1-5 are checking the conduction in the solid and verifications 6 and 7 are for convection in the fracture. Verification 1 was a comparison between the finite difference code and the analytical steady state solution of temperature of an infinite hollow cylinder with the inner and outer radius being held at constant but different temperatures. The finite difference model calculated the temperature distribution in the r direction correctly. Verification 2 was a comparison between the finite difference model with the analytical steady-state solution of the temperature of a finite hollow cylinder with *r = a* maintained at a temperature that is a function of *z*, *f(z)*, and all other boundaries held at a temperature of zero. This verified that the finite difference model also calculated the temperature distribution in 2-dimensions correctly. Verification 3 likened the model with an analytical steady state solution of a heat flux *(f(z))* applied to the inner radius of a finite hollow cylinder while all other boundaries are kept at a temperature of zero. This verified the model's ability to have a heat flux boundary condition. Verification 4 was a second test that the model can accurately calculate a heat flux boundary, but with insulated walls. A heat flux was applied to the inner radius of the infinite hollow cylinder. At *z = 0* and *z = L* the boundaries were insulated, and the outer radius was held at a constant temperature. Verification 5 matched the finite difference model to the transient analytical solution of 1-dimensional conduction with a heat source boundary condition on the inner radius. This verified the ability of the model to be accurate through time. Verification 6 was a comparison of the finite difference model with the analytical steady state solution of plug flow in a pipe with a constant inlet temperature and a constant wall temperature. This verified the models ability to determine the temperature profile of the fluid flow in the fracture. The time dependency of the flow in the model was verified (7) against a 1-dimensional transient advection-diffusion solution. The analytical solution used for verification 7 assumed the initial temperature of the fluid to be zero and an insulated wall boundary condition in the fracture with 100ºC water injection.

The relative normal errors (L2) between the model and the analytical temperature profiles were calculated to test agreement. The error was calculated by taking the absolute difference of the temperature specified by the analytical solution with the temperature predicted by the numerical model, normalized by the temperature from the analytical solution. The errors are unitless and represent the decimal form of the percentage of difference. The relative normal error of verifications 1-7 were 0.0002733, 0.0087408, 0.010777, 0.000058664, 0.00084554, 0.0038, 0.015901, respectively. These show great agreement with the code.

2.4 Experimental and Numerical Results

The purpose of this study was to show that higher heat transfer rates could be obtained by operating a geothermal reservoir cyclically with respect to pressure causing fluid vaporization. With this in mind, several experiments were run to validate the hypothesis. The density, specific heat, and thermal conductivity of the SHDR were experimentally determined to facilitate calculations in future experiments and to aid the comparison of the SHDR to typical rocks. The density and specific heat of the SHDR were found to be 2060 ± 160 kg/m3 and 0.945 ± 0.05 kJ/kg-K, respectively. The single phase constant flow experiment was run to show heat transfer rates of typical enhanced geothermal systems. The high Peclet number experiments represent high water flows through the preferential flow pathways in the reservoir. The low Peclet number experiments are representative of conditions away from the preferential flow pathways, where the fluid temperatures are near the adjacent solid temperatures. Finally the cyclic pressure experiments were conducted to evaluate the heat transfer rates from vaporization by depressurization.

Figure 2.4 shows the adjusted temperature for the thermocouple embedded at the wellbore, versus the natural log of the ratio of the total time *(t_1+t_2)* to the time beginning once the constant heat flux from the cartridge heater ended *(t_2)*. Figure 2.4 is an example plot for just one of six thermal conductivity experiments. The slope of the line for the natural log of time between 0.5 and 3 is used in equation 2.1 to find the thermal conductivity or heat transfer rate. The thermal conductivity experiments provided an average thermal conductivity of 2.18 ± 0.18 W/m-K.

The results from several single phase constant flow and cyclic pressure experiments are shown in Figure 2.5. These results are from experiments run with the initial temperature of the SHDR between 88°C and 93°C. The constant fluid velocity heat transfer rates were determined after the thermal gradient broke through the length of the SHDR and thus represent different instances in time. The time varied per experiment and is inversely proportional to the Peclet number. The heat rate for the single phase experiments is divided by the difference between the initial temperature and the room temperature. The vaporization from depressurization experiments were conducted 5 times and the heat rate was found to be 39.16 ± 4.67 Watts. Error propagation for the experimentally determined heat rate was calculated using equation 2.13, which is the first order estimate of the multivariable version of the Taylor series [17]. Equations 2.2 and 2.7 are used with equation 2.34 to find the error associated with each data point (see Figure 2.5).

$$\Delta f(\tilde{x}_1, \tilde{x}_2, \dots, \tilde{x}_n) \cong \left|\frac{\partial f}{\partial x_1}\right| \Delta\tilde{x}_1 + \left|\frac{\partial f}{\partial x_2}\right| \Delta\tilde{x}_2 + \cdots + \left|\frac{\partial f}{\partial x_n}\right| \Delta\tilde{x}_n \tag{2.13}$$

where *x* represents the multiple variables of the function *f*, *Δx* is the error of *x*, and *df/dx* is the partial derivative of *f* with respect to *x*. The errors shown in Figure 2.5 are 23.9% for the dimensionless heat rate and 14.7% for the modified Peclet number.

The finite difference model predictions are compared to experimental results to validate the model (Figure 2.5). The model was run with fluid flow at varying Peclet numbers, the heat transfer to the fluid was then calculated. The modeled results have a 4.64% deviation from the experimental data. This validates the ability of the simulation to accurately quantify heat transfer rates.

The numerical model was used to study the heat transfer process of the constant flow rate experiments. The heat transfer was determined using equation 2.14. This is different than the way it was calculated experimentally (see equation 2.8). However, equation 2.14 represents the flow of heat from the rock to the fluid, and equation 2.8 is the flow of heat encapsulated in the water.

$$q = \frac{2\pi k_r}{\log\left({r_{i+1}}/{r_i}\right)} \int_0^L (T_i - T_{i+1})\, dz \tag{2.14}$$

where L is the axial length of the computational domain, r_i is the radius at the well wall, and r_i+1 is the radius of the next node out from r_i. The numerical results are shown in Figure 2.6. The results were all calculated at a Fourier number of one with the fluid thermal diffusivity and a length equal to the well radius. Low Peclet numbers are driven by the thermal conductivity of the fluid. Larger Peclet numbers have heat flux that is dominated by the convection of fluid. Figure 2.7 shows the temperature profiles of a portion of the SHDR calculated computationally at various Peclet numbers and a Fourier number of one. At low Peclet numbers the heat transfer occurs over a small portion of the area close to the fluid inlet. Again, this is representative of fluid flow in EGS reservoirs removed from the preferential flow pathways, which comprise most of the reservoir volume.

2.5 Theoretical Methodology and Computations

2.5.1 Dimensionless Heat Transfer Methodology

A theoretical understanding of the heat transfer problem can be gained by studying the unsolvable coupled partial differential equations. The two equations to be studied are the Heat Equation in the solid (equation 2.9) and the Heat Equation in the fluid (equation 2.10), identified by the subscripts *s* and *f*, respectively. These equations correlate temperature with time and space based on Fourier's Law of Conduction and the first law of thermodynamics in conjunction with the conservation of energy. For the case of heat transfer in a fractured geologic media, variations in fracture apertures are better represented by cylindrical holes. Thus cylindrical coordinates are used. Temperature is assumed to not vary with respect to the tangential direction, therefore axisymmetric conditions are applied. Both Heat Equations are 1st order in time and 2nd order in space in 2-dimensions. This means that in order to be solved one initial condition and four boundary conditions are needed for each of the two equations. Equations 2.15, 2.16, 2.17, and 2.18 are the initial condition and the first three boundary conditions of the Heat Equation in the solid. Equation 2.15 is the initial condition in which there is a constant temperature T_0 everywhere. Equations 2.16 and 2.17 are an insulated condition at z equal to zero and length L. Equation 2.18 represents the case of the semi-infinite solid where the far-field temperature never changes.

$$T_s(r, z, t = 0) = T_0 \tag{2.15}$$

$$\frac{\partial T_s(r,z=0,t)}{\partial z} = 0 \tag{2.16}$$

$$\frac{\partial T_s(r,z=L,t)}{\partial z} = 0 \tag{2.17}$$

$$\lim_{r\to\infty} T_s\,(r, z, t) = T_0 \tag{2.18}$$

The Heat Equation for the fluid is found in equation 2.10 and adds an advection term to equation 2.9 which is purely diffusion. It is assumed that radial advection is negligible. The advection term enhances the heat transfer in the axial direction and can be used with a constant velocity, v (plug flow), or one that is a function of the radius (laminar flow). Equations 2.19, 2.20, 2.21, and 2.22 are the initial condition and the first three boundary conditions. The initial condition (equation 2.19) is the same as in the solid problem (equation 2.15). Equation 2.20 is the boundary condition at the axis when the radius is zero and represents symmetry. Symmetry is the same mathematically as insulated. Equation 2.21 is the boundary condition of the water being injected into the hole at a constant injection temperature T_I. Equation 2.22 is the semi-infinite boundary condition, which means that the far-field temperature in the axial direction does not change.

$$T_f(r, z, t = 0) = T_0 \tag{2.19}$$

$$\frac{\partial T_f(r=0,z,t)}{\partial r} = 0 \tag{2.20}$$

$$T_f(r, z = 0, t) = T_I \tag{2.21}$$

$$\lim_{z \to \infty} T_f\,(r, z, t) = T_0 \tag{2.22}$$

In order for an analytical solution to be achieved, both heat equations need an independent fourth boundary condition. However, the two regions are physically connected at the radius location denoted as r_i where the temperatures are equal (equation 2.23) and the heat fluxes are continuous (equation 2.24).

$$T_s(r = r_i, z, t) = T_f(r = r_i, z, t) \tag{2.23}$$

$$k_s \frac{\partial T_s}{\partial r} = k_f \frac{\partial T_f}{\partial r} \tag{2.24}$$

where T is the temperature, r is the radial distance, z is the axial distance, t is time, and k_s and k_f are the solid and fluid thermal conductivities, respectively.

The next step to having a better theoretical understanding of the controlling parameters is to nondimensionalize the problem. The order in which normalizing constants are chosen to form dimensionless variables is by physical significance than mathematical simplicity [15]. The temperature was nondimensionalized by making it a fraction of the largest possible temperature difference (equation 2.25). In equation 2.25, T_0 is the initial temperature of the system and T_I is the injection temperature. The radius and axial distance are made dimensionless by dividing by the fracture radius (equation 2.26 and 2.27). All of the terms chosen where nondimensionalized by physical significance except for the time variable. The time, equation 2.28, was chosen for mathematical simplicity. Equation 2.29 is the dimensionless fluid temperature that was nondimensionalized the same as the solid.

$$\tau_s = \frac{T_0 - T_s}{T_0 - T_I} \tag{2.25}$$

$$r^* = \frac{r}{r_i} \tag{2.26}$$

$$z^* = \frac{z}{r_i} \tag{2.27}$$

$$t^* = \frac{\alpha_s t}{r_i^2} = Fo \tag{2.28}$$

$$\tau_f = \frac{T_0 - T_f}{T_0 - T_I} \tag{2.29}$$

The dimensionless heat equation 2.30 is written by applying equations 2.25-28 to the heat equation 2.9. The dimensionless advection-diffusion equation 2.31 is derived by applying equations 2.26-29 to equation 2.10. Equation 2.32 is created by applying equations 2.25, 2.26, and 2.29 to the fluid-solid heat flux boundary condition equation 2.24.

$$\frac{\partial^2 \tau_s}{\partial r^{*2}} + \frac{1}{r^*}\frac{\partial \tau_s}{\partial r^*} + \frac{\partial^2 \tau_s}{\partial z^{*2}} = \frac{\partial \tau_s}{\partial t^*} \tag{2.30}$$

$$\frac{\partial^2 \tau_f}{\partial r^{*2}} + \frac{1}{r^*}\frac{\partial \tau_f}{\partial r^*} + \frac{\partial^2 \tau_f}{\partial z^{*2}} - \frac{v\, r_i}{\alpha_f}\frac{\partial \tau_f}{\partial z^*} = \frac{\alpha_f}{\alpha_s}\frac{\partial \tau_f}{\partial t^*} \tag{2.31}$$

$$\frac{\partial \tau_s}{\partial r^*} = \frac{k_f}{k_s}\frac{\partial \tau_f}{\partial r^*} \;@\; r^* = 1 \tag{2.32}$$

The dimensionless parameters that define the solid heat transfer and coupled fluid flow problem have now been introduced by the nondimensionalization process. The Fourier number which is the dimensionless time in equation 2.28. The constants on the right-hand side of equation 2.31 make up the thermal diffusivity ratio, *β*, equation 2.33. The thermal diffusivity ratio relates thermal conduction in the water to thermal conduction in the solid. This term plays a major role in heat transfer at low velocities or Peclet numbers. The constants on the right-hand side of equation 2.32 is the ratio of thermal conductivities and is represented by *κ* in equation 2.34. The Peclet number is given by the advection term on the left-hand side of equation 2.31 and is shown in equation 2.35. The Peclet number is the ratio of advection and diffusion in fluid flow that is experiencing convection heat transfer. When the Peclet number is combined with *β* and *κ* it forms the modified Peclet number, equation 2.36. The modified Peclet number is defined for this application as a ratio between the advective flux produced by the fluid flow and the heat transport in the solid and heat storage in the fluid. Thus, one would expect that the Peclet number would be the dominant parameter, with β and κ having secondary importance, depending on the fluid and solid thermal properties.

$$\beta = \frac{\alpha_f}{\alpha_s} \qquad (2.33)$$

$$\kappa = \frac{k_f}{k_s} \qquad (2.34)$$

$$Pe = \frac{v\, r_i}{\alpha_f} \qquad (2.35)$$

$$Pe^* = \frac{v\, r_i}{\alpha_f}\left(\frac{k_f}{k_s}\right)^a \left(\frac{\alpha_s}{\alpha_f}\right)^b \qquad (2.36)$$

2.5.2 Thermal Fluid Penetration

The heat transfer model was used to compare the thermal behavior of water, carbon dioxide, and mercury with the mortar solid. Water and carbon dioxide are both working fluids that have been studied for enhanced geothermal reservoirs. Brine was also considered but is insignificantly different from water in regards to the thermal properties that it was left out. Mercury was chosen as an aid to compare a largely different fluid, with respect to the thermal properties. The thermal properties of carbon dioxide were taken at 423 K and a pressure of 150 bar and are seen in Table 2.1 [18]. The properties for mercury were taken at 400 K and mercury is assumed to be incompressible [19]. All of the properties correspond with the in-situ conditions at Raft River geothermal field that has an Elba Quartzite reservoir at 1,500 m MD [20]. The thermal fluid penetration was determined by finding the distance from the water injection point along the axis that has experienced a 10% temperature drop after a given amount of time. The amount of time used for each case was determined by the Fourier number of the solid being set to two. The axial distance of thermal fluid penetration was nondimensionalized by dividing it by the radius of the hole (Equation 2.37) and compared to the modified Peclet number (Figure 2.8).

The slopes of the three equations in Figure 2.8 were used to find variables *a* and *b* in equations 2.36 as can be seen in equation 2.37. Then equation 2.37 was used to create Figure 2.8 with modified Peclet numbers that match thermal penetration length. The fit to the curve shown in Figure 2.8 is equation 2.38.

$$x^* = f(Pe^*) = \frac{vr}{\alpha_f}\left(\frac{k_f}{k_s}\right)^{0.018}\left(\frac{\alpha_s}{\alpha_f}\right)^{-0.76328} \tag{2.37}$$

$$\frac{x_{th}}{r_i} = 1 + 1.26\frac{vr}{\alpha_f}\left(\frac{k_f}{k_s}\right)^{0.018}\left(\frac{\alpha_f}{\alpha_s}\right)^{0.76328} \tag{2.38}$$

The correlation represented by equation (2.38) relates a penetration depth that is proportional to the hole radius, and the fluid modified Peclet number. The weak dependence on the ratio of thermal conductivities is noted. Also noted is a relatively strong dependence on the ratio of the thermal diffusivities. Mercury, a fluid with a diffusivity greater than that of the solid, penetrated further.

Figure 2.9 illustrates the temperature of a solid with various working fluids at 3 different modified Peclet numbers. It is noteworthy that water and carbon dioxide both have similar thermal diffusivities and thermal conductivities and the thermal diffusivity and thermal conductivity of mercury are an order of magnitude higher. Figure 2.9, however, shows that water and mercury extract a similar amount of heat from the solid. To quantify the differences in heat transfer, the total heat transfer, *q*, from the solid to the fluid can be specified in equation 2.39 and 2.40.

$$q = \frac{\pi v r^2 k_f}{\alpha_f}(T_o - T_I) \tag{2.39}$$

or, considering (2.37),

$$q = \pi r k_f Pe^*(T_o - T_I)\left(\frac{k_f}{k_s}\right)^{-0.018}\left(\frac{\alpha_f}{\alpha_s}\right)^{-0.76328} \tag{2.40}$$

Using the properties listed in Table 2.1, the following total heat transfer from the solid to the three fluids for each of the three different *Pe**'s shown in Figure 2.9 are calculated and tabulated in Table 2.2. The observations from Figure 2.9 are confirmed that water and mercury have nearly an order of magnitude higher heat transfer than CO_2.

2.5.3 Void Percentage

Geologically, the porosity is a defining characteristic of the reservoir. It is defined as the volume of nonrock space in the total volume of space. The porosity can give an estimation of the amount of water or oil in the reservoir. In impermeable systems the porosity or nonrock space is found solely in the fractures and is referred to as the fracture void space.

When extracting heat from a geothermal reservoir by means of water vaporization by depressurization, the thermal conductivity of the rock and the mass of water in the void space compete to be the limiting factor for heat transfer. For the simplified case of pure water in a completely saturated reservoir with uniform crack spacing and assuming that permeability plays no part, the void percent determines which factor is limiting. Equation 2.41 can be used to calculate the critical void percent for a reservoir, where the latent energy in the water equals the sensible energy in the rock.

$$V_{cr} = \frac{100\ \rho_s C p_s \Delta T}{x\ \rho_f h_{fg} - \rho_s C p_s \Delta T} \tag{2.41}$$

where V_{cr} is the critical void percent, ρ is the density, C_{ps} is the specific heat, ΔT is the assumed temperature drop, and h_{fg} is the enthalpy of vaporization of water. If the void percent is larger than that specified by equation 2.41, then the thermal conduction in the rock will be the limiting factor, not the mass of water. This is also shown in Figures 2.10 and 2.11. The numerical simulation was run in conjunction with the experimentally determined heat transfer in this work of 39.2 Watts to study boiling. This heat transfer coefficient is at its maximum when the pressure drop is initially introduced. The heat rate lessens when the rock temperature approaches the boiling temperature of the rock. In the finite difference code, equation 2.42 is multiplied to the boiling heat rate to emulate the heat rate drop with respect to approaching thermal equilibrium. Figure 2.10 is based on a void percent of 0.01%, which is the same as the SHDR. The temperature profile shown in Figure 2.10 is from the total mass of water being vaporized. The outer half of the cylinder is unaffected by the heat extraction at that time. Figure 2.11 is under the same conditions but for a void percent of 0.11%. These are both for 5 K change in temperature, which at 500 K corresponds to 230.1 kPa pressure reduction.

$$\frac{(T(i) - T_{final})}{(T_{initial} - T_{final})} \tag{2.42}$$

where $T(i)$ is the temperature of the node at the well radius, T_{final} is the assigned boiling temperature for the given pressure, and $T_{initial}$ is the temperature at which the node started. The critical void percent can be calculated for various temperatures (see Table 2.3). Table 2.3 only goes to a change in temperature of 20 K because that is a very large temperature shift in a geothermal system within the time frame of one cycle. A change in temperature of 20 K also corresponds to a very large change in pressure, 825.4 kpa or 120 psi at a reservoir temperature of 500 K for pure water. Granite is included in Table 2.3 because it is a common basement rock encountered in EGS reservoirs. Granite can have a void percent of greater than 2 % in EGS reservoirs [21], which means that using this process, thermal conductivity of the granite will limit the heat transfer process and complete vaporization is unlikely to occur.

2.6 Discussion

It was observed that the density and thermal conductivity of the simulated hot dry rock (SHDR) match very closely with fine-grained quartz diorite, consolidated sandstone and granite based on the values from the Thermophysical Properties of Matter Data Series [13]. The Thermophysical Properties of Matter Data Series also revealed that the SHDR has a higher thermal conductivity than that of all mortars listed [13]. This is consistent with the higher density of the SHDR and that none of the mortars were made with silica fume. These results show that the SHDR is a good approximation for the thermal characteristics of hot dry rock.

It was observed during the single phase constant flow experiment that some of the water that flowed through the SHDR became entrained by capillary action. This was discovered by comparing the inlet mass flow rate to the mass flow rate out during the experiment. This rate differential diminished as the SHDR became saturated.

In some of the cyclic pressure experiments, part of the tubing for the fluid exiting the SHDR was transparent. This section of transparent tubing allowed for visual observations of flow regimes. The flow appeared to be two-phase but liquid dominated. This occurs because the area where vaporization occurs was too small to allow the gases to move past the liquid. Thus, the vapor bubbles displaced some of the liquid from the experiment. Another consequence of steam displacing liquid water was that the exiting enthalpy quality could not be calculated by knowing only the temperature and pressure. The quality of the two phase flow also has to be known for enthalpy to be determined. Thus, the inferred heat flux was calculated from temperature build-up and drawdown method. This new application of the method is valid because of the assumption that the heat transfer is constant along the length of the SHDR. The heat transfer rate along the length is constant because the system is in mechanical equilibrium during the experiment and because the length of time of the experiment was less than required for the heat to be conducted to the edges of the SHDR.

The results from the experimental data sets demonstrate that the heat transfer rates in the single phase constant flow experiments are proportional to the modified Peclet number. This result is reasonable since higher heat transfer rates from the SHDR to the water should be observed as advection becomes prominent. The modified Peclet numbers for flow in geologic media away from the preferential flow pathways, like that of enhanced geothermal systems, are less than one. This is inferred from the equation for the Peclet number and the Reynolds number and the results found in the works of McFarland and Murphy; and Ogino and Yamamura [22, 23]. From the experimental data, it is shown that de-pressurization produces heat transfer rates 10 times that of single phase constant flow experiments with modified Peclet numbers expected for EGSs. The work of Sigurdsson et al. shows a similar theme of the extracted enthalpy rising as the rate of steam rises with a decline in liquid water production [2].

These results imply that the rate of production of energy from some enhanced geothermal systems can be dramatically improved if operated cyclically with respect to pressure (see Figure 2.5). One approach to that enrichment is to inject high pressure water into a single well to open fractures and distribute the water phase throughout the fracture network, then to decrease the pressure to generate the steam throughout the fracture volume. Note that no inter-well connectivity would be needed to facilitate that energy production. And since large heat transfer rates at the fracture rock interface can produce thermal fractures [4, 5] it is possible that in-situ boiling caused by rapid depressurization can cause thermal-hydrological enhancement far from injection or production wells.

2.7 Conclusions

A study of heat transfer in Enhanced Geothermal System's reservoir was conducted. The focus of the study was to compare single phase flow with vaporization due to depressurization in the reservoir far from the wellbore. Experimental, numerical, and analytical methods were used to develop the following conclusions.

1. Mortar infused with silica fume is a good thermal representation for experimentally simulating impermeable geothermal reservoir rock based on the mortar properties.
2. The temperature buildup and drawdown method is suitable to determine the thermal conductivity and heat flux, when the heat flux can be assumed constant along the entire length of the axis in question.
3. Instantaneous heat flux from vaporization due to depressurization is an order of magnitude higher than single phase flow at low modified Peclet numbers.
4. Single phase flow has heat transfer that is dominated either by the fluid convection or matrix conduction. The driving heat transfer mechanism is determined by the modified Peclet number. For modified Peclet numbers greater than 1 the thermal conductivity of the fluid will drive the heat transfer.
5. Thermal break through will happen faster with carbon dioxide as the working fluid in an EGS than water.
6. The mechanism that controls the heat transfer process during vaporization caused by depressurization will depend on the fracture void percent, in the case where permeability is ignored.

2.7.1 Recommendations

The single well EGS has great potential and needs to be studied further to prove the viability. Experiments can be performed in sand or artificially created fractures in large (1 meter diameter) specimens to evaluate the vaporization and depressurization fronts. Geochemical analysis could be made for the potential scaling when selecting a field test site.

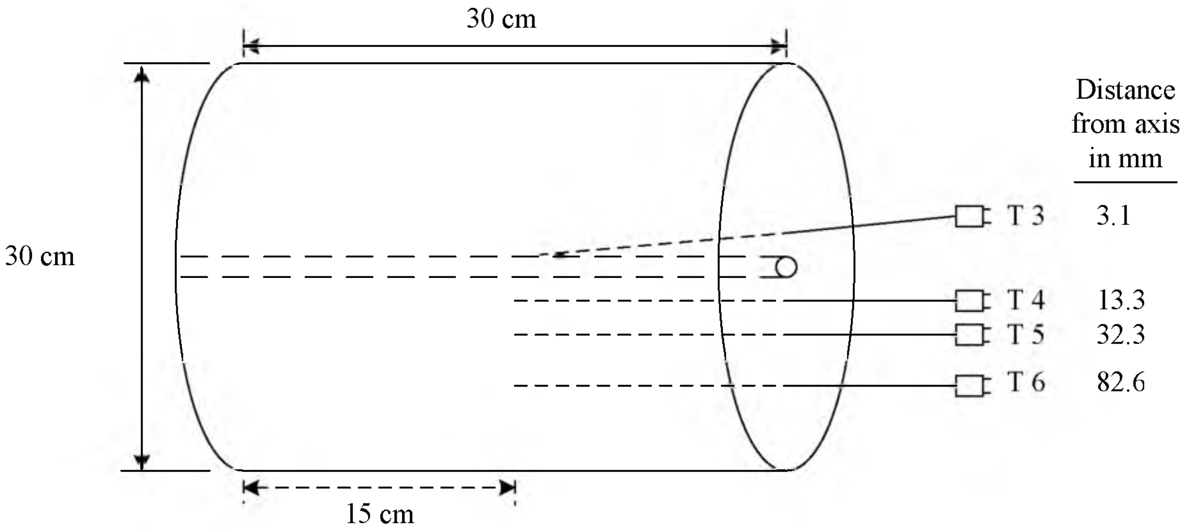

Figure 2.1: Schematic of the cylindrical SHDR benchtop experiment is shown with through hole and embedded thermocouples.

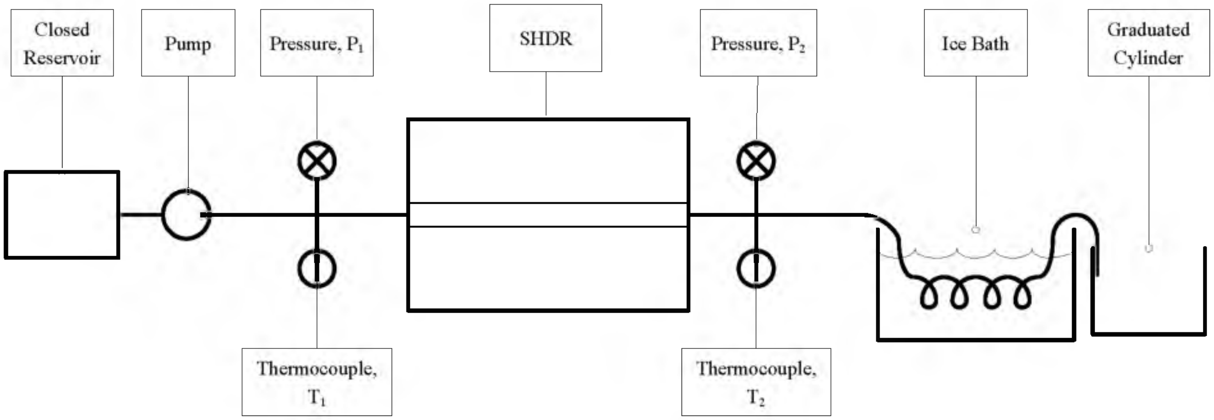

Figure 2.2: Schematic of the single phase flow experiment is shown.

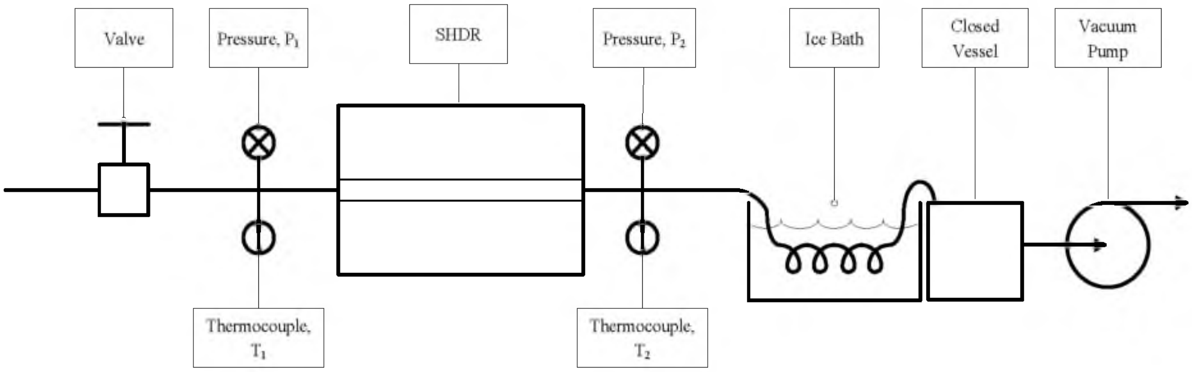

Figure 2.3: Schematic of the cyclic pressure experiment is shown.

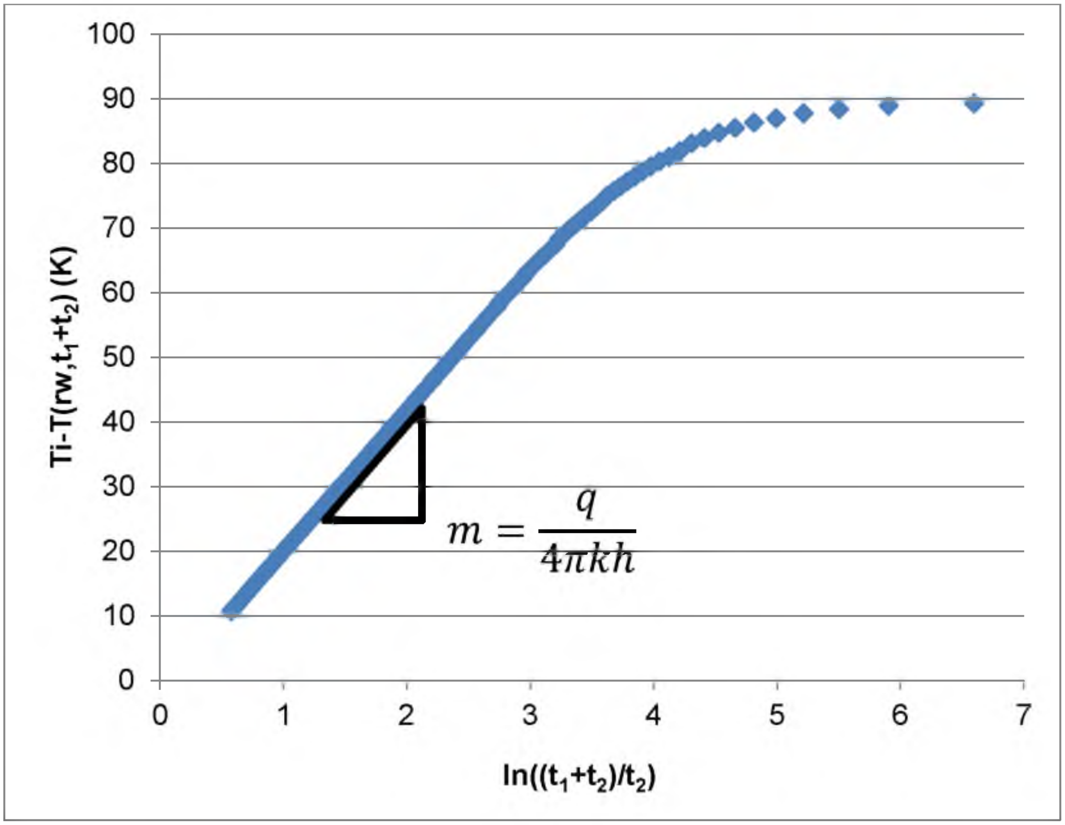

Figure 2.4: Adjusted temperature verses natural log of time for the thermocouple embedded at the wellbore during a thermal conductivity experiment is shown.

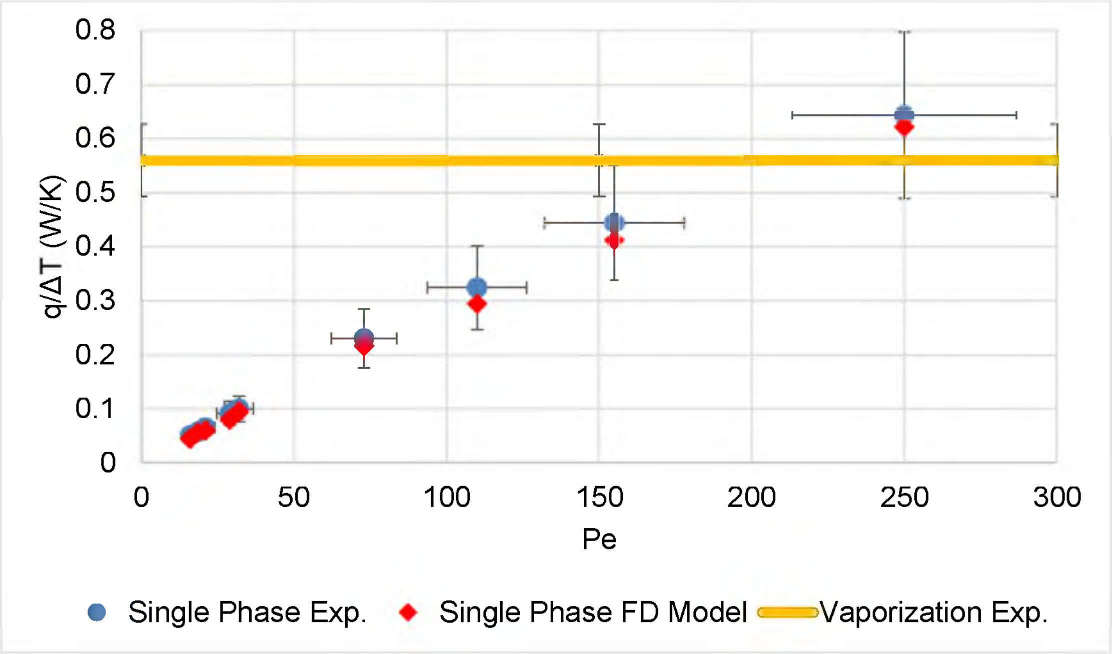

Figure 2.5: Experimental results from single phase flow and vaporization experiments. The numerical results for single phase flow heat transfer are also shown for the Peclet numbers chosen for the experiments.

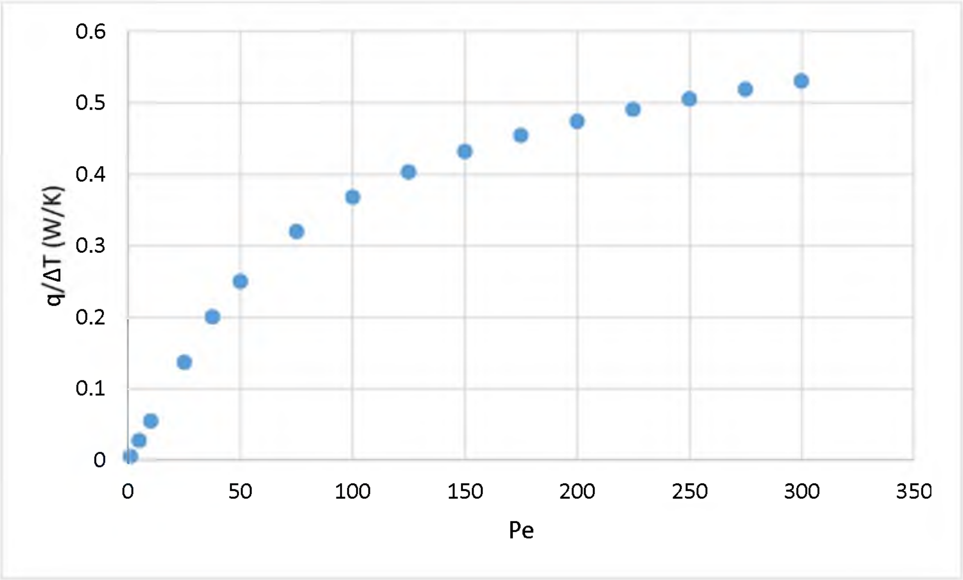

Figure 2.6: Heat transfer rate divided by temperature difference versus Peclet number from the numerical simulation is shown. Heat transfer was evaluated at Fo=1.

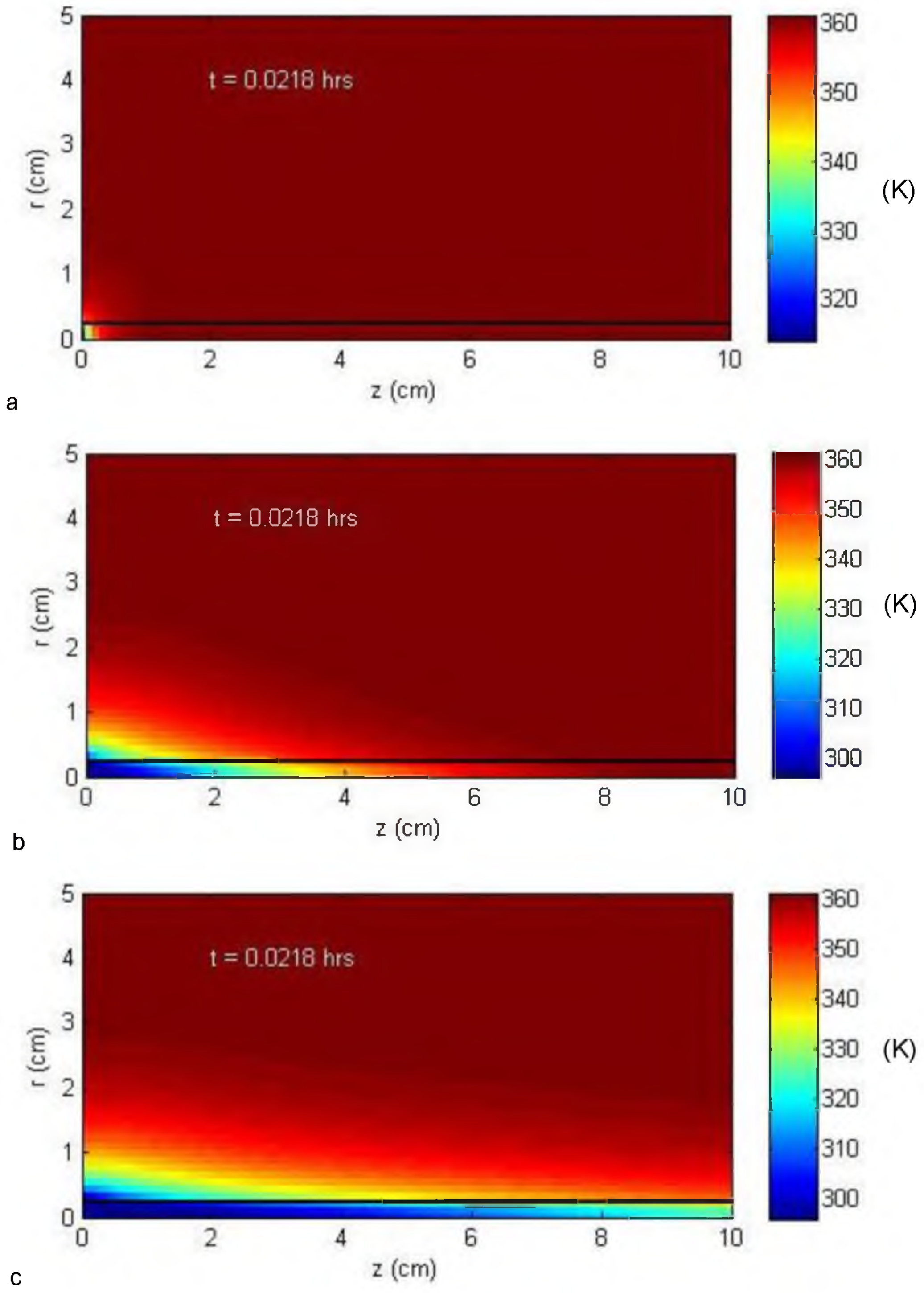

Figure 2.7: Low Peclet number single phase flow simulation temperature profiles. The solid and fluid initial condition is *T=360 K*, the water injection temperature *297 K*. Each one is showing the profile at a Fourier number of 1 and a Peclet number of: a. 1, b. 25, and c. 100.

Table 2.1: Thermal properties of water, CO2, mercury [18,19] and mortar.

	Units	Symbol	Water	CO2	Mercury	Mortar
Thermal Conductivity	kW/mK	k	0.000592	3.72E-05	0.0098	0.00218
Density	kg/m^3	ρ	1000	229.1	13287	2060
Specific Heat	kj/kgK	Cp	4.186	1.4477	0.1365	0.945
Thermal Diffusivity	m^2/s	α	1.41424E-07	1.12E-07	5.4E-06	1.12E-06

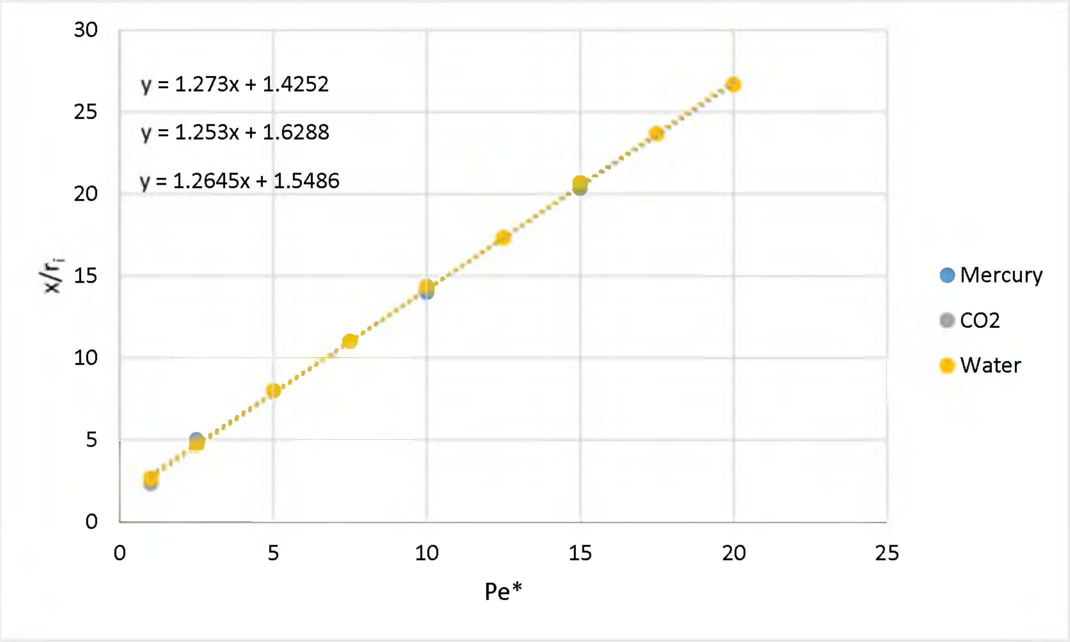

Figure 2.8: Shows the nondimensionalized thermal penetration length versus modified Peclet number for water and carbon dioxide taken at a Fourier number equal to 2.

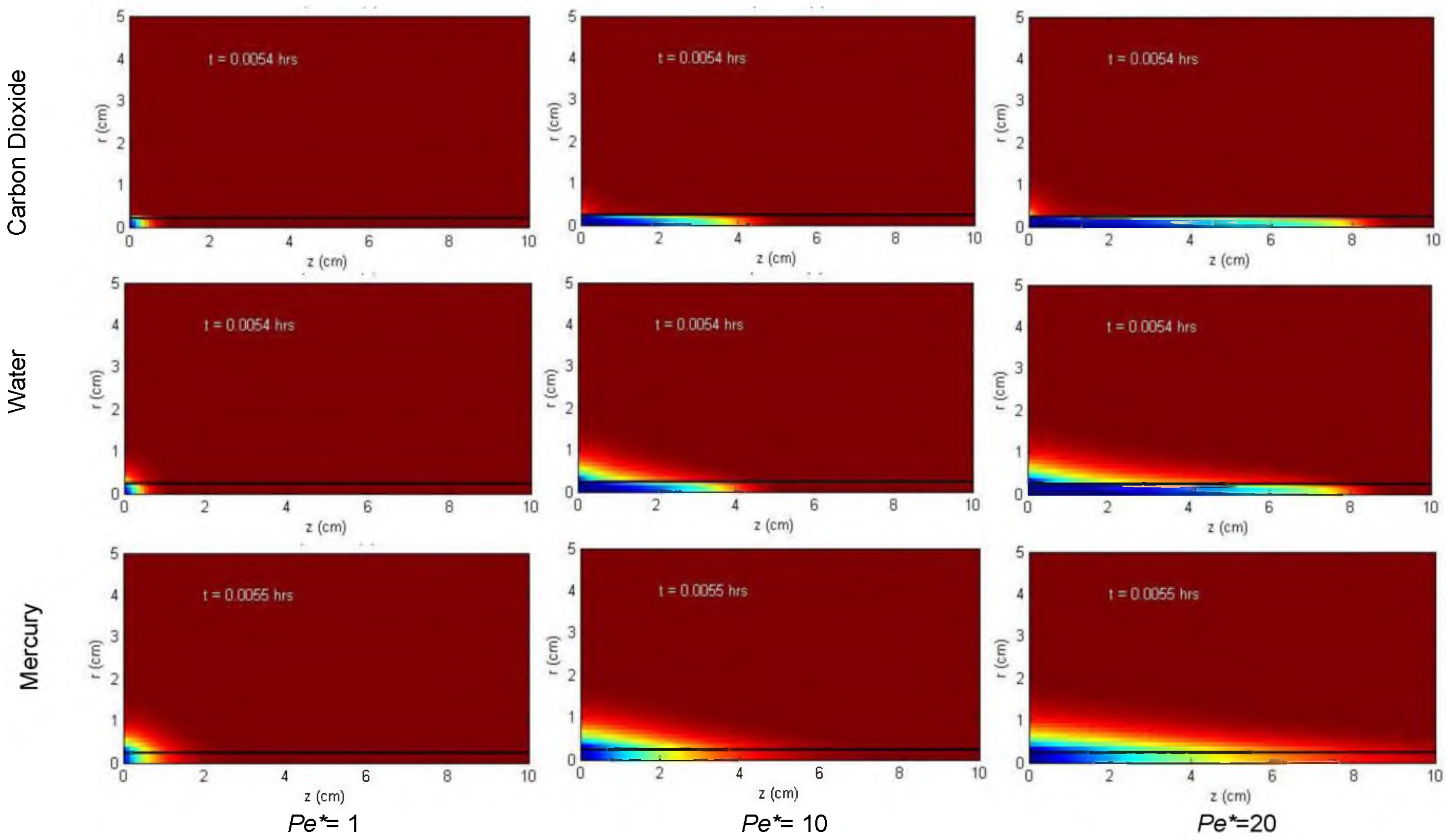

Figure 2.9: The temperature distributions for carbon dioxide, water, and mercury at various *Pe**s with the same Fourier number and thermal penetration depth. The range of temperature in Kelvin spans 300 in blue to 360 in dark red.

Table 2.2: Comparison of heat transfer (W/K) for the cases of figure 2.9

Fluid	Pe*=1	Pe*=10	Pe*=20
C0$_2$	0.004	0.040	0.080
Water	0.031	0.308	0.615
Mercury	0.030	0.300	0.600

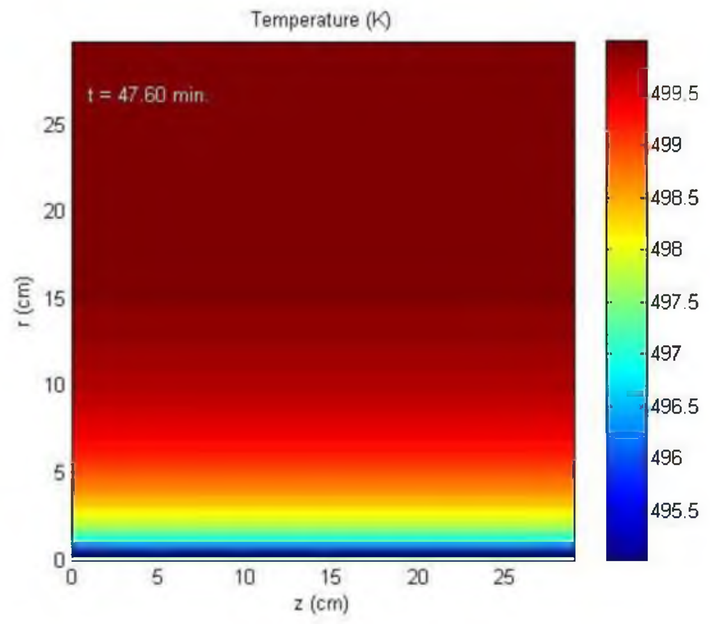

Figure 2.10: Temperature of the simulated hot dry rock determined computationally with a void percent of 0.01 %.

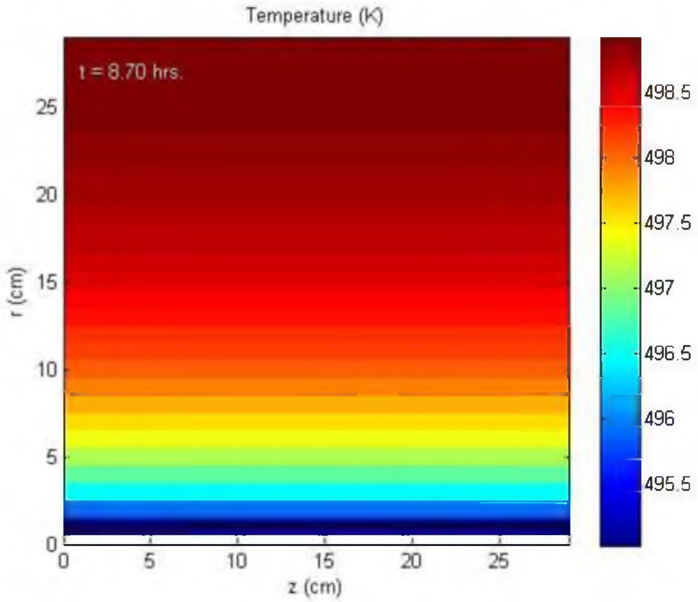

Figure 2.11: Temperature of the simulated hot dry rock determined computationally with a void percent of 0.11 %.

Table. 2.3 Important heat transfer properties
and critical void percent of mortar, and granite.

		Water	Mortar	Granite
h_{fg}	j/kg	2502000	N/A	N/A
ρ	kg/m^3	1000	2060	2680
c_p	J/kg K	N/A	945	837
x	1	Δ T	Critical Void %	
		1	0.08	0.09
		2	0.16	0.18
		3	0.23	0.27
		4	0.31	0.36
		5	0.39	0.45
		6	0.47	0.54
		7	0.55	0.63
		8	0.63	0.72
		9	0.71	0.81
		10	0.78	0.90
		11	0.86	1.00
		12	0.94	1.09
		13	1.02	1.18
		14	1.10	1.27
		15	1.18	1.36
		16	1.26	1.46
		17	1.34	1.55
		18	1.42	1.64
		19	1.50	1.73
		20	1.58	1.83

2.8 References

[1] Johnson, Philip W., 1989, “Fluid Flashing and Formation Mineralization Near Producing Geothermal Wells: A Literature Review and Simulation,” Geothermics, **18**, pp. 161-167

[2] Sigurdsson, O., Kjaran, S. P., Thorsteinsson, T., Stefansson, V., and Palmason, G., 1985, “Experience of Exploiting Icelandic Geothermal Reservoirs.” *GRC 1985 International Symposium on Geothermal Energy*, International Volume.

[3] Tester, J. W., H.D. Murphy, C.O. Grigsby, R.M. Potter, and B.A. Robinson, 1989, “Fractured Geothermal Reservoir Growth Induced by Heat Extraction,” SPE Res. Eng., **4**, pp. 97-104.

[4] Perkins, T.K., Gonzalez, J.A., 1985, “The effect of thermoelastic stresses on injection well fracturing”. J. SPE, pp. 78-88.

[5] Barr, D.T., 1980, “Thermal Cracking In Nonporous Geothermal Reservoirs,” M.S. thesis, Dept, Massachusetts Institute of Technology.

[6] Illman, W.A., and Hughson, D.L., 2005, “Stochastic Simulations of Steady State Unsaturated Flow in a Three-Laure, Heterogeneous, Dual Continuum Model of Fractured Rock,” J. Hydrol., **307**, pp. 17-37.

[7] Pruess, K., 1998, “On Water Seepage and Fast Preferntial Flow in Heterogeneous, Unsaturated Rock Fractures,” J. Contaminant Hydrol., **30**, pp.333-362.

[8] Pruess, K., Faybishenko, B., and Bodvarsson, G.S., 1999, “Alternative Concepts and Approaches for Modeling Flow and Transport in Thick Unsaturated Zones of Fractured Rocks,” J. Cont. Hydrol., **38**, pp. 281-322.

[9] Grant, M.A., and Garg, S.K., 2012, “Recovery Factor for EGS,” SGP-TR-194*, Proc. 37th Stanford Geothermal Workshop*, Stanford University, Stanford, CA, pp. 1-3.

[10] Brown, D.W., 1996. “Experimental Verification of the Load-Following Potential of a Hot Dry Rock Geothermal Reservoir,” *Proc. 21st Stanford Geothermal Workshop*, Stanford University, Stanford, CA, Jan 22-24, pp 281-285

[11] Carslaw, H.S., and J.C. Jaeger, *Conduction of Heat in Solids*, 2nd ed., Oxford University Press, London, 1959.

[12] Jaeger, J.C., *Application of the theory of heat conduction to geothermal measurements*, Terrestrial Heat Flow, Geophys. Monogr. Ser., Vol. 8, Lee W.H.K. Ed., pp. 7-23,

[13] Touloukian, Y.S., and C. Y. Ho, Eds., 1970-1977, *Thermophysical Properties of Matter, The TPRC Data Series* (13 vol. on Thermophysical properties: thermal conductivity, specific heat, thermal radiative, thermal diffusivity, and thermal linear expansion), Plenum Press, NY.

[14] Xu, H., and R. Desbrandes, 1991, “Formation Evaluation Using In-situ Measurements of Formation Thermal Properties.” Log Analyst, **32**(2), pp.144-157.

[15] Meyers, G.E., 1998, *Analytical Methods in Conduction Heat Transfer*, 2nd ed., AMCHT Publications, Madison, pp. 180, Chap. 7.

[16] Abromowitz, M., and Stegun, I.A., 1972, Handbook of Mathematical Functions With Formulas, Graphs, and Mathematical Tables, National Bureau of Standards, Applied Mathematics Series 55, pp. 228-229, Chap. 5.

[17] Chapra, S.C., and Canale, R.P., 2006, *Numerical Methods for Engineers*, 5th ed., McGraw Hill, San Francisco, pp. 91-92, Chap. 4.

[18] 2014, Thermal Properties of Fluid Systems, from http://webbook.nist.gov/chemistry/fluid/.

[19] Incropera, F.P., and DeWitt, D.P., 2002, *Fundamentals of Heat and Mass Transfer*, 5th ed., John Wiley & Sons, Hoboken, pp. 923, App. A.

[20] Bradford, J., McLennan, J., Moore, J., Glasby, D., Waters, D., Kruwell, R., Bailey, A., Rickard, W., Bloomfield, K., and King, D., 2013, "Recent Developments at the Raft River Geothermal Field," SGP-TR-198, *Proc. 38th Stanford Geothermal Workshop*, Stanford University, Stanford, CA, pp. 1-10.

[21] McClure, M.W., and Horne, R.N., 2014, "An Investigation of Stimulation Mechanisms in Enhanced Geothermal Systems," Int. J. Rock Mech. Min. Sci., 72, pp. 242-260.

[22] McFarland R. D., and H. D. Murphy, 1976. "Extracting Energy from Hydraulically Fractured Geothermal Reservoirs." *Intersociety Energy Conversion Engineering Conference*, 11, pp. 1-23.

[23] Ogino, F., and Yamamura, M., "Pressure Drop of Water Flow between Injection and Production Wells Intersected by a Circular Fracture," Geothermics, 27(1), 25-41, 1998.

CHAPTER 3

AN EXPERIMENTAL STUDY OF THERMAL AND HYDRAULIC GEOTHERMAL RESERVOIR STIMULATION OF BRITTLE IMPERMEABLE MATERIAL

3.1 Abstract

Reservoir stimulation is one of the key technologies necessary for optimization of enhanced geothermal systems. The higher volumetric density of fractures created by stimulation allows for greater access to the rock, which potentially yields higher fluid flow rates and increased productivity. Hydraulic fracturing is a well established practice and has been studied in great detail. Thermal fracturing, which is a natural process in heat mining from geothermal systems, has been studied primarily computationally. To study this further, a suite of experiments simulated a brittle, impermeable reservoir subjected to sequential hydraulic and thermal fracturing processes and vice versa. The in-situ stresses were simulated via a 1,000 psi stress placed normal to the sample borehole axis and the principle of superposition. To assess the effectiveness of the fracturing procedures, experiments were conducted in which cement paste, acrylic, and granite specimens were stimulated using methods analogous to those that could be used on a reservoir scale. Fractures that have faces perpendicular to the maximum horizontal principal stress were theorized by Perkins and Gonzalez [1] to occur once a hydraulic fissure has been thermally fractured. These fractures were created in blocks of acrylic and validate their findings. It was concluded that thermal fractures created significant permeability, but almost completely closed when the temperature was spatially equilibrated.

3.2 Introduction

Stimulation is a common practice to increase the injectivity/productivity of wells in hydrocarbon and geothermal reservoirs. Generally accomplished by hydraulic fracturing, geothermal stimulation can be achieved in other ways including chemical stimulation, propellant fracturing, and thermal fracturing. While hydraulic fracturing can be effective under most circumstances, understanding the interaction of hydraulic fracturing with thermal fracturing will be relevant to both the geothermal and the petroleum industries. Thermal fracturing has the added benefit of potentially creating fractures parallel to the least horizontal principal stress and perpendicular to hydraulic fractures, which are expected to extend in the direction of greatest principal stress. This allows the artificially created fracture network to grow in a different plane than the hydraulic fracture.

A sensitivity study conducted by Sanyal and Butler [2] concluded that the most influential variable for thermal energy extraction from a stimulated geothermal system is the resultant fracture volume. The fracture volume created by a stimulation treatment is related to the fracture geometry, orientation, and in-situ stress conditions of the reservoir. The resulting fracture geometry can affect fluid flow, thermal drawdown, short-circuiting, connectivity and injectivity, all of which influence how much thermal energy is extracted. An increase in understanding of and ability to perform stimulation techniques can open up new geographical areas of geothermal production worldwide. Tester et al. calculated that 2% of the thermal energy contained within the earth between the depths of 3.5 to 7.5 km “is roughly 2,600 times the annual consumption of primary energy in the United States in 2006.” [3] Most of that energy can only be accessed via stimulated Enhanced Geothermal Systems (EGS).

The research performed here experimentally examined how thermal and hydraulic stimulations affect a brittle reservoir. Hydraulic stimulation of reservoirs has been studied for years and is a well-known procedure. Thermal fracturing is the subject of much work done with respect to machine parts and even waterflooding in the oil and gas industry, but those fractures are viewed as side effects of other processes [4]. In this work, thermal fractures are sought for their ability to create unique fracture geometries. The analytical research of Perkins and Gonzalez

[5] indicates that thermal gradient will travel in an unfractured isotropic reservoir independent of stress orientation, normal to a point or line source. Through conduction of the impermeable reservoir, subcooled circular regions within the reservoir will be created. Due to thermal contraction these subcooled regions will fracture. If natural fractures or a previously created hydraulic fracture is preferentially oriented towards the maximum horizontal principal stress then an elongated subcooled region will occur, which has the potential to form fractures perpendicular to the maximum horizontal principal stress [5]. The effects of thermal and hydraulic fracturing on preexisting thermal and hydraulic fracture networks will also be studied.

Thermal fractures created along a hydraulic fracture were analytically and numerically shown to grow normal to the hydraulic fracture plane by Perkins and Gonzalez, [1] and Ghassemi [6]. This concept was validated experimentally in this work. Acrylic blocks were loaded uniaxially normal to the axis of the through hole and subjected to high internal water pressures to cause hydraulic fractures. The same blocks were then thermally fractured with liquid nitrogen while under the same 1,000 psi uniaxial external stress and in the same orientation.

3.3. Materials and methods

Proof of concept experiments were conducted using cement paste, acrylic, and granite specimens, stimulated by methods analogous to those that could be performed in a geothermal reservoir scale. The acrylic specimens are made of generic cast acrylic that were cast as one thick sheet then machined to size. They were purchased from Interstate Plastics. Acrylic was chosen because it is isentropic, homogeneous, and fractures brittlely under the conditions subjected to in this research [7]. The exact formula for the cement paste blocks and procedure are found in Appendix A. The granite was Barre Gray Granite acquired from the corporation Rock of Ages. Block specimens, 8 by 8 by 12.5 inches, were uniaxially compressed in order to simulate a difference in horizontal earth stresses without a polyaxial loading frame. The blocks also have a 0.25 inch diameter hole through the center. The hole was drilled in the acrylic with an endmill, manually advanced with no lubricant at 1200 rpm and a steel drill bit. Bold Technologies (Salt Lake City) drilled at both sides to accomplish the 12.5 inches depth and the hole met in the middle. The cement paste blocks were cast with a 1/4 inch cold rolled steel rod in the middle. The granite blocks were drilled with a 1/4 diamond drill from both sides by TerraTek Schlumberger.

All tests were conducted with the specimens uniaxially-loaded normal to the through hole axis and in the same orientation. An Omni Uniaxial Machine, as seen in Figure 3.1, applied the load. The stress was maintained at 1,000 psi. The uniaxial stress represents a deviatoric stress (presuming that axis of the hole is in the maximum principal stress direction, the 1000 psi is taken to represent the difference between the maximum and minimum total horizontal principal stresses). The experimental setup is also representative of a horizontal well in homogeneous media that has equal in-situ horizontal principal stresses. The 1,000 psi stress is patterned after the deviatoric stress of 1100 psi that is estimated at the Raft River, Idaho geothermal site [8]. Three 2 inch thick steel plates were used with a semihemispherical plate (gimble plate) to distribute the load evenly through the specimen. The two sides of the steel plates that contact the specimens were machined to 1/64 inch smoothness. Kimwipes were used as scratch protectors for the acrylic blocks. In order to minimize stress gradients and singularities, the sides of the cement paste specimens where machined with a surface grinder.

3.3.1. Hydraulic fracture experimental setup

Hydraulic fracture experiments were arranged in such a way that center portion of the through hole would be pressurized with water. Half of the samples were hydraulically fracture first then thermally fractured. The other half of the samples were thermally fracture first than hydraulically fractured. All specimens were hydraulically fractured by the same method and under the same orientation.

Hydraulic packers were fabricated to seal the injection tubes in the hole by means of compressing rubber O-rings. Figure 3.2 shows the packers that were designed and built to accomplish this task on such a small scale. The 1/8 inch Swagelok tubing in the center was secured with a Swagelok fitting at one end and tapped at the other. The other metal parts were made out of turned stainless steel tubing 1/4 inch outer diameter and 1/8 inch inner diameter. It was found that O-rings made out of 90 Durameter rubber maintained their position and the pressure. All moving parts and O-rings were coated in silicon plumbers grease. The grease allowed the metal parts to move after loading. The 1/8 inch tubes bent during the experiment and were good for at most 2 experiments.

A pneumatically powered dual piston pump delivered the DI water used to hydraulically fracture the blocks. The pump was set to deliver a constant flow rate during the experiment. The pressure increased until fracturing occurs, at which time the pressure dropped sharply. The pump control computer also recorded flow rate and pressure delivered from the pump. A solid steel rod 4 inches long and 3/16 inch diameter was placed inside the hole of the specimens during the experiment to reduce the volume of pressurized water, and minimize the size of the resultant hydraulic fracture. A 7500 psi pressure transducer was attached to the packer on the side of the block that was not receiving the water. The air was flushed out of the specimen prior to the experiment. Data was acquisitioned from the pressure transducer, the pump flow rate, pump pressure, video camera, and acoustic sensor (see Figure 3.3).

3.3.2. Thermal Fracture Experimental Setup

The thermal fracture experiments were designed to deliver liquid nitrogen to the same center section of the through hole. With the exception of the acrylic blocks that were hydraulically fracture first, all specimens were thermally stimulated by the same method and in the same orientation with regards to the 1,000 psi stress. The acrylic specimens that were previously, hydraulically fractured were oriented so that the principal stress was in the same configuration as the hydraulic fracture, but one of the blocks was flipped, to allow gravity to assist the liquid nitrogen in creating an elongated cooled zone.

Thermal packers were created to control the section of hole that was exposed directly to liquid nitrogen. Thermal packers were created by brazing 3/16 inch diameter brass tubing to 1/4 inch diameter copper tubes. Cotton was then glued to the brass tube in increments of 1 inch. Then silicone plumbers grease was applied to the outside of the packers for lubrication. The red silicon rubber stopper at the edge of the copper tube is the final seal (see Figure 3.4). The packers were 4 inches long except for the ones used for the acrylic blocks that were previously hydraulically fractured. Those packers were 6 inches and 2 inches, so that the liquid nitrogen would be exposed over the entire length of the hydraulic fracture. The liquid nitrogen exited the back packer that was bent to apply a 10 inch head (0.36 psig) (see Figure 3.5). The pressure head was used to ensure the in the advent of pooling, it would occur inside the block and not drain out. The thermal fracturing experiment was conducted by flowing liquid nitrogen for 30 minutes.

3.3.3. Visual Fracture Evaluation

The evaluation of 3-dimensional fractures in bench top experiments was accomplished in the acrylic specimens visually with pictures and photo editing software (Gimp). Because of the complicated geometries that were created, traditional descriptive techniques like strike and dip are insufficient. Instead a new approach was developed whereby the projected area of the fractures in the orthogonal directions of the principal stresses were visually evaluated. Many of the fractures are almost invisible when viewed perpendicular to their faces. This caused the need for experimenting with light and hundreds of digital photographs. The different methods used were, fluorescent (ambient) light; flash; light background; dark background; no ambient light with flash; and no ambient light with flash light at various angles. Many of these options were combined and all had success and failure depending on each individual fracture. The projected area of the fractures in a given direction was calculated by converting the number of pixels into inches squared. The 1/4 inch through hole was used as the scale for all of the conversions in each individual photograph. The reported areas are an average of the two opposite sides. This method minimizes the error of the fractures actual size being smaller when it is closer to the camera than the 1/4 inch hole and vice versa.

3.3.4 Acoustic Events

Acoustic events (AE) from laboratory samples are mechanical vibrations caused by microcrack growth on the scale of grain size. Their frequencies lie in the range of 100 kHz to

2000 kHz [9]. The larger the frequency of the AE the smaller the source. The sensor used during the indicated experiments was Vallen Systeme's VS900-RIC. It has a frequency range of 100-900 kHz and a 34 dB gain integrated preamplifier. A power supply was used to power the preamplifier and the voltage from the sensor was recorded with a National Instruments usb data acquisition module. Voltage was received from the sensor at the maximum rate of the data acquisition module of 50,000 hz. The National Instruments program LabVIEW read in the data, recorded the raw data then compressed it with a reduction factor of 100. This meant that it would then report the minimum, maximum, and mean for every 100 data points of raw data. Both data sets were saved as binary (TDMS) files. Excel was used to analyze the compressed data and plot the peak of all acoustic events.

In order for the piezoelectric element of the AE sensor to accurately detect the vibrations, the specimen had a location sanded smooth and the couplant, honey, was applied to remove air. Gorilla tape was then adhered to secure the sensor to the specimen during testing. Equation 3.1 is used to convert the voltage from the AE sensor to decibels [10].

$$Magnitude\ (dB) = 20\log_{10}\left(\frac{V}{Ref.V}\right) \tag{3.1}$$

where *V* is the voltage read from the sensor in mV, and *Ref. V* is the reference voltage in mV that is input into the equation to account for the variation in the power supply voltage and normalize the data between experiments so that the noise is always below 1 dB. Acoustic monitoring was used during all of the fracture experiments on the granite specimens. Blocks C10, C11, C12, and C13 were monitored with an acoustic sensor only for the thermally fracture experiments. The hydraulic fracture of C11 also was monitored for AE. The results from these experiments can be seen in Appendices A and B.

3.3.5 CT Scanning

CT scanning was used as a nondestructive means of evaluating the post experimentation fracture geometry. A Siemens Dual Definition Flash using SAFIRE Technology medical CT scanner was used to perform the scans at 140 keV and 850 mas. This is true for all of the CT scans performed except the post fracturing granite samples which were scanned at 1100 mas.

The scanner was also set to take 0.6 mm slice with 0.2 mm overlap between slices. Penetration of the cement paste and granite samples was attained using this process but the fractures could not be detected without a contrasting agent. Many different methods and substances were used. The most notable failures are: Xenon gas at 10 psi and 20 psi, water solution of potassium chloride and Barium Sulfate Suspension (2.1% w/v, 2.0% w/w, Berry Smoothie Readi-lat®2). The successful contrasting agents are 37% organically bound Iodine (medical Iodine), 35% potassium iodine in deionized water (35% SSKI), and Indium Casting Alloy. 35% SSKI was used on all of the cement paste blocks with success. 35% SSKI was insufficient for the granite blocks, which had to be injected with metal to have the fractures appear. The metal used was Indium Casting Alloy from McMaster-Carr. It has a melting temperature of 134°F and consists of 48% Bismuth, 25% Lead, 5% Indium, 13% Tin, and 9% Cadmium. Both Lead and Cadmium are toxic and thus the handling of the Indium Casting Alloy required safety precautions. In order to inject the alloy, a modified caulk gun was used to apply pressure to a piston inside a metal syringe holding the heated liquid. Spacers to hold the syringe in place, the piston, and the caulk gun drive rod all had to be turned on a lathe especially for this purpose. The injection of metal into the granite blocks occurred after both fracturing experiments were performed on each block. The results from the Indium Casting Alloy CT scans are seen in Appendix B.

3.3.6 Qualitative Metrics

It was hoped that various recording methods would provide quantitative data. However, the methods employed in this investigation only gave qualitative information. The methods that were tried during this suite of experiments are Infrared Thermal Imaging, High Speed Video Recording, and Photoelasticity.

Infrared Thermal Imaging (ITI) provides a video of the temperature of an object based on its radiative properties. The use of ITI to see inside the acrylic specimens to observe the temperature change failed because acrylic blocks are transparent in visible wavelengths but are opaque at infrared wavelengths. While it is possible to quantify the outside surface temperature using the ITI video images in the end the video would only be providing the temperatures on the outside of the block which are not of interest.

High Speed Video Recording was also attempted to determine the growth rate of the hydraulic fractures in the acrylic samples. Obtaining a focused image is a bit of an art. A very small aperture for the camera helped to focus the image, but there has to be high amounts of light intensity for it to be visible. In the end a compromise was made, the high speed camera was used to take images at 250 hz with a very narrow window of observation (about 1.5 inches diameter). During one of the hydraulic fracturing experiments, post thermal fracturing, the camera was recording the correct location of the hydraulic fracture growth. The fracture, however, extended past the frame of view in between images. Therefore, all that can be said is that the hydraulic fracture advances faster than 1/250 inch per second.

Stresses are difficult to determine in 3-dimensional specimens with photoelasticity. In the Manual on Experimental Stress Analysis [11] there are 5 methods discussed for the determination of stress in 3-dimensions. They are: Frozen Stress Method, Surface Stress from Normal Slices, Core Method, 3-Dimensional Shear-Difference Method, and the Scattered Light Method. All 5 methods require copies of the 3-dimensional parts made from epoxy formulations. Most are destructive tests and none of them are appropriate for dynamic stress measurements. For these reasons photoelasticity can be used to find the qualitative stress concentrations only, similar to what was done by Daehnke et al. [12].

3.3.7 Material Properties

The material properties that are used for analysis are in Table 3.1. The materials in Table 3.1 are those used to perform the bench-top experiments and Elba Quartzite. Elba Quartzite is included to compare the experimental materials with those of the rock that comprises the geothermal reservoir at Raft River, ID. Bradford [13] obtained density, Poisson’s Ratio, and Young’s Modulus of the Elba Quartzite using a suite of logs run at RRG-9 ST1 prior to casing the well. A density log was used to obtain an average density of the Elba Quartzite formation interval. Compression and shear wave slowness logs were used to obtain the Poisson’s Ratio and Young’s Modulus. The density, thermal conductivity, and specific heat for the mortar used were experimentally determined in [14]. The other properties for Mortar, Water and Liquid Nitrogen came from either the TPRC Data Series [15] or *The Handbook for Chemistry and Physics* [16]. The properties for Granite were obtained by the company Rock of Ages for Barre Gray Granite [17]. The Properties for Cast Acrylic (PMMA) were gathered from the manufacturer, Interstate Plastics [18], and another producer of Acrylic Sheets [19]. Fracture toughness values were obtained from [20-22] for Mortar, Acrylic, and Granite, respectively.

3.4 Results

One of the purposes of this work is to study the fracture orientation of thermal and hydraulic stimulation on bench-top samples that simulate a geologic reservoir. Another purpose is to better understand the bulk property changes of the specimens when fractured for the purpose of understanding sequenced fracture operations. Validating the concept of creating fractures that have faces perpendicular to the maximum horizontal earth stress is another goal. The bench top experimental analog that has been created to accomplish this was uniaxially loaded and therefore only has one principal stress. Regardless, fractures were created that have faces perpendicular to the maximum principal stress. The highlights of the sequenced experimental results are in Table 3.2. Of note is that the acrylic specimens that where first thermally fractured have hydraulic breakdown pressures that are less than half of the samples that where hydraulically fractured first. No such trend is clearly present in the granite or cement paste data. Table 3.3 shows the outcome of the CT scans and AE on the experiments. For a complete presentation of every experiment, including relevant figures and numbers see Appendixes A, B, and C.

3.4.1 Thermal Fractures Oriented Perpendicular to the Maximum Principal Stress

Hydraulic fractures were first created in two acrylic specimens, A2 and A4 by injecting water at high pressure. Both hydraulic fractures formed around 4,000 psi. Figure 3.6 shows the three orthogonal views of the hydraulic fracture of A2. A4 is almost identical except that it lines up closer to the axis of the hole. This is an expected result for hydraulic fracturing under these conditions. The projected area in the direction of maximum principal stress was calculated visually with the photo editing software Gimp. The projected area of the hydraulic fractures of A2 and A4 in the direction of maximum principal stress are 0.707 and 0.256 in^2, respectively.

The hydraulically fractured specimens were then thermally fractured for 30 minutes with liquid nitrogen. The resulting fracture morphology is quite complex as can be seen in Figure 3.7. However, the fracture morphology is simplified somewhat by looking at the gross area of the fractures projected in the direction of maximum principal stress. The projected area of the thermal and hydraulic fractures of A2 and A4 in the direction of maximum principal stress are 7.162 and4.82 in^2. The photographic images used to calculate the areas are shown in Figure 3.8. This shows a dramatic increase over the areas of the hydraulic fractures alone and quantifies the new thermally fractured surface area that is perpendicular to the maximum principal stress (see Figure 3.9).

3.4.2 Thermal Fracture Aperture

Hydraulic fractures have apertures that are significantly larger than thermal fractures when the specimens are at uniform room temperature. This is observed in the complete inability to view thermal fractures in any CT scan versus the hydraulic fractures which were readily observed. When acrylic specimens that were fractured both hydraulically and thermally were CT scanned with 35% SSKI solution, the hydraulic fractures were recognizable in the scans while the thermal fractures could not be detected. Additionally, when specimens A2 and A4 were thermally fractured, it was observed that the liquid nitrogen was not able to penetrate the hydraulic fractures until sufficient time had passed for them to widen from thermal contraction. The same is true for the freshly created thermal fractures. By the end of the thermal fracturing experiments, both the thermal and hydraulic fractures were visually confirmed to have liquid nitrogen flowing into them, in A2 and A4.

3.4.3 Kaiser Effect

The Kaiser effect is the phenomena where solids will not emit acoustic events when being stressed at the same level as they were previously [9]. For example, this effect will indicate a threshold during a fatigue compressive loading test that the specimen may have been previously loaded. In the case of the granite specimens this can be seen as an overall reduction in the number and magnitude of AE for thermally fracturing specimens that were already hydraulically fractured versus the blocks that were thermally fractured first (see Figure 3.10). Both specimens, G1 and G2, which were hydraulically fractured first had fewer AE and a reduced total magnitude. Figure 3.11 shows that there are not fewer acoustic events or a decrease in magnitude of the cement paste samples that were previously hydraulically fractured. The lack of difference between the two data sets indicates that the Kaiser effect was not observed in the cement paste specimens. This might be to the length of time between hydraulic and thermal fracturing of these samples.

3.5 Discussion

Thermal fracturing is a process with the potential for creating intricate crack geometries. All fracturing occurs from a given stress state that causes failure. This stress state is controlled by thermoelasticity. Thermoelasticity is the stress caused by a temperature gradient that creates reversible deformation proportional to the coefficient of thermal expansion. For the case of thermal fracturing the thermal properties are slightly more deterministic than the mechanical properties. Both thermal and mechanical properties for the materials used in experimentation and Elba Quartzite, which is the raft river reservoir rock, are found in Table 3.1.

The thermal diffusivity is a material property that reveals how heat flows through stationary media. A higher thermal diffusivity means that a substance will come to thermal equilibrium faster. This means that thermal gradients will be less pronounced and the media will be less likely to thermally fracture. A comparison of the thermal diffusivities of granite, cement paste, and acrylic exposes that acrylic is an order of magnitude lower. Therefore, from a heat transfer point of view acrylic is more likely to thermally fracture and create a more pronounced stress cage than granite, or cement paste.

The thermal fracturing of the cement paste specimen C13 resulted in surface cracks that extended continuously over three sides. This extensive thermal fracturing is better understood when looking at the fracture toughness. The fracture toughness is measure of resistance to crack extension given a preexisting flaw. It is used extensively in linear elastic fracture mechanics (LEFM) which assumes that all materials are flawed. Cement Paste has a fracture toughness that is an order of magnitude lower than acrylic, or granite. The low fracture toughness combined with the high thermal diffusivity caused fairly flat 2-dimensional fracturing.

3.6 Conclusions

1. Fractures were created that have faces that are perpendicular to the maximum principal stress of the isentropic homogeneous bench top acrylic specimens. This result validates the concept that was first presented by Perkins and Gonzalez [1]. Fracture patterns were created by hydraulically fracturing the acrylic specimens, then thermally fracturing them with liquid nitrogen for 30 minutes, all while under a uniaxial load of 1,000 psi.

2. The hydraulic fracture breakdown pressure was almost half in acrylic specimens when they were thermally fractured first.

3. Fractures created in large bench-top experimental specimens can be detected in a medical CT scanner when the proper contrasting agent is used. Which is 35% SSKI for cement paste and Indium Casting Alloy for Granite.

4. Thermal fractures create significant permeability, but almost completely closed when the temperature gradients disappeared.

5. During thermal stimulation, it was found that the Kaiser effect can be used as an indicator of preexisting fractures or previous stress state.

3.6.1 Recommendations

It is recommended that the packer O-rings be compressed by applying an axial force through an interthreaded jack placed concentric to the 1/8 inch tubing. The jack would consist of a metal tube that has an inner diameter of 5/32 inch and outer threads that match the inner threads of a metal sleeve. A ball bearing washer or sufficient lubrication would need to be used to reduce torsion.

It is also recommended that a true tri-axial loading frame be used to continue studying thermal and hydraulic fractures in rock samples.

Figure 3.1: Acrylic specimen A4 loaded in the uniaxial compression machine with thermal packers installed.

Figure 3.2: Hydraulic packer; a. Solid works exploded view b. 4 inch hydraulic packer made of stainless steel tubing and 90 Durameter O-rings with a 1/4 inch outside diameter, c. Packer installed and wedges tightened with 2 inch C-clamp.

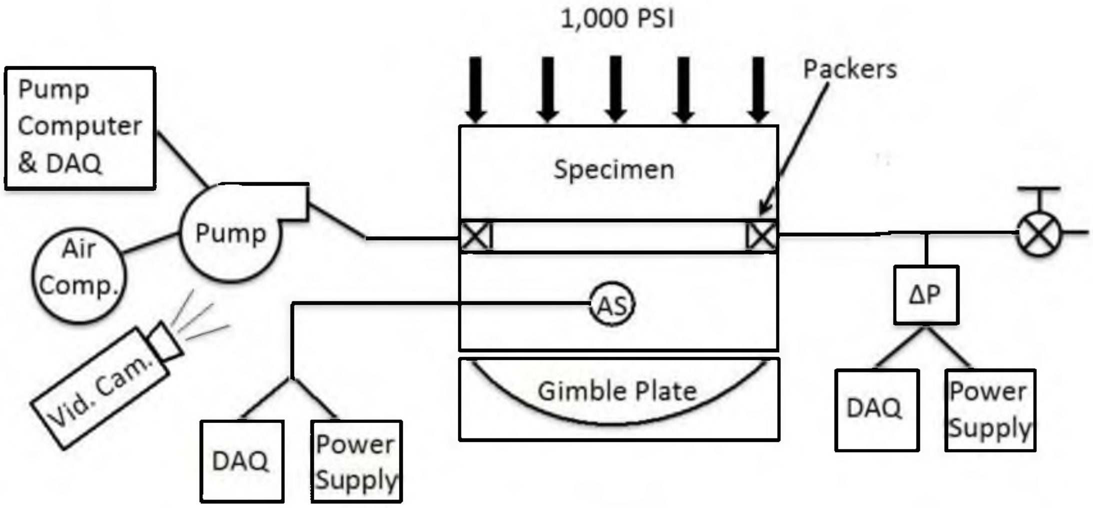

Figure 3.3: Hydraulic fracturing experimental schematic. DAQ is data acquisition, ΔP is the pressure transducer, and AS is the acoustic sensor.

Figure 3.4: Thermal packers made from cotton, super glued to brass tubing with a silicon plug.

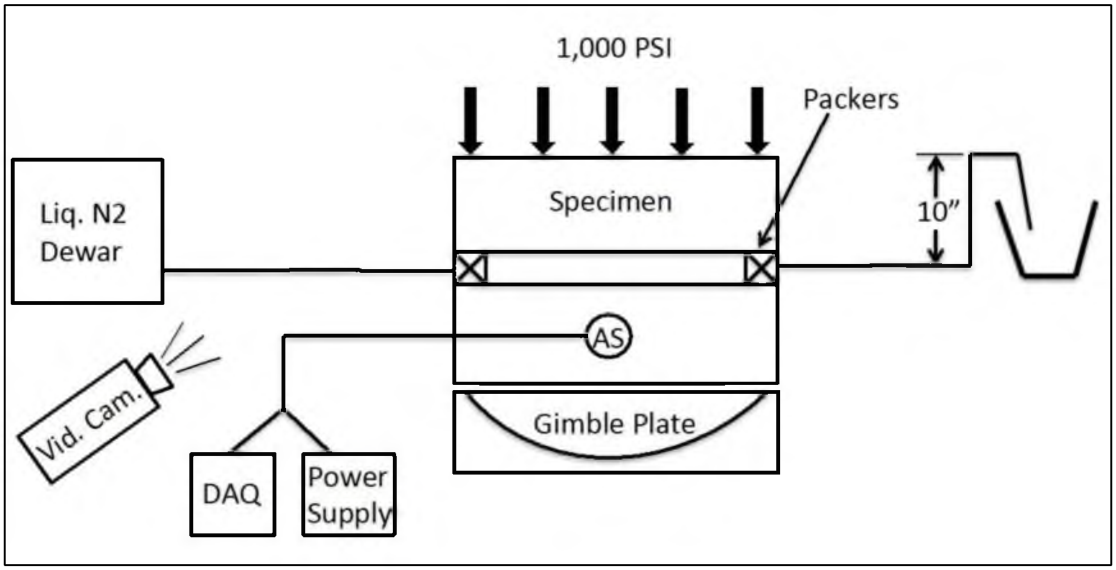

Figure 3.5: Thermal fracturing experimental schematic. DAQ is data acquisition, and AS is acoustic sensor.

Table 3.1: Material properties.

Property	Symbol	Units	Cement Paste	Acrylic	Granite	Elba Quartzite	Water	Liquid N2
Viscosity	μ	Ns/m^2	N/A	N/A	N/A	N/A	28500	17680
Thermal Conductivity	k	W/m K	2.181	0.190	3.444	4.000	0.592	0.141
Density	ρ	kg/m^3	2060	1190	2681	2610	1000	808
Specific Heat	Cp	J/kg K	945	1470	837	1130	4200	3077
Thermal Diffusivity	K	cm^2/hr	1.120E-06	1.086E-07	1.534E-06	1.356E-06	1.409E-07	5.687E-08
Linear Coefficient of Thermal Expansion	α	1/K	1.20E-05	7.20E-05	6.16E-06	3.30E-05	N/A	N/A
Poisson Ratio	ν	Unitless	0.15	0.35	0.23	0.28	N/A	N/A
Young's Modulus	E	Pa	2.50E+10	3.10E+09	2.14E+10	1.09E+10	N/A	N/A
Ultimate Compressive Strength	Com	Pa	1.50E+07	1.21E+08	2.07E+08	2.10E+08	N/A	N/A
Fracture Toughness	K1C	Pa m^1/2	3.E+05	1.E+06	2.E+06	2.E+06	N/A	N/A

Table 3.2 Hydraulic and thermal fracture experimental highlights. Breakdown pressure for G2 was not recorded.

Sample	Sequence	Time Thermally Fractured (minutes)	Hydraulic Breakdown pressure (psi)	Breakdown Flow Rate (ml/minute)
A1	T - H	15	930	3
A2	H - T	30	4710	5
A3	T - H	8.5	1315	1
A4	H - T	30	3501	1
C10	H - T	30	519	5
C11	T - H	30	571	5
C12	H - T	30	622	5
C13	T	30	N/A	N/A
G1	H -T	30	2201	5
G2	H -T	30	1500 ?	20
G3	T - H	30	1286	1
G4	T - H	30	2248	1

Table 3.3 CT, Photograph, and acoustic event outcomes from the experimentation.

Sample	Test	CT Scan/ Photo Analysis Successful	Acoustic Emissions Successful	Test	CT Scan/ Photo Analysis Successful	Acoustic Emissions Successful
A1	T	Yes	N/A	H	Yes	N/A
A2	H	Yes	N/A	T	Yes	N/A
A3	T	Yes	N/A	H	Yes	N/A
A4	H	Yes	N/A	T	Yes	N/A
C10	H	Yes	No	T	No	Yes
C11	T	No	Yes	H	Yes	Yes
C12	H	Yes	No	T	No	Yes
C13	T	Yes	Yes	N/A		
G1	H	No	Yes	T	Yes	Yes
G2	H	No	Yes	T	Yes	Yes
G3	T	No	Yes	H	No	Yes
G4	T	No	Yes	H	Yes	No

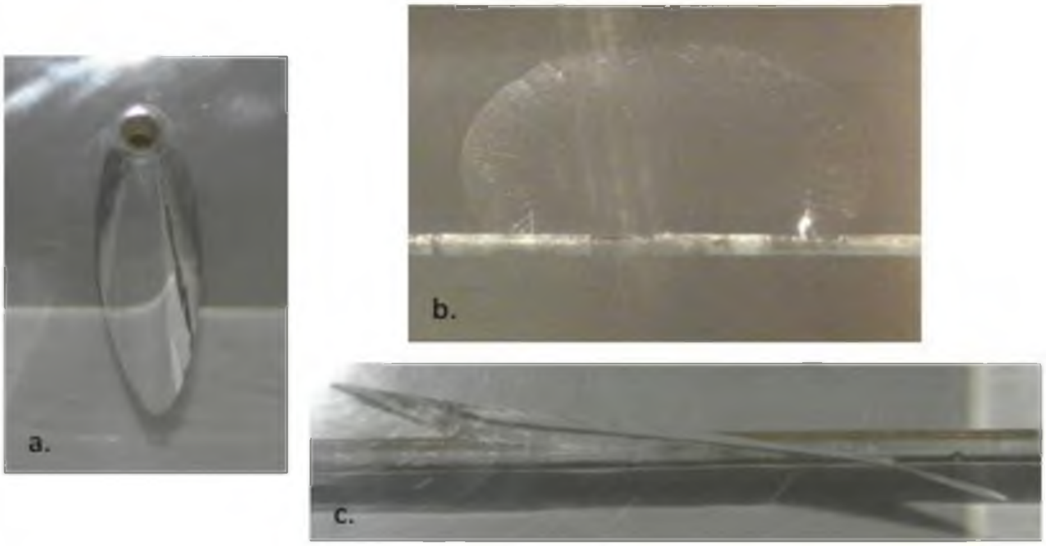

Figure 3.6: Hydraulic fracture of A2 in a. axial direction, b. horizontal direction, and c. maximum principal stress direction.

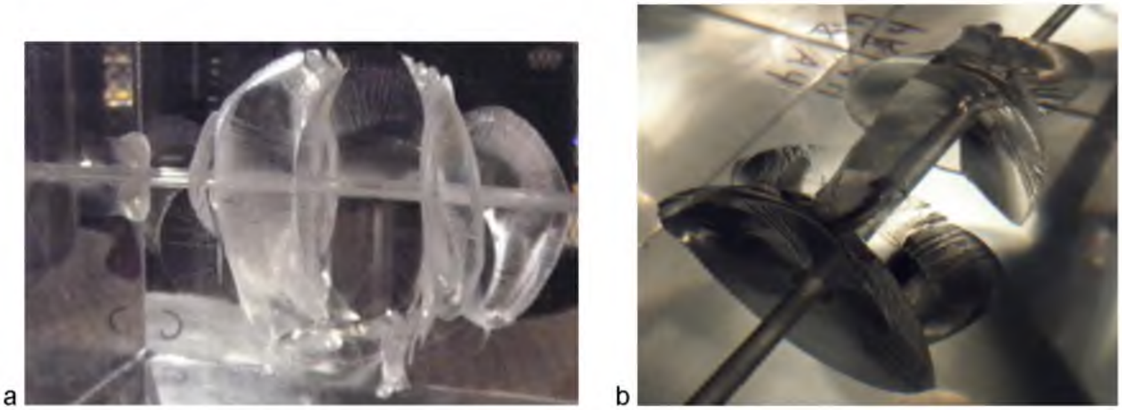

Figure 3.7: Thermal fracture after hydraulic fracture of; a. A2, and b. A4. Views are intended to highlight the complexity of the fracture geometries.

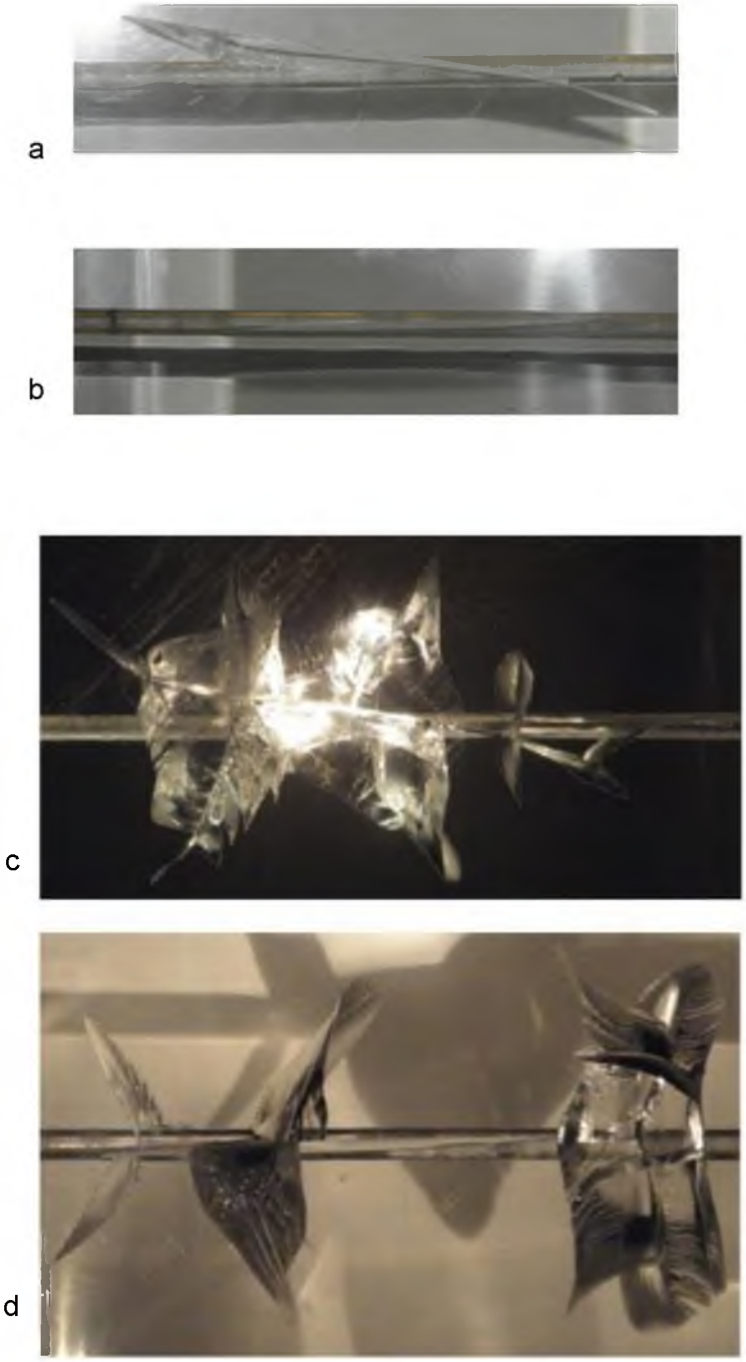

Figure 3.8: Fracture evaluation of specimens A2 and A4 comparing hydraulic fractures to thermal fractures created after the hydraulic fracture. All photographs are taken in the orientation of the applied maximum principal stress (1,000 psi). a. A2 hydraulic fracture, b. A4 hydraulic fracture, c. A2 thermal fracture post hydraulic fracture, d. A4 thermal fracture post hydraulic fracture.

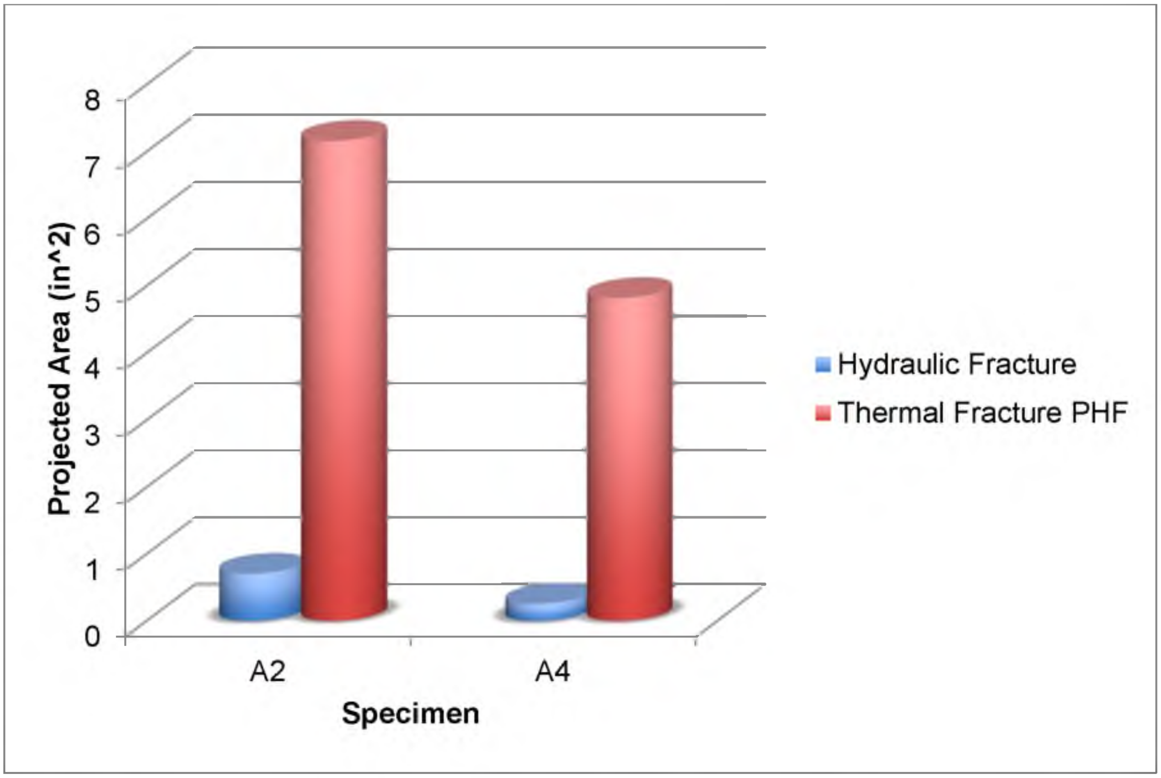

Figure 3.9: Projected area of fractures in the maximum principal stress direction for acrylic samples A2 and A4.

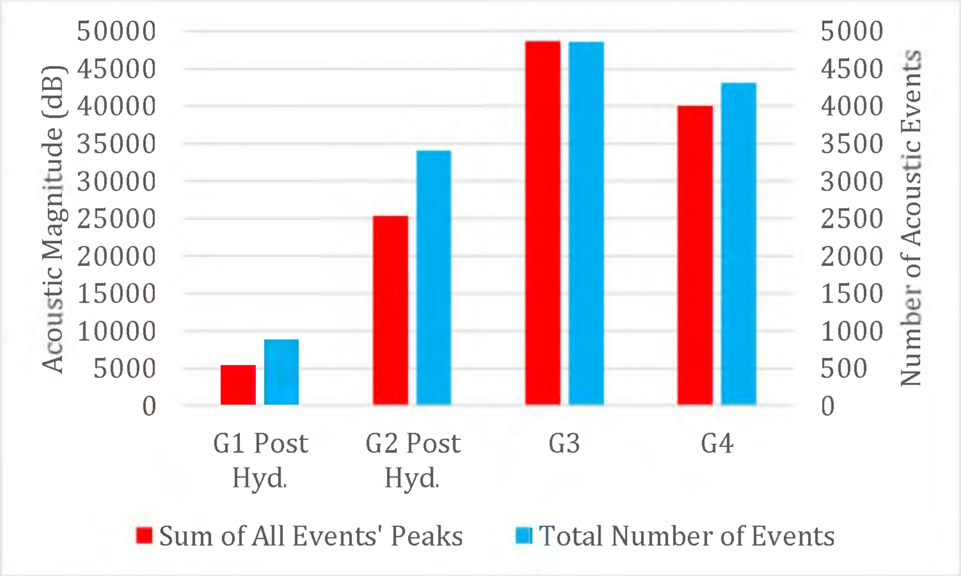

Figure 3.10: Summation of the magnitude and total number of acoustic events during the thermal fracture experiments of the granite specimens.

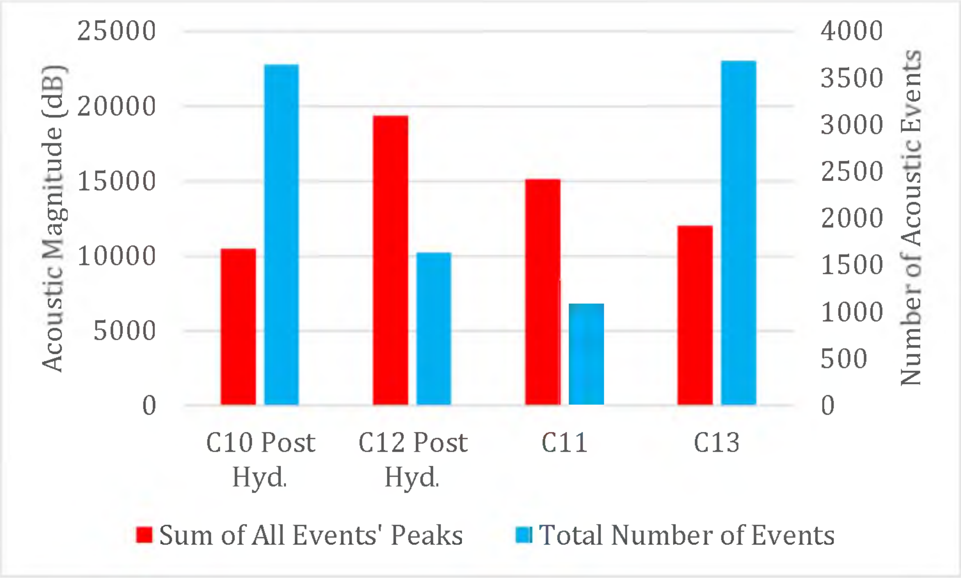

Figure 3.11: Summation of the magnitude and total number of acoustic events during the thermal fracture experiments of the cement paste specimens.

3.7 References

[1] Perkins, T.K., and Gonzalez, J.A., 1985, “The Effect of Thermoelastic Stresses on Injection Well Fracturing,” J. SPE, pp. 78-88.

[2] Sanyal, S.K. and Butler, S.J., 2005, “An Analysis of Power Generation Prospects from Enhanced Geothermal Systems.” Geotherm. Resour. Counc. Trans., **29**.

[3] MIT, 2006. The future of Geothermal Energy. Impact of Enhanced Geothermal Systems (EGS) on the United States in the 21st Century. Assessment by a Massachusetts Institute of Technology-led Interdisciplinary Panel (J.F. Tester, Chairman), 372 pp. from http://geothermal.inel.gov/publications/future_of_geothermal_energy.pdf

[4] Dulieu-Barton, J. M. and Stanley, P., 1998 “Development and Applications of Thermoelastic Stress Analysis,” J. Strain Anal., 1998, **33**(2), 93-104.

[5] Perkins, T.K. and Gonzalez, J.A., 1984, “Changes in Earth Stresses Around a Wellbore Caused by Radially Symmetrical Pressure and Temperature Gradients,” J. SPE, pp. 129-40.

[6] Ghassemi, A., 2007, Stress and Pore Pressure Distribution Around a Pressurized, Cooled Crack in Low Permeability Rock, *Proc. 32nd Stanford Geothermal Workshop*, Stanford University, Stanford, pp. 1-23.

[7] McLennan, J.D., (1980), “Hydraulic Fracturing: A Fracture Mechanics Approach,” Ph.D. thesis, University of Toronto, Toronto, Canada.

[8] Tran, D.T., “Stress Fields in The Raft River Geothermal Reservoir Area,” Quarterly Report for DOE, Raft River Project, (March 2010).

[9] Lockner, D., 1993, “The Role of Acoustic Emission in the Study of Rock Fracture,” Int. J. Rock Mech. Min. Sci. Geomech., **30**(7), pp. 883-899.

[10] Sanchez, S., June 2014, Schlumberger Employee, Terratek, private communication.

[11] Doyle, J.F., Phillips, J.W., 1989, Manual on Experimental Stress Analysis, Society for Experimental Mechanics, Chap. 6.

[12] Daehnke, A., Kouzniak, N., Rossmanith, H.P., and Knasmillner, R.E., 1997, “Blast-Induced Fracturing Around Boreholes and Gas-Pressurised Rapid Crack Extension,” In ICF 9 – Sydney, Australia,from http://www.gruppofrattura.it/ocs/index.php/ICF/ICF9/paper/viewFile/4347/1507.

[13] Bradford, J., 2015, PhD. Candidate Research Engineer, Energy and Geoscience Institute, private communication.

[14] Craig, S.L., Udell, K.S., 2009, “Enhanced Heat Transfer from Geothermal Systems Using Pressure Cycling,” *Geothermal Resource Council Proc.*, Reno, NV, Oct. 2009.

[15] Touloukian, Y. S., and C. Y. Ho, Eds., 1970-1977, *Thermophysical Properties of Matter, The TPRC Data Series* (13 volumes on Thermophysical properties: thermal conductivity, specific heat, thermal radiative, thermal diffusivity, and thermal linear expansion), Plenum Press, NY.

[16] Weast, R.C., Ed., 1980, *CRC Handbook of Chemistry and Physics*, 60th ed., CRC Press, Inc., Boca Ratan, FL.

[17] Smith, M, March 2010, Employee, Rock of Ages Corp., Barre, Vermont, private communication.

[18] Thomas, F., Nov. 2009, Employee, Interstate Plastics, Sacramento, CA, private communication.

[19] Physical Properties of Acrylite GP Acrylic Sheet, from http://www.sdplastics.com/acryliteliterature/1235EGPPhysicalProperties.pdf.

[20] Lee, K.M., and An, K.S., “Factors Influencing Fracture Toughness of Mortar-Aggregate Interface in Concrete,” *Frac. Mech. Concrete Structures*, Freiburg, Germany, pp. 193-202, from http://framcos.org/FraMCoS-3/1-2-12.pdf.

[21] Marshall, G.P., and Williams, J.G., 1973, “The Correlation of Fracture Data for PMMA,” J. Mater. Sci., **8,** pp. 138-140.

[22] Alehossein, H., and Boland, J.N., 2004, “Strength, Toughness, Damage and Fatigue of Rock,” *Structural Integrity and Fracture*, from http://eprint.uq.edu.au/archive/00000836.

CHAPTER 4

THERMAL FRACTURE NUCLEATION SIMULATED FROM A FINITE DIFFERENCE THERMOELASTIC MODEL BASED ON LINEAR ELASTIC FRACTURE MECHANICS

4.1 Introduction

To gain insight into the workings and unique phenomena that occur during hydraulic and thermal fracturing of impermeable, homogeneous, and isotropic reservoirs, physical experiments and computational simulations have been conducted. Blocks of granite, acrylic, and cement paste with dimensions of 8 by 8 by 12.5 inches, and a 1/4 inch through hole were hydraulically and thermally fractured under a uniaxial load of 1,000 lbs. perpendicular to the hole axis. A finite difference code was created to simulate a continuous, impermeable, and homogeneous reservoir. This code can determine fracture initiation, stress state, displacement, and temperature distribution based on in-situ, far-field, and thermoelastic conditions.

The purpose of this computational work is to study thermal fractures and understand the extent to which they contributed to the fracture networks observed experimentally. The experiments were arranged with a uniaxial load positioned perpendicular to the axis with the other surfaces being traction free. This was done as a way to simulate the differential horizontal stresses (1,000 psi) found at the Raft River Geothermal Site. This set up provided a unique opportunity for thermal fractures to grow either axially or circumferentially depending on the alignment of stresses and surface flaws.

Thermoelastic stresses cause unique nonlinear, localized stresses near the wellbore. These stresses are similar to those resulting from residual stresses or variable distributed loading on a crack face. During the thermal fracturing of acrylic blocks, the dominant feature observed were the creation of circumferential cracks. This is true even in blocks that already contain axial hydraulic fractures. There are several things that affect this including: residual stresses, and initial flaw size, geometry, and orientation from casting and drilling, and thermal stresses. Thermal stresses have been modeled using a thermoelastic finite difference code.

4.2 Reservoir Geometry

A cylindrical coordinate system was chosen because it best represents a circular hole and surrounding media. The assumption of axisymmetry is used to simplify the geometry to a 2-dimensional point of interest. Axisymmetry is valid when there is no change in temperature or stress with angle. While this is always true for temperature the stress state can reach a solution by imposing the assumption of superposition. The superposition principle, valid for homogenous isotropic elastic media, states that stress and stress intensity's are additive. Figure 4.1 shows the r and z plane along with the corresponding nodes that were used to discretize the governing equations. Each of the 15 different node types represents a different nodal space. Node types 7-9 are split nodes, having two equations for each node. They are split because they are on the boundary of the solid matrix and the hole and therefore have to have two different discretized equations to represent the two different domains. There are nine different nodes for the solid media and nine nodes for the hole. The difference between the nodal equations will be explained later.

4.3 Temperature in the Solid Media

To determine the temperature distribution in the solid media, conduction heat transfer was solved by means of Fourier's Law in conjunction with the conservation of energy principle. Equation 4.1 is the result in cylindrical coordinates for the axisymmetric case, known as the Heat Equation.

$$\frac{1}{r}\frac{\partial}{\partial r}\left(r\frac{\partial T}{\partial r}\right)+\frac{\partial^2 T}{\partial z^2}=\frac{1}{\alpha}\frac{\partial T}{\partial t} \tag{4.1}$$

where T is temperature, r is radius, z is the axial length and t is time. The control volume approach was used to discretize the equation 4.1. Each control volume balances the energy stored with the energy conducted through its faces. This provides an explicit dynamic solution of temperature that is solved for each node in ascending order. Node 5 is an interior node. Nodes 1-4, and 6-9 are boundary nodes.

The code is set up so that the boundaries at z equal to zero and length, and r equal to the outer radius, can be held at a constant temperature (Dirichlet) or insulated (Neumann). The boundary at r equal to the inner radius can be set up for fluid flow, constant heat flux, constant temperature, or with a constant heat convection coefficient. These conditions can be set to the whole or partial length of the inner radius with the rest of it being held at a constant temperature or insulated. The versatility of the code allows for different conditions to be run. This is useful in the verification process. The verifications can be found in Appendix E.

For the application of using this code to simulate a geothermal reservoir the semi-infinite condition is used. In this state, the boundary conditions at z equal to zero and length are insulated. At r equal to the outer radius the boundary condition can be either constant temperature or insulated. A stopping condition has to exist that stops the code once a change in temperature reaches the outer radius. The outer radius has to be set large enough that the code has enough time to run. This is dependent on the thermal diffusivity of the material.

Fluid flow is the only temperature boundary condition that utilizes nodes 7-15. The temperature within the fluid was calculated using the assumption of laminar plug fluid flow that is driven based on equilibrium of momentum, which accounts for advection and conduction between surrounding nodes.

4.3.1 Boiling Heat Transfer

Boiling heat transfer is a complex process that is extremely nonlinear. Through the shifts from film to transitional and finally to nucleate boiling, the heat flux varies widely. The specific quantities of which depend on the thermal and physical properties of the liquid and solid. Complete solutions for the heat transfer through the different boiling regimes do not exist. A constant temperature is a close approximation but has the downside of causing an artificial spike in the thermal stresses from the instantaneous temperature change. A coefficient that relates temperature change to the heat flux is used to moderate the constant temperature assumption.

4.4 Thermoelasticity

The stresses for both the experimental specimens and the reservoirs they represent are found by applying the thermoelastic relationships on a finite hollow cylinder. The finite difference code is a derivation of the Navier-Cauchy stress-displacement equations of equilibrium. The Navier-Cauchy equations are derived from applying the strain-displacement equations into Hooke's law and then applying that to the equilibrium equations. The fundamental assumptions for the Navier-Cauchy equations are that:

1. The temperature is solved independently of the deformations of the body.
2. Small deformations.
3. Linear Elastic medium.

The Navier-Cauchy equations in the cylindrical coordinate system for an axisymmetric thermoelastic cylinder in the radial (r) and axial (z) direction without body forces according to Noda et al. [1] are shown in equations 4.2 and 4.3, respectively. Equations 4.4 and 4.5 are the axisymmetric Laplacian operator and the dilations, respectively. In these equations *u* and *w* are the displacements in the radial and axial direction respectively. Nu is the poison ratio, and alpha is the linear coefficient of thermal expansion. Equation 4.6 clarifies the sign convention of equations 4.2 and 4.3. Substituting in these equations along with the simplifying equations a1 (4.7) and a2 (4.8) the results are equations 4.9 and 4.10.

Radial

$$\nabla^2 u - \frac{u}{r^2} + \frac{1}{1-2v}\frac{\partial e}{\partial r} - 2\left(\frac{1+v}{1-2v}\right)\alpha\frac{\partial \tau}{\partial r} = 0 \tag{4.2}$$

Axial

$$\nabla^2 w + \frac{1}{1-2v}\frac{\partial e}{\partial z} - 2\left(\frac{1+v}{1-2v}\right)\alpha\frac{\partial \tau}{\partial z} = 0 \tag{4.3}$$

Where:

$$\nabla^2 = \frac{\partial^2}{\partial r^2} + \frac{1}{r}\frac{\partial}{\partial r} + \frac{\partial^2}{\partial z^2} \tag{4.4}$$

And

$$e = \frac{\partial u}{\partial r} + \frac{u}{r} + \frac{\partial w}{\partial z} \tag{4.5}$$

$$\tau = T - T_{initial} \tag{4.6}$$

$$a_1 = \frac{1}{1-2\nu} \tag{4.7}$$

$$a_2 = 2\left(\frac{1+\nu}{1-2\nu}\right)\alpha \tag{4.8}$$

$$(1+a_1)\frac{\partial^2 u}{\partial r^2} + \frac{\partial^2 u}{\partial z^2} + \frac{\partial^2 w}{\partial z \partial r} + (1+a_1)\frac{1}{r}\frac{\partial u}{\partial r} - (1+a_1)\frac{u}{r^2} = a_2\frac{\partial T}{\partial r} \tag{4.9}$$

$$(1+a_1)\frac{\partial^2 w}{\partial z^2} + \frac{\partial^2 w}{\partial r^2} + a_1\frac{\partial^2 u}{\partial z \partial r} + \frac{1}{r}\frac{\partial w}{\partial r} + \frac{a_1}{r}\frac{\partial u}{\partial z} = a_2\frac{\partial T}{\partial z} \tag{4.10}$$

These equations, radial 4.9 and axial 4.10, are coupled elliptical 2nd order partial differential equations with two dependent variables and two independent variables. Because of this only approximate solutions exist. The method of approximating the solution used in this paper is finite difference. The Navier-Cauchy equations that represents equilibrium in the radial and axial directions (equations 4.9 and 4.10) were discretized. Equations 4.11 and 4.12 are the discretized forms of equations 4.9 and 4.10 for the central node 5. They were discretized using the central differencing Taylor-series formulation.

$$\begin{aligned} u_{(i,j)} = \frac{1}{\left(\frac{2(1+a_1)}{\Delta r^2} + \frac{2}{\Delta z^2} - \frac{(1+a_1)}{{r_{(i)}}^2}\right)} \Bigg[& \frac{(1+a_1)}{\Delta r^2}\left(u_{(i-1,j)} + u_{(i+1,j)}\right) + \frac{1}{\Delta z^2}\left(u_{(i,j+1)} + u_{(i,j-1)}\right) \\ & + \frac{1}{4\Delta z \Delta r}\left(w_{(i+1,j+1)} - w_{(i+1,j-1)} - w_{(i+1,j-1)} + w_{(i-1,j-1)}\right) \\ & + \frac{(1+a_1)}{2r_{(i)}\Delta r}\left(u_{(i+1,j)} - u_{(i-1,j)}\right) - \frac{a_2}{2\Delta r}\left(T_{(i+1,j)} - T_{(i-1,j)}\right) \Bigg] \end{aligned} \tag{4.11}$$

$$w_{(i,j)} = \frac{1}{\left(\frac{2(1+a_1)}{\Delta z^2} + \frac{2}{\Delta r^2}\right)} \left[\frac{(1+a_1)}{\Delta z^2} \left(w_{(i,j+1)} + w_{(i,j-1)} \right) + \frac{1}{\Delta r^2} \left(w_{(i+1,j)} + w_{(i-1,j)} \right) \right.$$
$$+ \frac{a_1}{4 \Delta z \Delta r} \left(u_{(i+1,j+1)} - u_{(i+1,j-1)} - u_{(i-1,j+1)} + u_{(i-1,j-1)} \right) + \frac{1}{2 r_{(i)} \Delta r} \left(w_{(i+1,j)} - w_{(i-1,j)} \right)$$
$$\left. + \frac{a_1}{2 r_{(i)} \Delta z} \left(u_{(i,j+1)} - u_{(i,j-1)} \right) - \frac{a_2}{2 \Delta z} \left(T_{(i,j+1)} - T_{(i,j-1)} \right) \right] \tag{4.12}$$

The boundary conditions at *r* equal to the inner and outer radius are that radial stress and axial shear are zero. This is known as a traction free surface condition. The corresponding boundary conditions at *z* equal to zero and *L*, are *du/dz* and *dw/dz* are zero. These conditions are applied to the equilibrium equations and rediscretized for radial and axial displacements. On the corners all of these conditions apply. The equations for the edge nodes are also discretized using a forward or backward differencing scheme so that nodes used in the displacement equation are in real space. Additionally the system of equations is solved implicitly which makes it stable. In order to come to a single solution, one node's axial displacement must be set to zero. The node chosen for the datum displacement of zero is the center node at the outer radius.

4.4.1 3-Dimensional Stress by Superposition

In order to take the 2-dimensional stress state calculated in the thermoelastic model and apply 3-dimensional stresses, superposition is utilized. Daneshy [2] provided the equations necessary for 3-dimensional cylindrical stresses around a borehole that is orthogonal to the far field stresses. They are found in equations 4.13 through 4.18. It is important to note that theta is oriented parallel to sigma 11 when equal to zero. These equations were quantized and added to the thermoelastic stresses calculated in the finite difference code.

$$\sigma_{rr} = \left[\frac{\sigma_{11}+\sigma_{22}}{2} \left(1 - \frac{a^2}{r^2}\right) + \frac{\sigma_{11}-\sigma_{22}}{2} \left(1 + 3\frac{a^4}{r^4} - 4\frac{a^2}{r^2}\right) \cos 2\theta + \sigma_{12} \left(1 + 3\frac{a^4}{r^4} - \right.\right.$$
$$\left.\left. 4\frac{a^2}{r^2}\right) \sin 2\theta \right] - \left[p_w \frac{a^2}{r^2} \right] \tag{4.13}$$

$$\sigma_{\theta\theta} = \left[\frac{\sigma_{11}+\sigma_{22}}{2} \left(1 + \frac{a^2}{r^2}\right) - \frac{\sigma_{11}-\sigma_{22}}{2} \left(1 + 3\frac{a^4}{r^4}\right) \cos 2\theta - \sigma_{12} \left(1 + 3\frac{a^4}{r^4}\right) \sin 2\theta \right] + \left[p_w \frac{a^2}{r^2} \right] \tag{4.14}$$

$$\sigma_{zz} = \left[\sigma_{33} - \nu\left\{2(\sigma_{11} - \sigma_{22})\frac{a^2}{r^2}\cos 2\theta + 4\sigma_{12}\sin 2\theta\right\}\right] \quad (4.15)$$

$$\sigma_{r\theta} = \left[\frac{\sigma_{11}-\sigma_{22}}{2}\left(1 - 3\frac{a^4}{r^4} + 2\frac{a^2}{r^2}\right)\sin 2\theta + \sigma_{12}\left(1 - 3\frac{a^4}{r^4} + 2\frac{a^2}{r^2}\right)\cos 2\theta\right] \quad (4.16)$$

$$\sigma_{\theta z} = \left[(-\sigma_{13}\sin\theta + \sigma_{23}\cos\theta)\left(1 + \frac{a^2}{r^2}\right)\right] \quad (4.17)$$

$$\sigma_{rz} = \left[(\sigma_{13}\cos\theta + \sigma_{23}\sin\theta)\left(1 - \frac{a^2}{r^2}\right)\right] \quad (4.18)$$

It is of interest to note that a rise in hydraulic pressure would only create axial fractures. This is seen specifically in the lack of a pressure term for axial stress, equation 4.15.

4.5 Linear Elastic Fracture Mechanics

Linear elastic fracture mechanics (LEFM) theory was used to determine the fracture nucleation and orientation. The basic equation for the Irwin stress intensity factor in LEFM is equation 4.19.

$$K_{1C} = f(a)\sigma\sqrt{\pi a} \quad (4.19)$$

where K_{1C} is the Fracture Toughness of the material in mode 1 tensile fracturing, σ is the farfield applied stress, a is the fracture length, and f(a) is the geometric correction factor. Fracture growth is initiated when the right side of equation 4.19 exceeds the fracture toughness. For common loading geometries there are many compilations of stress intensity factors [3-7]

Thermoelastic stresses cause unique, nonlinear localized stresses near the wellbore. These stresses are similar to those resulting from residual stresses or variable distributed loading on a crack face. In both cases Bueckner's principle was used to solve for the stress intensity factor. Residual stresses were solved by Tada, Paris, and Irwin [3] and variable distributed loading on a crack face was solved by Rooke and Cartwright [6]. Bueckner developed the idea that the stress intensity factor could be calculated by integrating the stress times a weighted geometric factor over the length of the crack [8]. Equation 4.20 is the generic form of the application of Bueckner's principle. The outcome of Bueckner's principle are the Green's Function in LEFM and the Weight Functions. The two differences between these functions, are how the geometric factor is obtained and multiplying by the square route of πa [9].

$$K_I = \frac{1}{\sqrt{\pi a}} \int_0^a \sigma(x) G(x,a) dx \quad (4.20)$$

Where a is the edge crack length, *σ(x)* is the tensile opening stress perpendicular to the crack face, and *G(x,a)* is the geometry factor.

In this work the Weight Function utilized by Lecampion, Abbas and Prioul [10] was used to determine the stress intensity factor of the blocks (see equation 4.21).

$$K_1 = \frac{2\sqrt{\pi l_o}}{\pi} \int_0^{l_o} \frac{p(x)}{l_o\sqrt{1-(x/l_o)^2}} \left(\frac{x/l_o + r_i/l_o}{1 + r_i/l_o}\right)^{d-1} \left(1 + 0.3\left(1 - \frac{x}{l_o}\right)\left(\frac{1}{1 + l_o/r_i}\right)^4\right) dx \quad (4.21)$$

Where l_o is the crack length, *p(x)* is the net stress acting on the crack face, r_i is the hole radius, *x* is abscissa along the fracture starting at zero at r_i, and *d* being a geometric coefficient. For axial fractures *d* is equal to 1 and for circumferential fractures *d* is equal to 2.

4.6 Results

The results of the numerical simulation indicate a stress field that is more favorable toward the creation of axial fractures; see Figures 4.2, 4.3, 4.4, and Table 4.1. These results were obtained by simulating cement paste, acrylic, and granite with the properties listed in Table 3.1. The outer radius was set to a constant temperature, the initial temperature. The simulation time was set for three minutes and the flaw size was varied to determine what the critical size is under these conditions. It is observed that cement paste requires circumferential flaws greater than 2.5 times the size of axial to cause fracturing in that orientation. Acrylic need circumferential flaws 4 times larger and granite was not able to fracture circumferentially with a maximum flaw size of 1 mm.

Therefore it is determined that initial flaws from drilling play a large role in the creation of these circumferential cracks. Bowman [11] studied the fatigue life of polycarbonate sheets with drilled holes. As part of the study axial and circumferential surface roughness was measured on 8 different techniques of hole drilling. They found in all cases that the circumferential surface roughness was twice that of the axial and that manual drilling (as opposed to automated) produced ten times the roughness.

The stress intensity factor of the uniform temperature blocks was determined and found to not exceed the fracture toughness for any of the materials. The thermal fracturing observed during the experiments took place by exposing a section of the sample borehole to liquid nitrogen for 30 minutes. Figure 4.5 shows a comparison of the temperature along the center in the z direction, and r location varying from the inner radius to the outer edge. These calculations were obtained with the outer radius being held at the initial temperature of the block. The similar thermal conductivities and specific heats of granite and cement paste result in similar temperature profiles. The acrylic on the other hand is quite different. It has a higher slope of temperature near the wellbore which causes a higher thermal stresses, as shown in Figures 4.6 and 4.7. The higher stress cage will result in more drastic fracturing. This was seen experimentally and is now more fully understood. Figures 4.8, 4.9, and 4.10 are the 2-dimensional temperature profiles at 30 minutes of liquid nitrogen exposure. The tighter temperature cage is seen in Figure 4.8 compared to the more diffuse profiles in Figures 4.9 and 4.10 supporting the results in Figures 4.6 and 4.7.

4.7 Conclusions

A finite difference thermoelastic numerical model with a linear elastic fracture mechanics application was created. It has the capability of applying various types of heat transfer and evaluating the thermal stresses and fracture nucleation potential. From these calculations it was concluded that the circumferential fractures that were created experimentally in acrylic occurred from flaws that are at least four times larger in that orientation from drilling.

Temperature profiles of the cement paste, acrylic, and granite specimens were calculated after 30 minutes of liquid nitrogen exposure. These profiles revealed a well defined temperature cage in the acrylic specimens that accounts for the drastic thermal fractures that were observed experimentally. In order to create thermal fractures in geologic reservoirs that are perpendicular to the maximum horizontal principal stress, half an order of magnitude larger flaws or preexisting fractures would have to exist in that orientation than features parallel to the maximum horizontal principal stress.

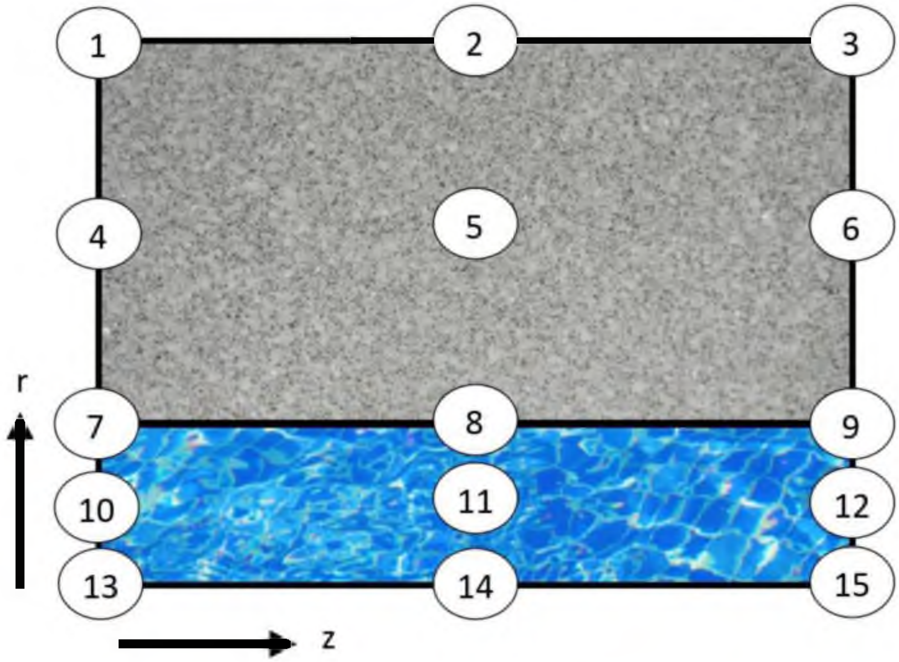

Figure 4.1: The r and z plane of the simulated impermeable media and hole.

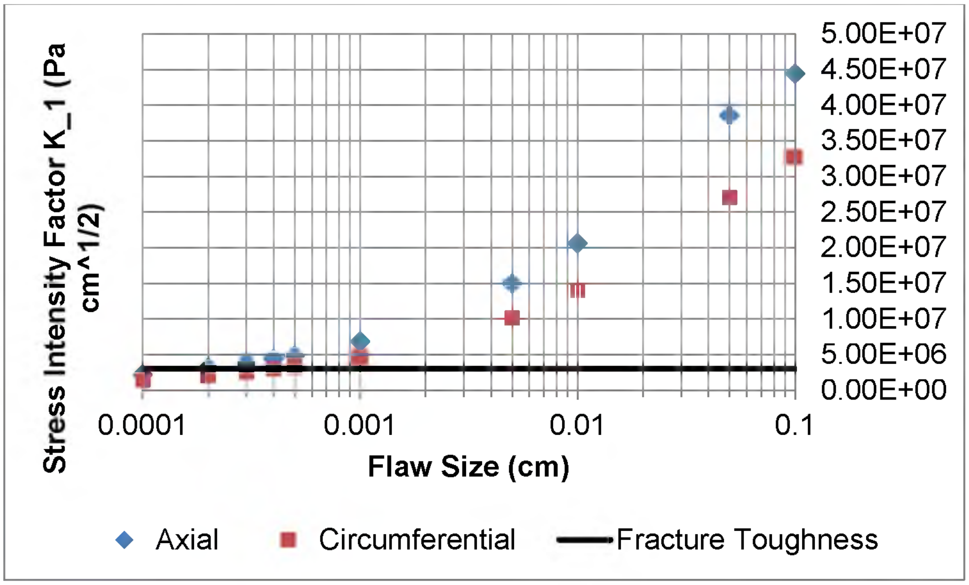

Figure 4.2: Stress intensity factor versus flaw size of cement paste. The fracture toughness for cement paste is 3.0 x 10^6 Pa $cm^{1/2}$.

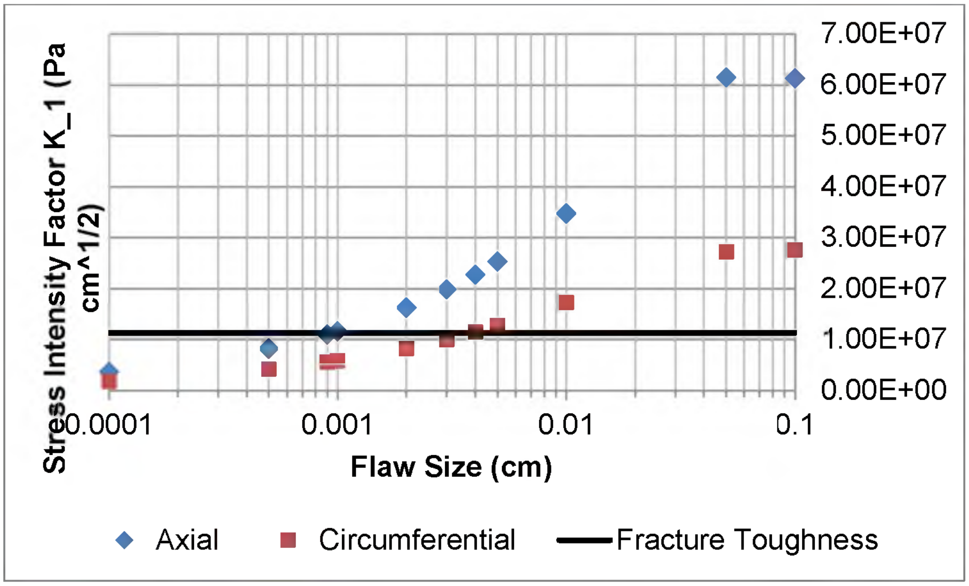

Figure 4.3: Stress intensity factor versus flaw size of acrylic. The fracture toughness for acrylic is 1.13 x 10^7 Pa $cm^{1/2}$.

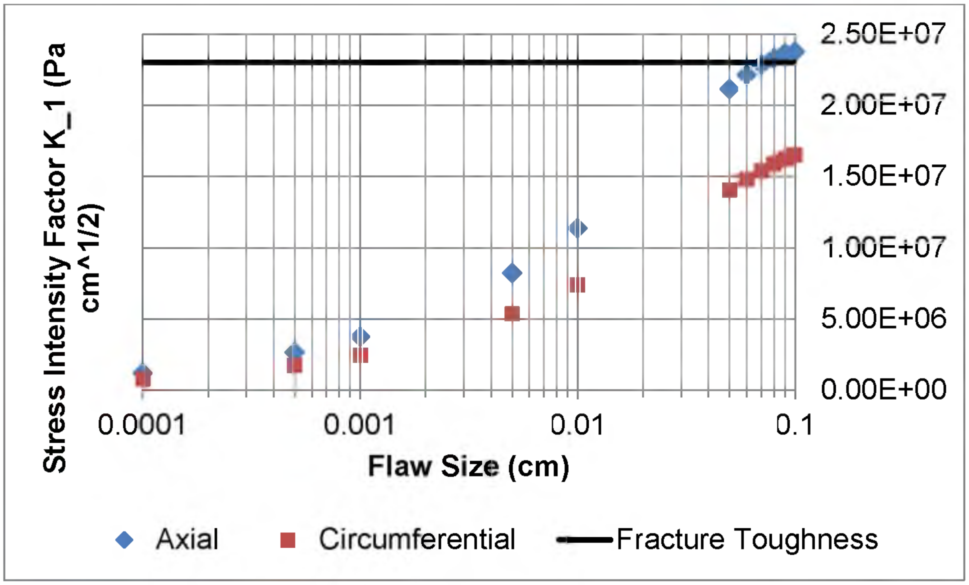

Figure 4.4: Stress intensity factor versus flaw size of granite. The fracture toughness for granite is 2.3 x 10^7 Pa $cm^{1/2}$.

Table 4:1 Results of stress intensity versus flaw size.

Cement Paste			Acrylic			Granite		
Flaw Size (cm)	Stress Intensity (Pa cm$^{1/2}$)		Flaw Size (cm)	Stress Intensity (Pa cm$^{1/2}$)		Flaw Size (cm)	Stress Intensity (Pa cm$^{1/2}$)	
	Axial	Circ.		Axial	Circ.		Axial	Circ.
0.0001	2.16E+06	1.46E+06	0.0001	3.67E+06	1.87E+06	0.0001	1.19E+06	7.74E+05
0.0002	3.05E+06	2.06E+06	0.0005	8.19E+06	4.17E+06	0.0005	2.65E+06	1.73E+06
0.0003	3.74E+06	2.52E+06	0.0009	1.10E+07	5.58E+06	0.001	3.74E+06	2.44E+06
0.0004	4.31E+06	2.91E+06	0.001	1.16E+07	5.88E+06	0.005	8.21E+06	5.35E+06
0.0005	4.82E+06	3.26E+06	0.002	1.63E+07	8.24E+06	0.01	1.13E+07	7.39E+06
0.001	6.80E+06	4.59E+06	0.003	1.98E+07	1.00E+07	0.05	2.11E+07	1.40E+07
0.005	1.49E+07	1.01E+07	0.004	2.27E+07	1.15E+07	0.06	2.21E+07	1.48E+07
0.01	2.06E+07	1.40E+07	0.005	2.53E+07	1.27E+07	0.07	2.28E+07	1.54E+07
0.05	3.85E+07	2.70E+07	0.01	3.47E+07	1.73E+07	0.08	2.33E+07	1.59E+07
0.1	4.44E+07	3.27E+07	0.05	6.15E+07	2.72E+07	0.09	2.36E+07	1.62E+07
			0.1	6.12E+07	2.76E+07	0.1	2.38E+07	1.65E+07
Fracture Toughness	(Pa cm$^{1/2}$)	3.00E+06	Fracture Toughness	(Pa cm$^{1/2}$)	1.13E+07	Fracture Toughness	(Pa cm$^{1/2}$)	2.30E+07

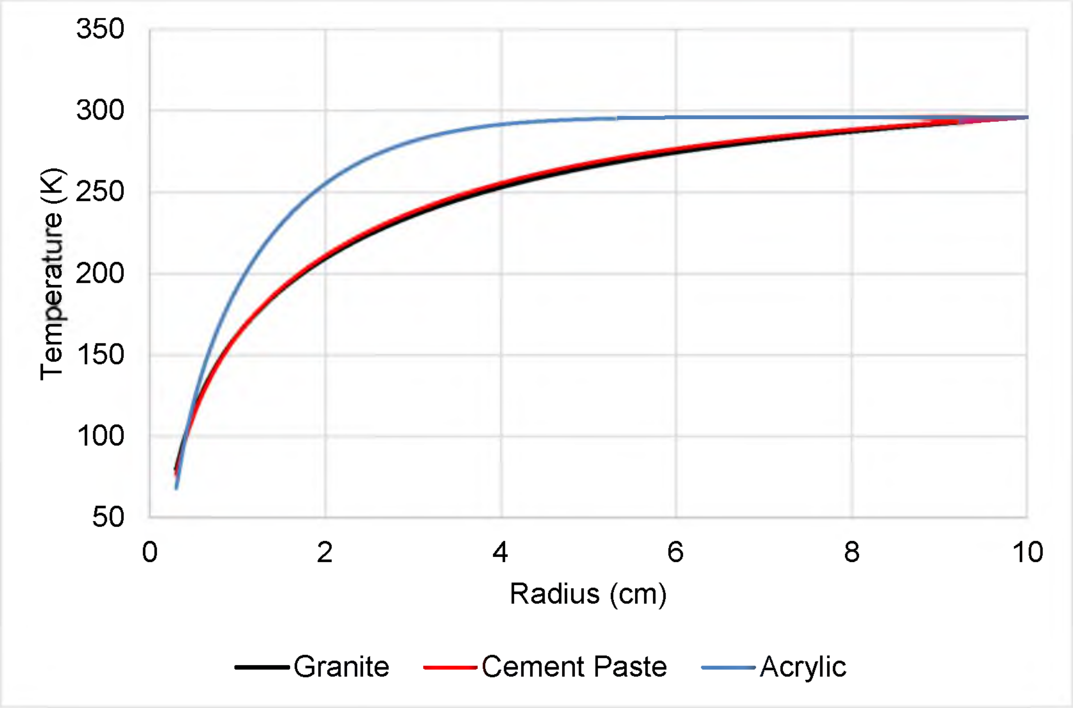

Figure 4.5: Temperature of specimens after exposure to liquid nitrogen for 30 minutes.

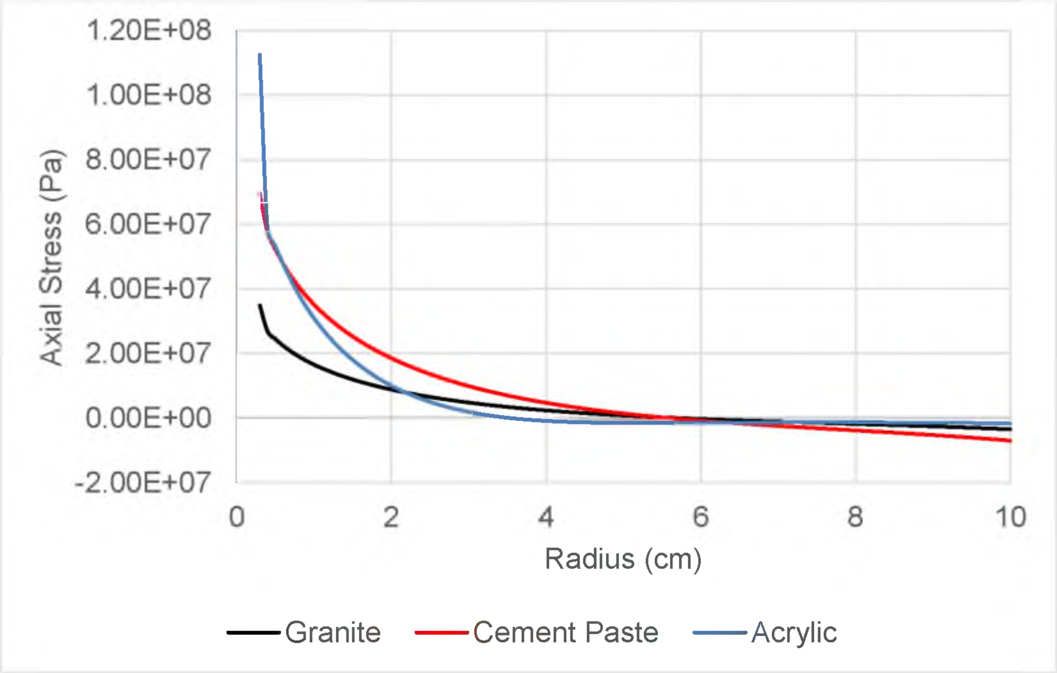

Figure 4.6 Axial stress of specimens after exposure to liquid nitrogen for 30 minutes.

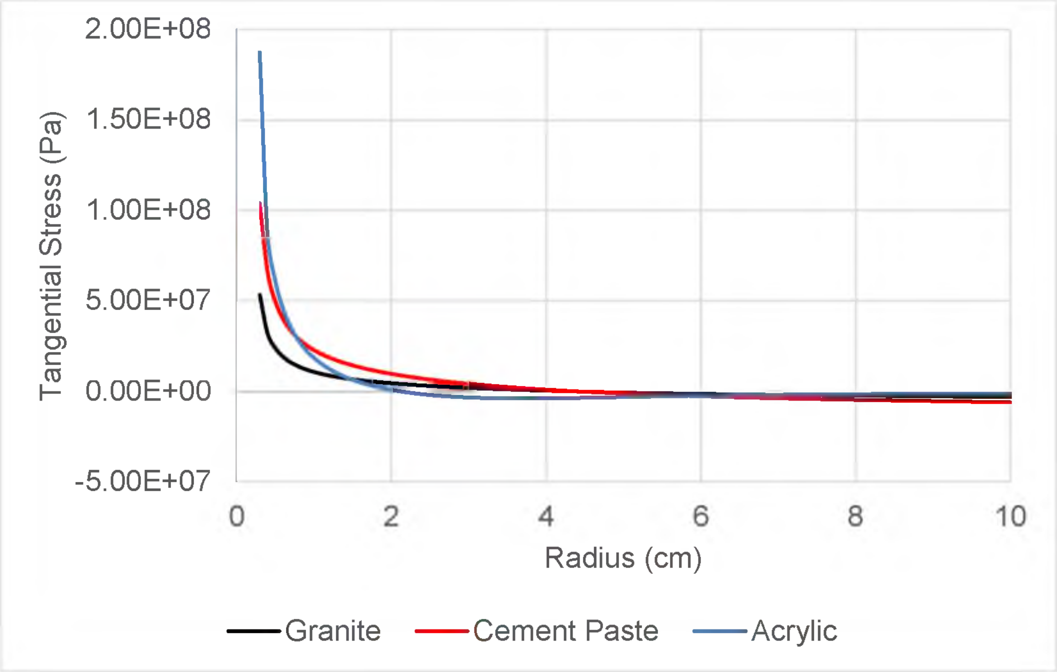

Figure 4.7 Tangential stress of specimens after exposure to liquid nitrogen for 30 minutes.

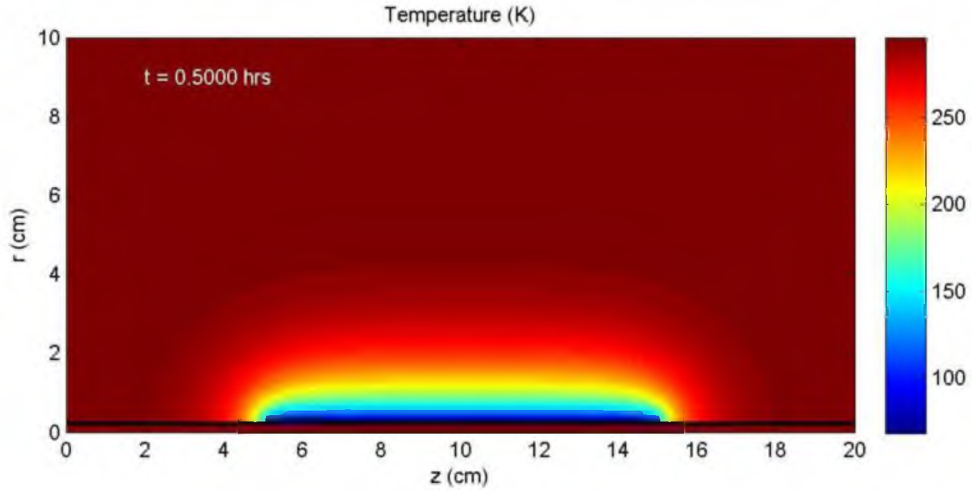

Figure 4.8: Temperature profile of acrylic after 30 minutes exposure to liquid nitrogen.

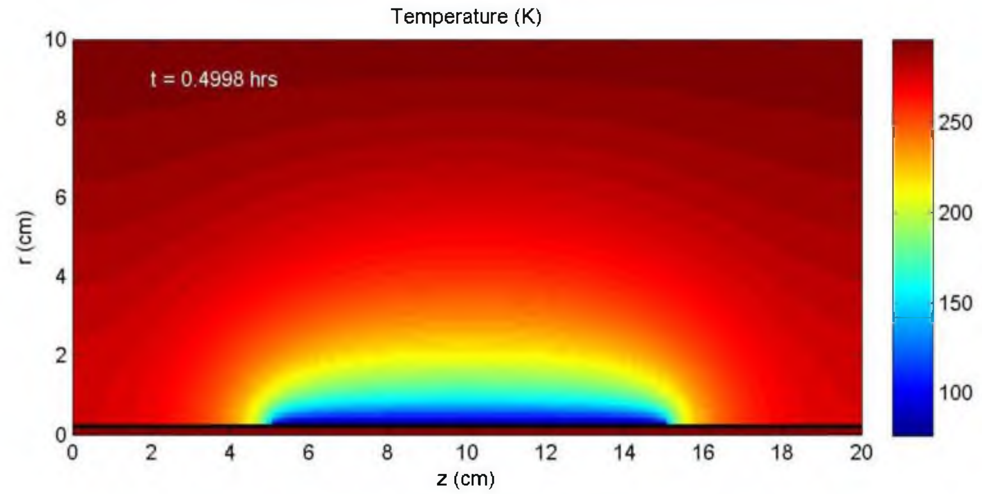

Figure 4.9: Temperature profile of cement paste after 30 minutes exposure to liquid nitrogen.

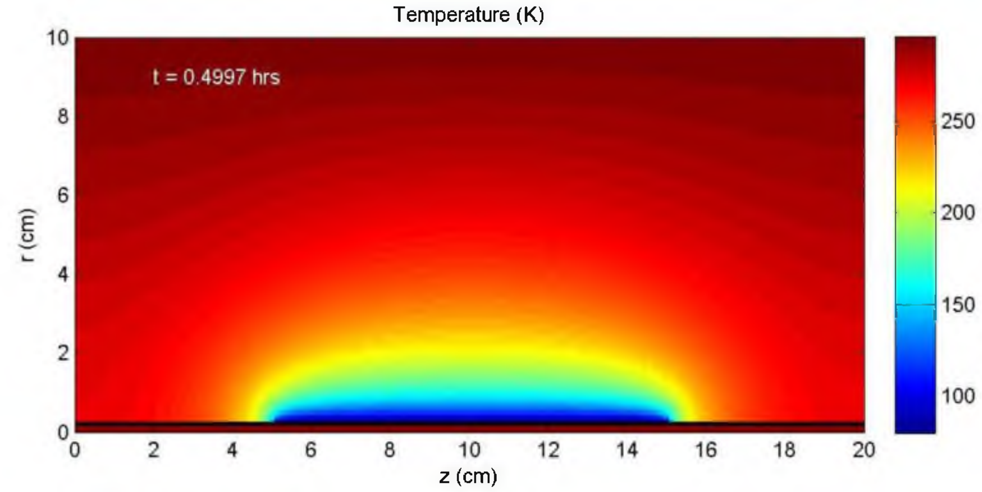

Figure 4.10: Temperature profile of granite after 30 minutes exposure to liquid nitrogen.

4.8 References

[1] Noda, N., Hetnarski, R.B., and Tanigawa, Y., 2003, *Thermal Stresses*, 2nd ed., Taylor & Francis, New York, pp. 260, Chap. 6.

[2] Daneshy, A.A., 1973, "A Study of Inclined Hydraulic Fractures," SPE 4062, SPE J., pp. 61-68.

[3] Tada, H, Paris, PC, and Irwin, GR, 2000, *The Stress Analysis of Crack Handbook*, 3rd ed., ASME Press, New York.

[4] Sih, GC, 1973, *Handbook of Stress-Intensity Factors for Researchers and Engineers*, Institute of Fracture and Solid Mechanics, Lehigh University, Bethlehem, Pennsylvania.

[5] Murakami, Y, Eds., et. al., 1987, *Stress Intensity Factors Handbook*, 2nd Vol., Pergamon Press, New York.

[6] Rooke, DP, and Cartwright, DJ, 1976, *Compendium of Stress Intensity Factors*, HMSO, London.

[7] Laham, SA, 1999, "Stress Intensity Factor and Limit Load Handbook," SINTAP/Task 2.6, British Energy Generation LTD.

[8] Bueckner, H.F., 1970, "A Novel Principle for the Computation of Stress Intensity Factors," Zeit. Ang. Math. Mech. (ZAMM), **50**(9), pp. 529-546.

[9] Cartwright, D.J., 1979, *Developments in Fracture Mechanics*, G.G. Chell Eds., Applied Science Publishers LTD, London, Chap 2.

[10] Lecampion, B., Abbas, S., and Prioul, R., 2013, "Competition between Transverse and Axial Hydraulic Fractures in Horizontal Wells," SPE 163848, SPE J., pp. 1-13.

[11] Bowman, DR, 1993, "An Experimental Evaluation of the Effect of Hole Fabrication/Treatment Techniques on Residual Strength and Fatigue Life of Polycarbonate Specimens with Holes," 93-27589, University of Dayton Research Institute, Dayton, OH.

CHAPTER 5

CONCLUSIONS

Proof of concept experiments were performed to evaluate the heat mining potential of a new and innovative way to operate an Enhanced Geothermal System. Temperature buildup and drawdown was used to find the heat transfer rate when it can be assumed constant with respect to length along the cylindrical hole axis. By injecting water into hot dry rock, allowing it to thermally equilibrate and then dropping the pressure, steam can be produced, leading to high heat transfer rates from the rock, 39.16 W. This process has a distinct advantage of only needing one well to function. It was found that the steam generation produces around 10 times higher heat rates than that of low Peclet number single phase constant flow, which would be found in the reservoir away from the preferential flow pathways. Single phase flow has heat transfer that is dominated either by the fluid convection or matrix conduction. The driving heat transfer mechanism is determined by the modified Peclet number. For modified Peclet numbers greater than 1 the thermal conductivity of the rock will drive the heat transfer. Thermal breakthrough will happen faster with carbon dioxide as the working fluid in an EGS than water. The mechanism that controls the heat transfer process during vaporization caused by depressurization will depend on the fracture void percent, in the case where permeability is ignored.

Fractures were created that have faces that are perpendicular to the maximum principal stress of the isentropic homogeneous bench top acrylic specimens. This result validates the concept that was first presented by Perkins and Gonzalez [1]. This was accomplished by hydraulically fracturing the acrylic specimens, then thermally fracturing them with liquid nitrogen for 30 minutes, all while under a uniaxial load of 1,000 psi.

The hydraulic fracture breakdown pressure was almost half in acrylic specimens when they were thermally fractured first. Fractures created in large bench-top experimental specimens can detected in a medical CT scanner when the proper contrasting agent is used. It was concluded that thermal fractures created significant permeability, but almost completely closed when the temperature was normalized. When thermally stimulating, the Kaiser effect can be used as an indicator of preexisting fractures or previous stress state, if acoustic event monitoring is in place.

A finite difference thermoelastic code with a linear elastic fracture mechanics application was created. It has the capability of applying various types of heat transfer and evaluating the thermal stresses and fracture nucleation potential. It was concluded that the circumferential fractures that were created experimentally in acrylic occurred from flaws that are at least four times larger in that orientation from drilling.

Temperature profiles of the cement paste, acrylic, and granite specimens were calculated after 30 minutes of liquid nitrogen exposure. These profiles revealed a well defined temperature cage in the acrylic specimens that produces the large thermal gradients driving the creation of the observed thermal fractures experimentally. This implies that a circumferential fracture could be achieved in a reservoir if the well was drilled horizontally in the direction of least principal stress and in-situ flaws were oriented in the direction perpendicular to the wellbore axis. In order to create thermal fractures in geologic reservoirs that are perpendicular to the maximum horizontal principal stress, half an order of magnitude larger flaws or preexisting fractures would have to exist in that orientation than features parallel to the maximum horizontal principal stress.

APPENDIX A

CEMENT PASTE SPECIMEN EXPERIMENTAL RESULTS

A.1 Specimen Casting

Cement paste specimens were cast with a 0.46 water to cement ratio. C10 and C11 had the plasticizer AdvaCast 575 added at 30 ml per 20 lbs. of cement along with the additive Vmar-3 at 20 ml per 20 lbs. of cement. Specimens C12 and C13 had Glenium 7710 added at 55 ml per 20 lbs. of cement and Vmar-3 at 10 ml per 20 lbs. cement. They were always kept in water or the 100% humidity room. Specimens C10 and C11 are 8 by 8 by 11.5 inches and C12 and C13 are 8 by 8 by 12 inches.

A.2 Cement Paste Specimen C10

Cement paste specimen C10 was hydraulically fractured then thermally fractured. The first attempt to hydraulically fracture C10 seemed successful. Water was injected at 1 ml/minute and dropped off sharply at 600.4 psi. There was no water observed leaking water from the packers at that time. The CT scan of C10 injected with 35% SSKI revealed no fractures.

The second attempt to hydraulically fracture C10 was successful. Water was injected at 5 ml/minute and breakdown pressure was recorded at 519 psi. CT scans revealed a fracture as seen in Figure A.1.

C10 was thermally fractured with liquid nitrogen 14 months after the second hydraulic fracture experiment took place. Liquid nitrogen was applied to the through hole for 30 minutes, whilst the block was under the 1,000 psi stress. The acoustic data from the experiment is in Figure A.2. The acoustic emissions show significant events that are the result of thermal fracturing. It was observed that after the liquid nitrogen was shut off the acoustic events dramatically reduced in frequency and magnitude (see Figure A.3). CT scanning of C10 after the thermal fracture experiment was conducted with 35% SSKI. No fractures were detected. I believe that the thermal fractures did not create an aperture large enough to be detected. I also believe that the hydraulic fractures infilled with mineral precipitation from the blocks sitting in water for 14 months.

A.3 Cement Paste Specimen C11

Cement paste specimen C11 was thermally fractured then hydraulically fractured. C11 was thermally experimented with liquid nitrogen running for 8 minutes. The subsequent CT scan did not detect any fractures. C11 was thermally fractured a second time, but for 30 minutes of liquid nitrogen exposure to the inner through hole. The acoustic events were recorded during the second experiment and are seen in Figure A.4. Despite the large frequency and magnitude of acoustic events, no fractures were detected when CT scanned with 35% SSKI.

C11 was hydraulically fractured with water after it was thermally fractured. It was pressurized by a constant flow rate of 5 ml/minute and fractured at a breakdown pressure of 571 psi. Acoustic events accompanied the pressure increase as seen in Figure A.5. A hydraulic fracture was also observed in the CT scans, seen in Figure A.6.

A.4 Cement Paste Specimen C12

Cement paste specimen C12 was hydraulically fractured then thermally fractured. C12 was hydraulically fracture at a constant flow rate of 5 ml/minute with a breakdown pressure of 622.4 psi (See Figure A.7). Figure A.8 shows the subsequent CT scan and hydraulic fracture.

C12 was thermally fractured for 30 minutes after it was hydraulically fractured and CT scanned after that with 35% SSKI. No fractures were detected. I think this is due to the thermal fractures being having too small of an aperture to detect and the hydraulic fractures being infilled during the 14 months in between experiments and the blocks sitting in water. Acoustic events were recorded during the experiment and after (see Figures A.9 and A.10).

A.5 Cement Paste Specimen C13

Cement paste specimen C13 was thermally fractured only. C13 was thermally experimented for 8 minutes after which it was CT scanned with 35% SSKI with no fractures detected. C13 was thermally fractured again for 30 minutes and the thermal fracture extended to 4 sides of the block. The acoustic events are shown in Figure A.11 during and Figure A.12 for after the experiment. The CT scans, seen in Figure A.13, revealed significant fracturing. C13 was not hydraulically fractured due to the extensiveness of the thermal fractures.

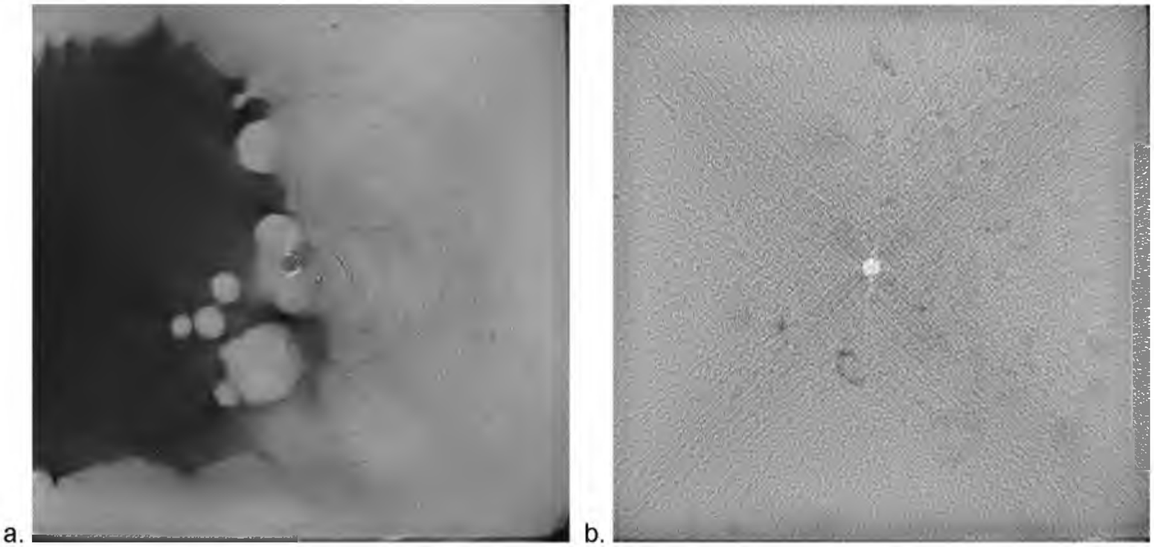

Figure A.1: CT scan of C10 after the second hydraulic fracture experiment with 35% SSKI injected. The fracture can be clearly seen with the naked eye when viewing the scans as a video, but they are very hard to make out as individual photographs. These are the two best in the specimen. The fracture which extends both above and below the hole starts at side A and continues to at least 9.39 inches from side A. a. Fracture at side A, b. Fracture 1.22 inches from side A.

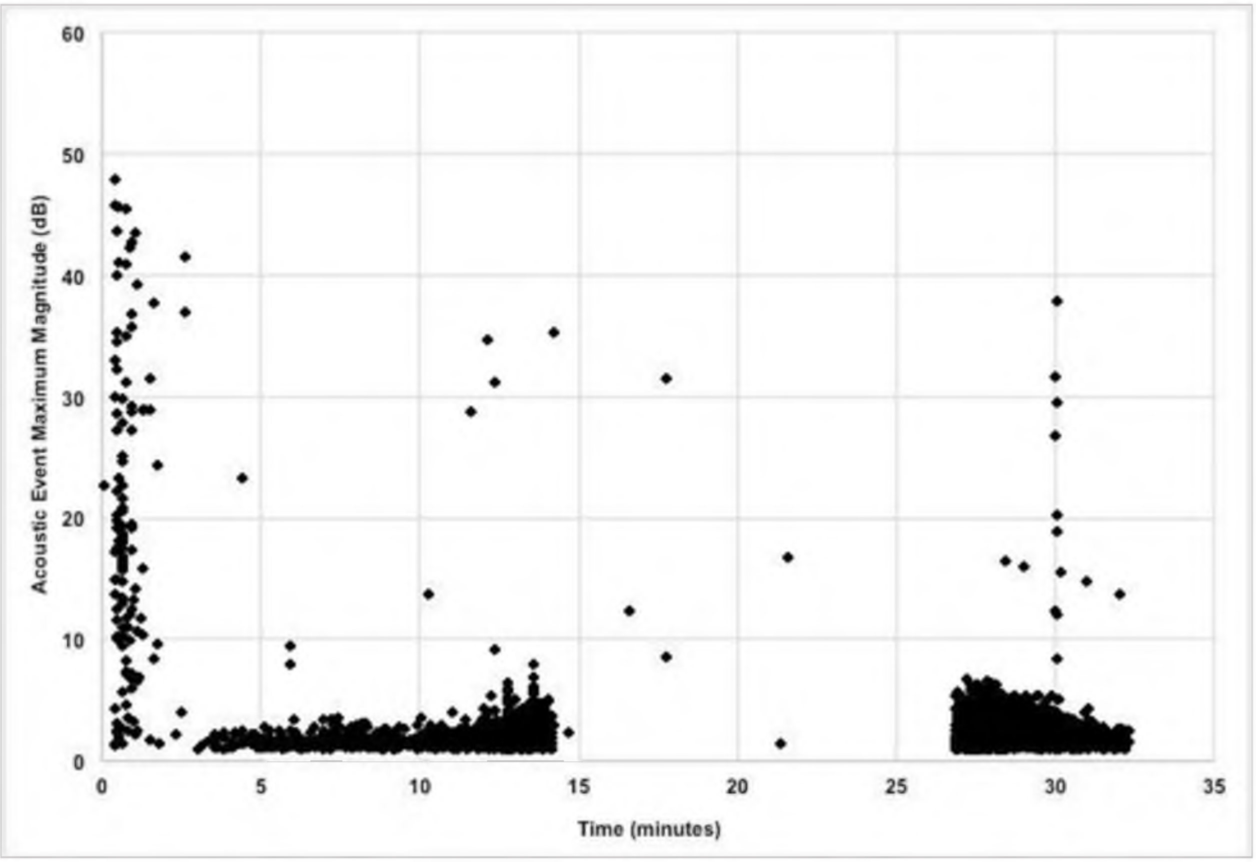

Figure A.2: Peak of all acoustic events over the threshold of 1 dB with a reference voltage of 0.5 mV during the thermal fracture experiment of C10. 3644 events recorded with the maximum being 47.89 dB.

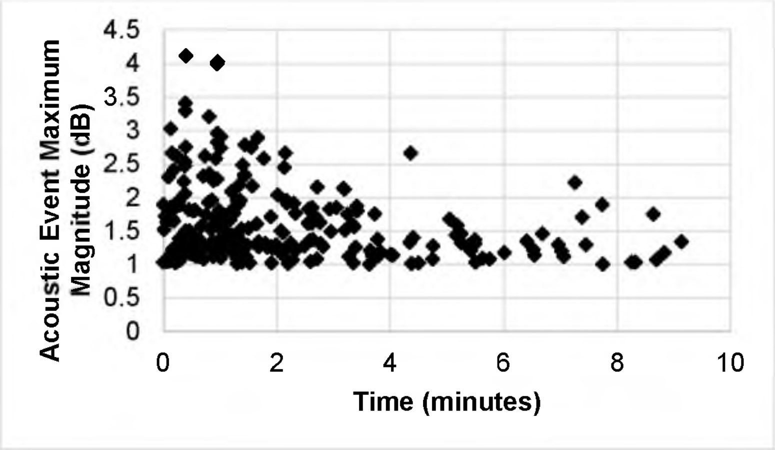

Figure A.3: Peak of all acoustic events over the threshold of 1 dB with a reference voltage of 0.5 mV after the thermal fracture experiment of C10. 228 events recorded with the maximum being 4.12 dB.

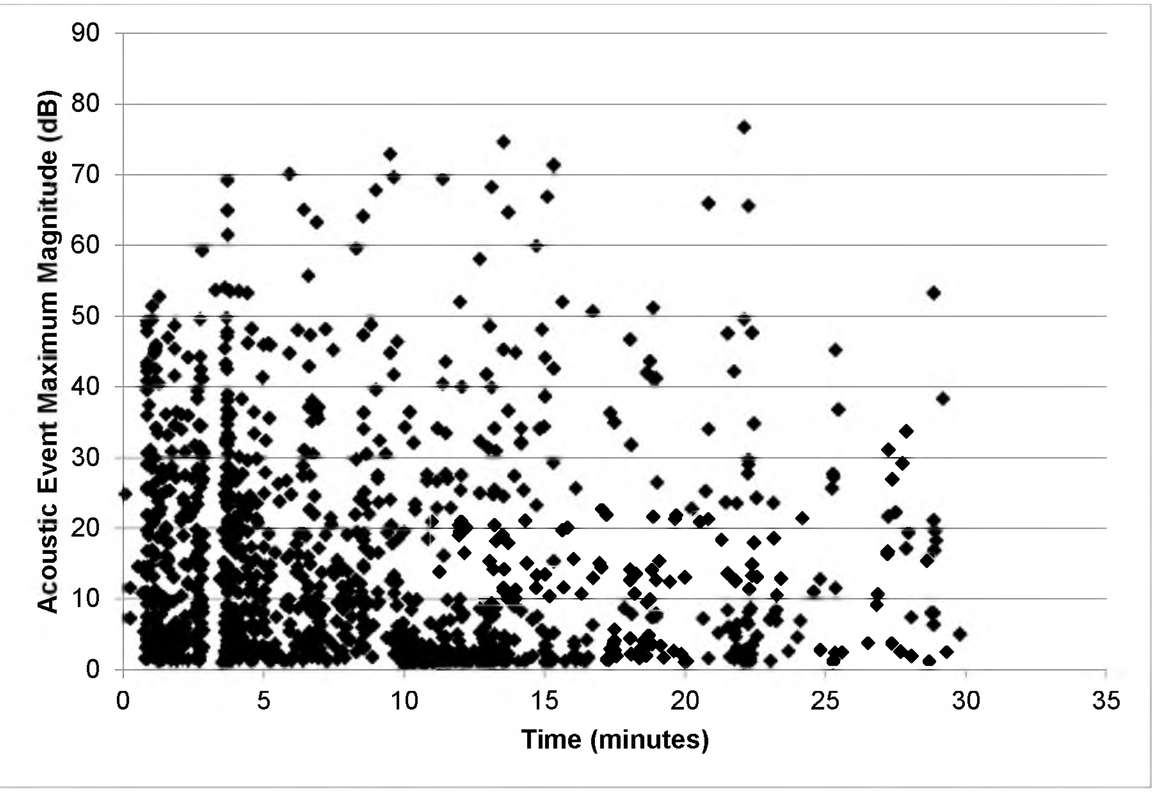

Figure A.4: Peak of all acoustic events over the threshold of 1 dB with a reference voltage of 0.35 mV during the thermal fracture experiment of C11. 1634 events recorded with the maximum being 76.73 dB.

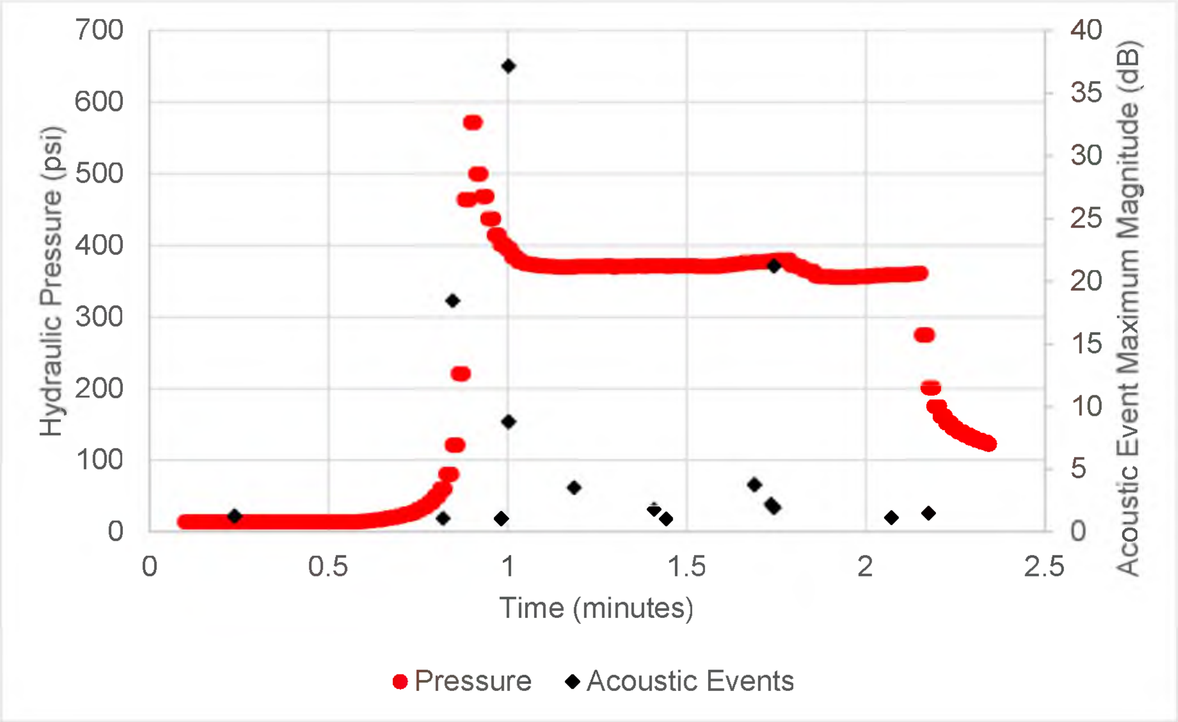

Figure A.5: Hydraulic pressure and acoustic events during the hydraulic fracture experiment of C11 post thermal fracturing. Peak of all acoustic events over the threshold of 1 dB with a reference voltage of 0.675 mV. 16 events recorded with the maximum being 37.17 dB. The time for the AE was adjusted by -0.15 minute, in order for it to line up with the pressure data. This is necessary because they were recorded on two separate computers and started at different times.

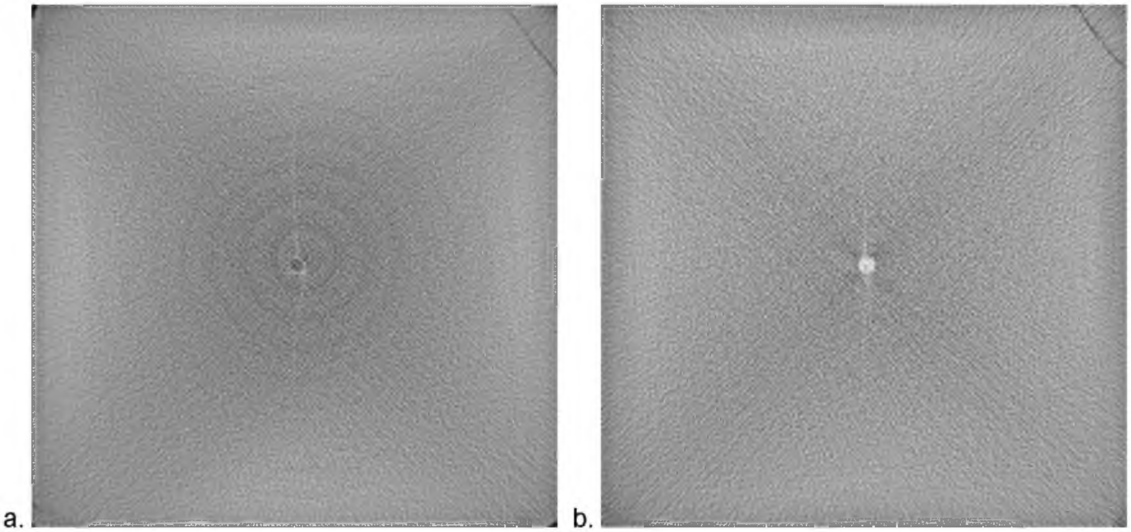

Figure A.6: CT scan of C11 post thermal and hydraulic fracture experiments with 35% SSKI injected. The fracture which extends both above and below the hole starts at side A and continues 2.05 inches where it shrinks and stops. It is detected again at 9.61 where it grows all the way to side B. a. Fracture 0.21 inch from side A, b. Fracture 0.84 inch from side A.

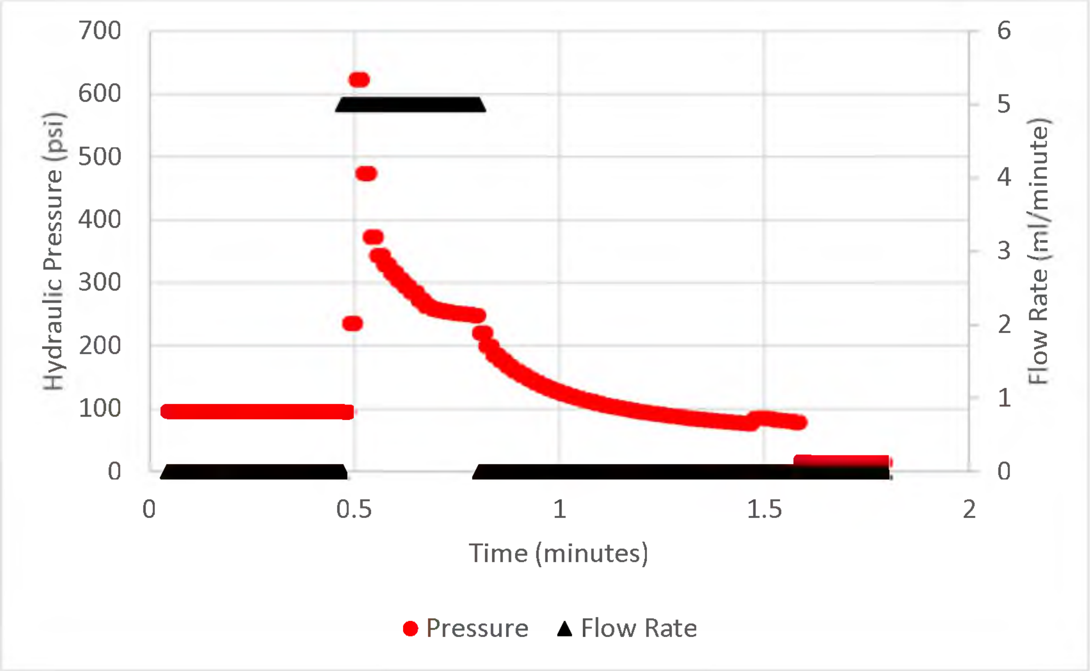

Figure A.7: Hydraulic pressure and flow rate of C12 hydraulic fracture experiment. Breakdown pressure reached 622.4 psi.

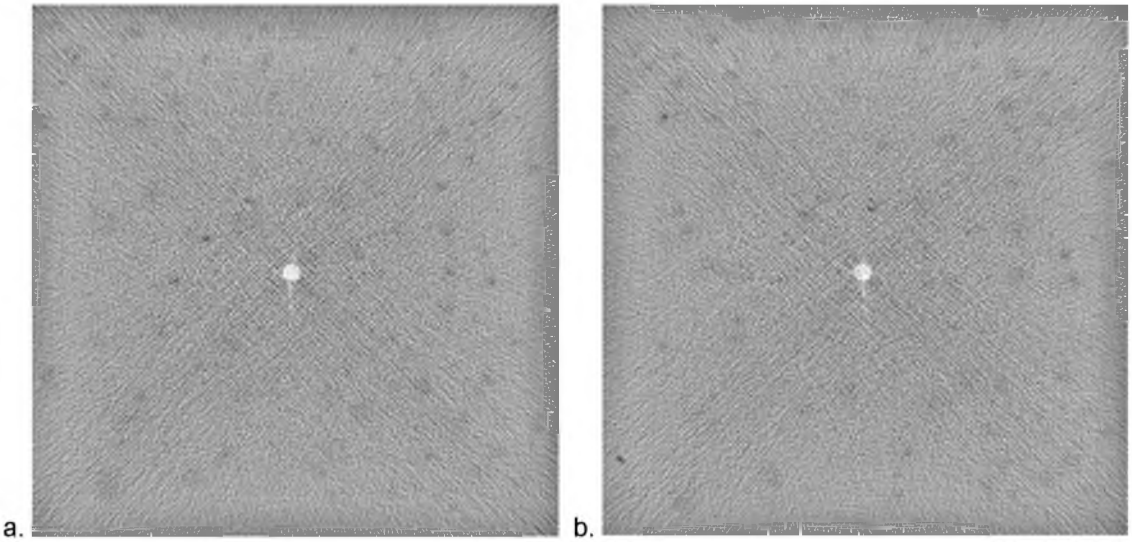

Figure A.8: CT scan of C12 post hydraulic fracture experiment with 35% SSKI injected. The fracture can be clearly seen with the naked eye when viewing the scans as a video, but they are very hard to make out as individual photographs. These are the two best in the specimen. The fracture which extends both above and below the hole starts 3.49 inches from side A and continues to at least 6.14 inches from side A. a. Fracture 4.85 inches from side A, b. Fracture 5.57 inches from side A.

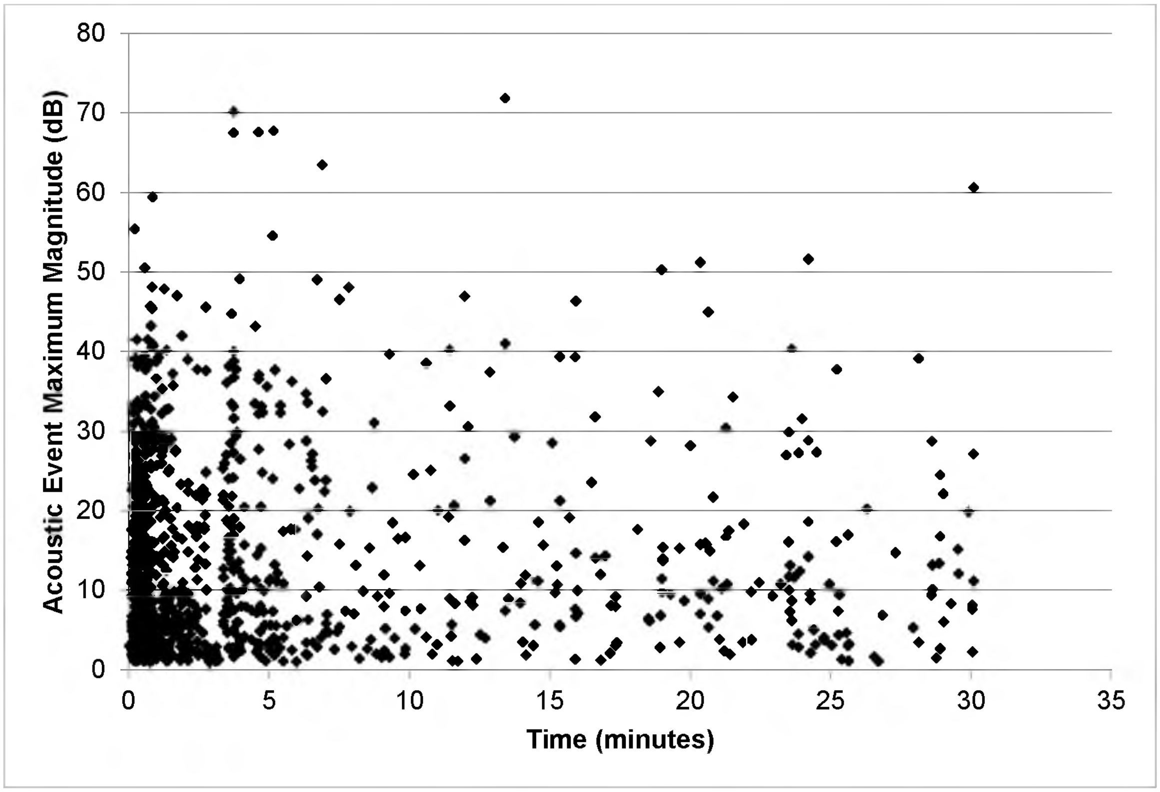

Figure A.9: Peak of all acoustic events over the threshold of 1 dB with a reference voltage of 0.35 mV during the thermal fracture experiment of C12. 1085 events recorded with the maximum being 71.84 dB.

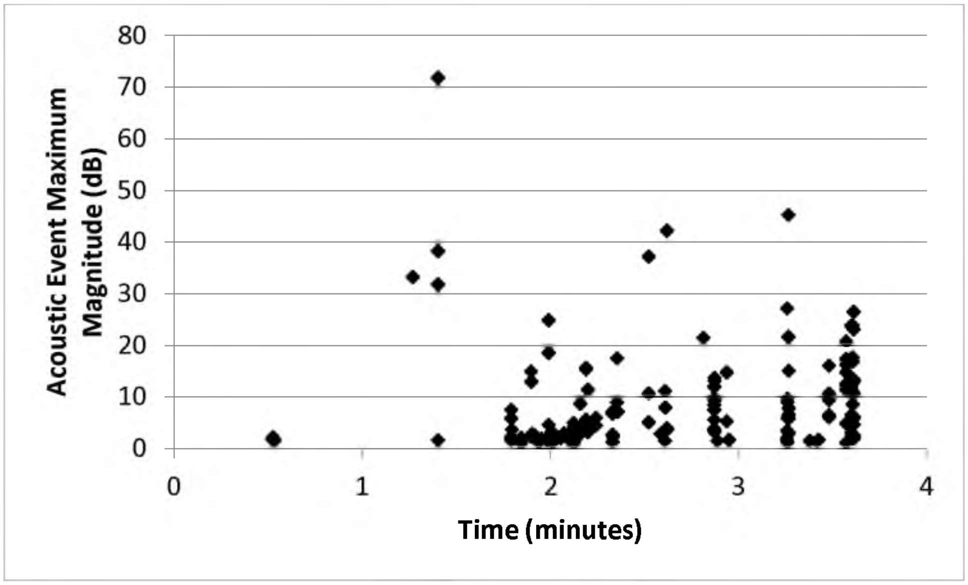

Figure A.10: Peak of all acoustic events over the threshold of 1 dB with a reference voltage of 0.35 mV after the thermal fracture experiment of C12. 156 events recorded with the maximum being 71.76 dB.

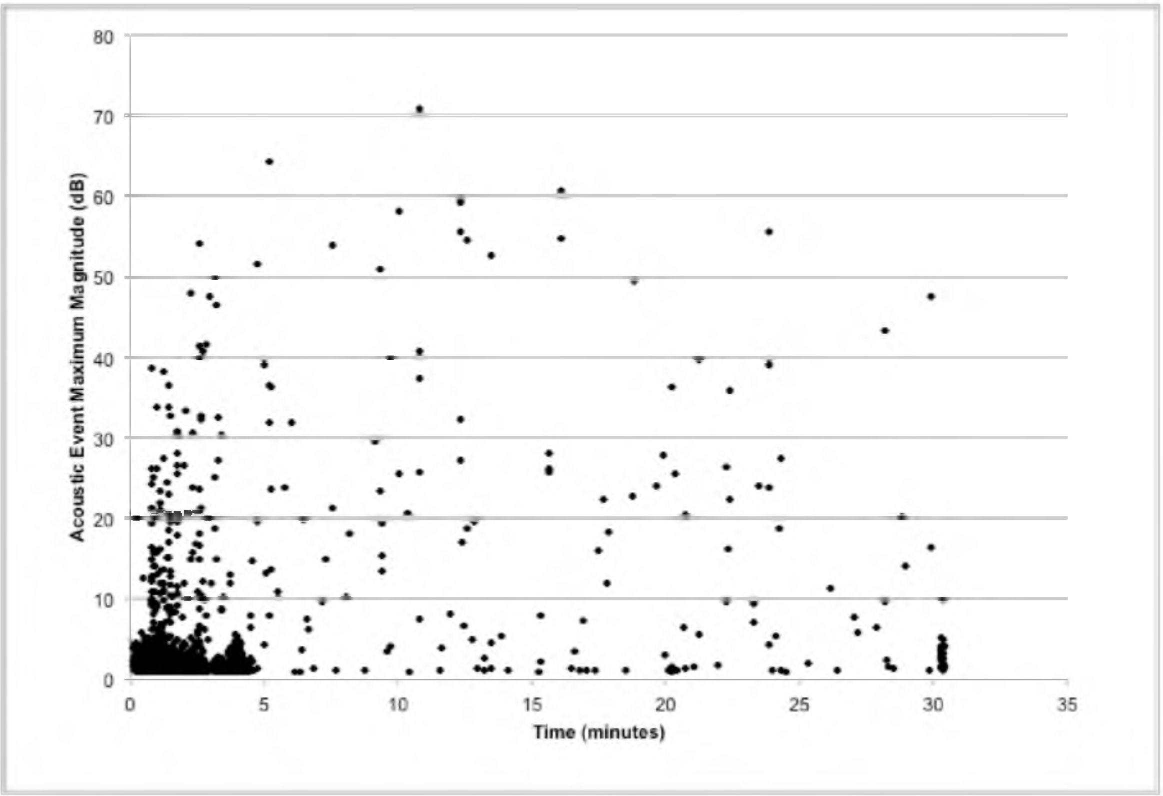

Figure A.11: Peak of all acoustic events over the threshold of 1 dB with a reference voltage of 0.275 mV during the thermal fracture experiment of C13. 3683 events recorded with the maximum being 70.87 dB.

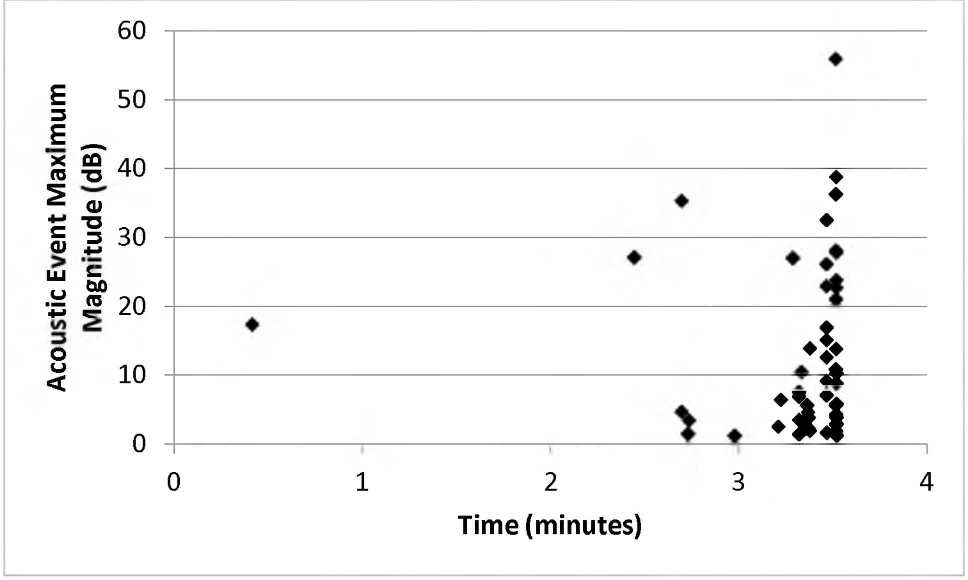

Figure A.12: Peak of all acoustic events over the threshold of 1 dB with a reference voltage of 0.275 mV after the thermal fracture experiment of C13. 53 events recorded with the maximum being 55.91 dB.

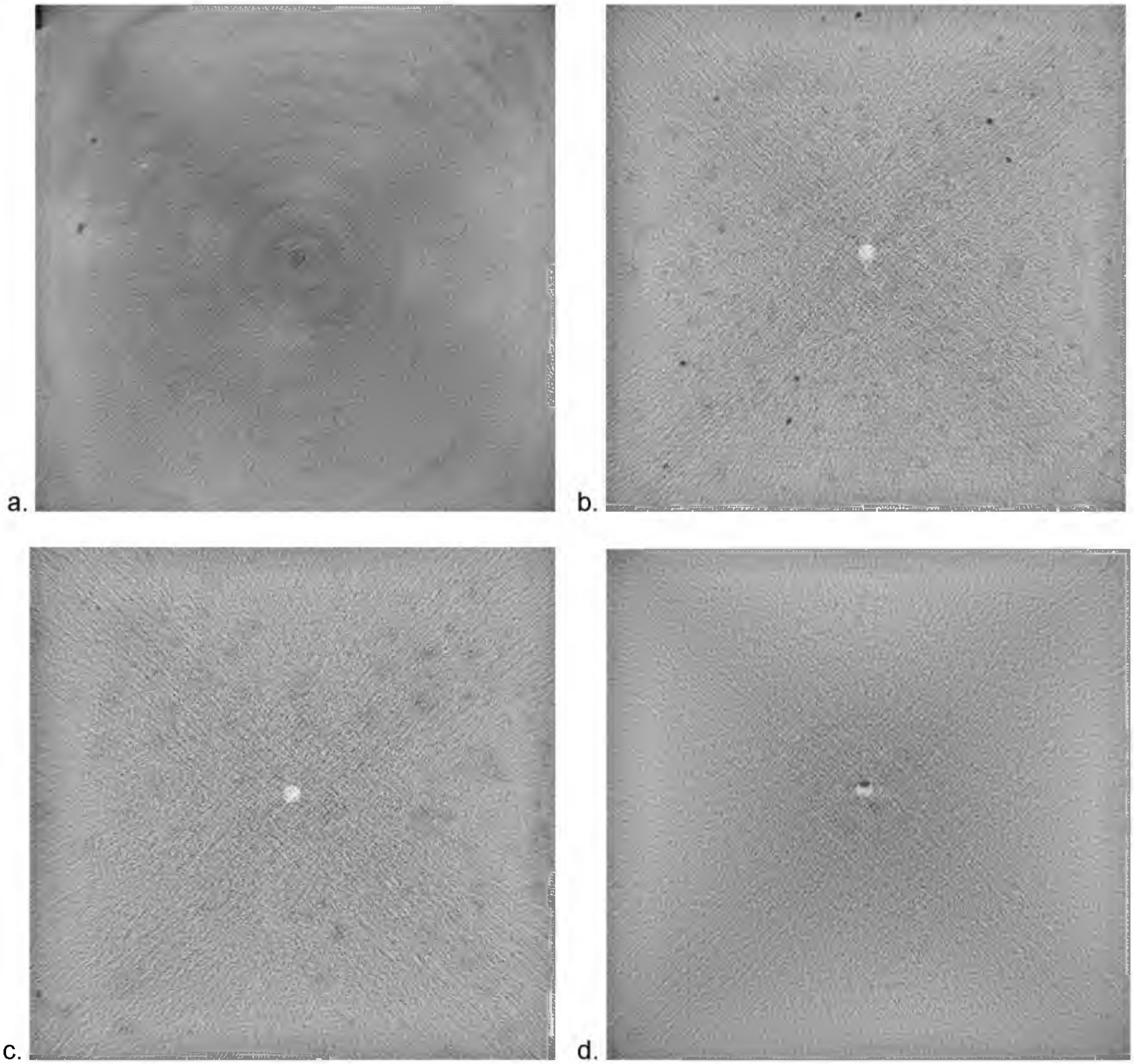

Figure A.13: CT scan of C13 post thermal fracture experiment with 35% SSKI injected. The fracture which extends both above and below the hole starts at side A and continues to side B. At side A the fractures is tilted 14° to the right and this continues for 9.5 inches where it becomes within 2° of vertical and stays that way to side B. a, b, c, and d are 0.11 inch, 1.89 inches, 6.0 inches, and 11.18 inches from side A respectively.

APPENDIX B

GRANITE SPECIMEN EXPERIMENTAL RESULTS

All granite specimens were CT scanned before any experimentation and after their first experiment with 35% SSKI injected. None of these scans detected fractures, because of the lack of CT contrast between the dense granite and not dense enough 35% SSKI. The granite blocks were all CT scanned with Indium Casting Metal Injected into them. G1, G2, and G4 revealed fractures from this process and are in the Figures B.4, B.8, and B.17.

B.1 Granite Specimen G1

Granite specimen G1 was hydraulically fractured then thermally fractured. G1 was hydraulically fractured at 5 ml/minute and had a breakdown pressure of 2201.4 psi (see Figure B.1). The fracture cracked through the block to side B.

G1 was thermally fractured with liquid nitrogen for 30 minutes. The acoustic events during and after the experiment are shown in Figures B.2 and B.3.

G1 was heated to 85°C in an oven and injected with Indium Casting Alloy, then CT scanned at 140 KeV and 1100 mas so the fracture geometry could be determined. As seen in Figure B.4 a and b the fracture exited out of Side B. The fracture remains within 2° of vertical and entirely above the hole until 1.42 inches from side B. From 1.42 inches until 4.58 inches it extends both above and below the hole. The wing above extends to a maximum of 3.25 inches and as it ends it slants to the right 17° from vertical. This is observed in Figure B.4 c and d. The bottom wing is clearly seen with the naked eye looking at a movie of the slides at 20 fps. It extends to 1.9 inches and stays near vertical.

B.2 Granite Specimen G2

Granite specimen G2 was hydraulically fractured then thermally fractured. G2 was initially pressurized at a flow rate of 20 ml/minute accidentely during the preparation phase of thehydraulic fracture experiment. The pressure reached at least 1500 psi during the 10 seconds of the accident. No data was being recorded when this occurred.

In an attempt to have a more controlled hydraulic fracture the pressure was started low and raised periodically. The flow rate, shown in blue in Figure B.5, starts at 0.5 ml/minute, then 1 ml/minute after the first minute, and finally after nine minutes is raised to 5 ml/minute. The pressure in Figure B.5 is a result of the changing flow rates, along with the high pressure valve other side of the specimen from the pump was slightly open. The valve was closed at 3 minutes. The low breakdown pressure of the hydraulic fracture created at 9 minutes is most likely due to the pre-experiment pressurization accident.

It was attempted to hydraulically fracture G2 two more times. Both times there were negligible acoustic events and the pressure plateaued, without the distinctive drop off of hydraulic fractures. The flow rates and plateaued pressures are 5 ml/minute, 700 psi and 10 ml/minute, 750 psi.

G2 was thermally fractured with liquid nitrogen for 30 minutes. The acoustic events during and after the experiment are shown in Figures B.6 and B.7.

G2 was heated to 85°C in an oven and injected with Indium Casting Alloy, then CT scanned at 140 KeV and 1100 mas so the fracture geometry could be determined. Figure B.8 a and b show the surface manifestation of the fracture. At surface B the fracture is 1.43 inches long at 6° tilted right from vertical and offset 0.63 inches to the left from the center hole. The fracture extends to a depth of 8.2 inches from side B. At 1.6 inches the fracture extends a second wing going near vertical above the hole. The bottom wing grows to a length of 3.33 inches and shortens dramatically when it ends. Figure B.8 c and d illustrate the bottom wind growing and becoming near vertical at 3.6 inches and remaining so until it ends. The top wing has a maximum length of 2.2 inches from the center of the hole and remains near vertical until 4 inches then tilts to the right ending at 21° from vertical.

B.3 Granite Specimen G3

Granite specimen G3 was thermally fractured then hydraulically fractured. G3 was thermally fractured with liquid nitrogen for 30 minutes. The acoustic events during and after the experiment are shown in Figures B.9 and B.10.

G3 was hydraulically fractured after it was thermally fractured. The breakdown pressure and flow rate was 1286 psi and 1 ml/minute, respectively (see Figure B.11). It was attempted to hydraulically fracture G3 two additional times. The second hydraulic fracture pressure and flow rate data indicate fracture extension (see Figure B.12). The third hydraulic fracture experiment does not indicate any additional fracturing (see Figure B.13). The acoustic data for all three hydraulic fracturing experiments is very low and inconclusive. No fractures were detected from the CT scan of G3 with indium casting alloy injected.

B.4 Granite Specimen G4

Granite specimen G4 was thermally fracture then hydraulically fractured. G4 was thermally fractured with liquid nitrogen for 30 minutes. The acoustic events during and after the experiment are shown in Figures B.14 and B.15.

G4 was hydraulically fractured after it was thermally fractured. The results from that experiment are shown in Figure B.16. The first steep decline occurred from the pressure reaching the safety pressure and the pump automatically changing the flow rate to zero. The safety pressure was increased and the experiment continued with a flow rate of 1 ml/minute. The breakdown pressure reached a peak at 2248.4 psi. The acoustic readings from this experiment are inconclusive.

It was attempted to hydraulically fracture G4 three additional times. These all resulted with no apparent fracture event from either the pressure or acoustic data.

G4 was heated to 85°C in an oven and injected with Indium Casting Alloy, then CT scanned at 140 KeV and 1100 mas so the fracture geometry could be determined. The fracture is 2 inches long and tilting 10° from vertical to the left at side B as seen in Figure B.17 a-d. At 0.3 inches from side B a second wing of the fracture grows above the hole. It is near vertical and has a uniform length of 1.25 inches. The bottom wing shifts to near vertical at 2.54 inches and both fractures remain vertical until they abruptly end at a depth of 4.77 inches from side B.

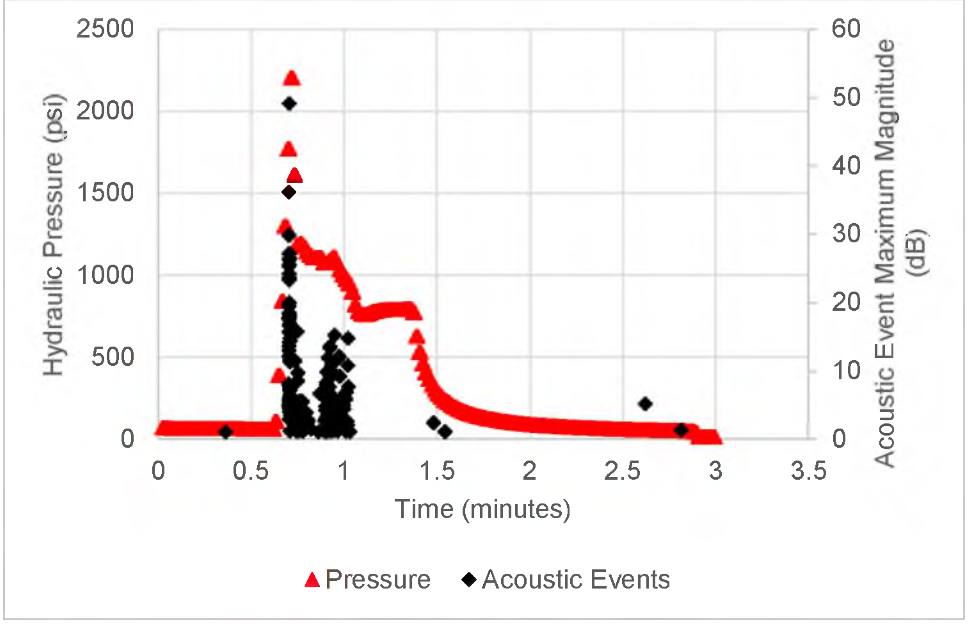

Figure B.1: Pressure and acoustic events during the hydraulic fracture experiment of G1. Peak of all acoustic events over the threshold of 1 dB with a reference voltage of 0.63 mV during the hydraulic fracture of G1. 179 events recorded with the maximum being 49.10 dB. The time for acoustic events was adjusted by -0.09 minute, in order for the data to line up. The breakdown pressure was 2201.4 psi.

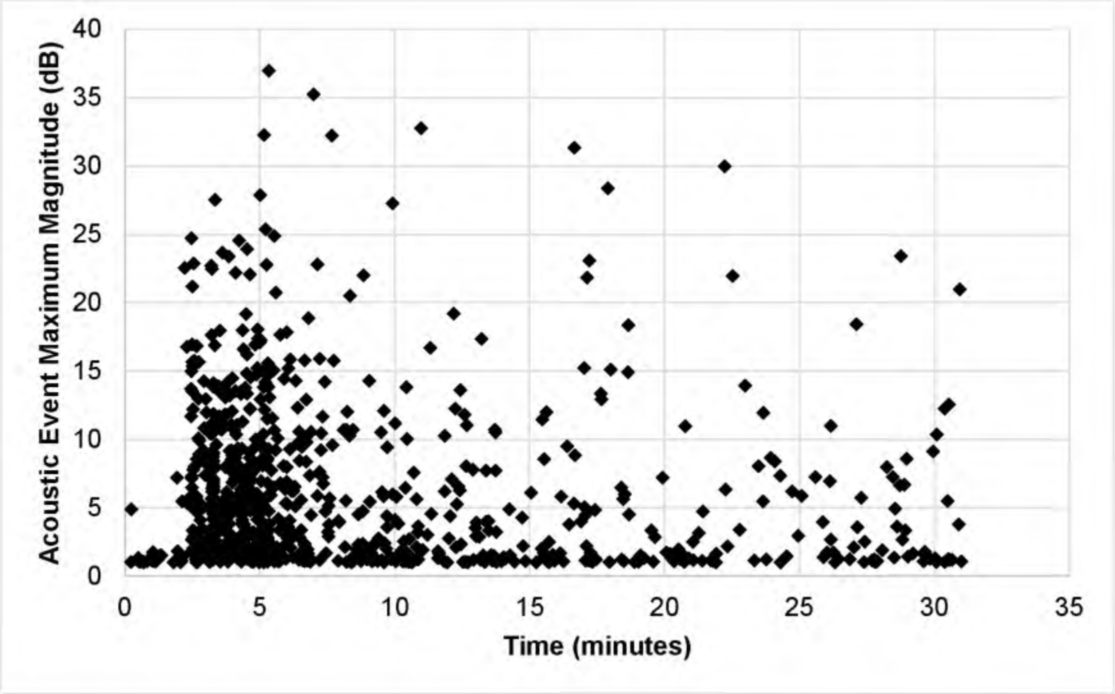

Figure B.2: Peak of all acoustic events over the threshold of 1 dB with a reference voltage of 0.3 mV during the thermal fracture of G1. 884 events were recorded with the maximum being 36.95 dB.

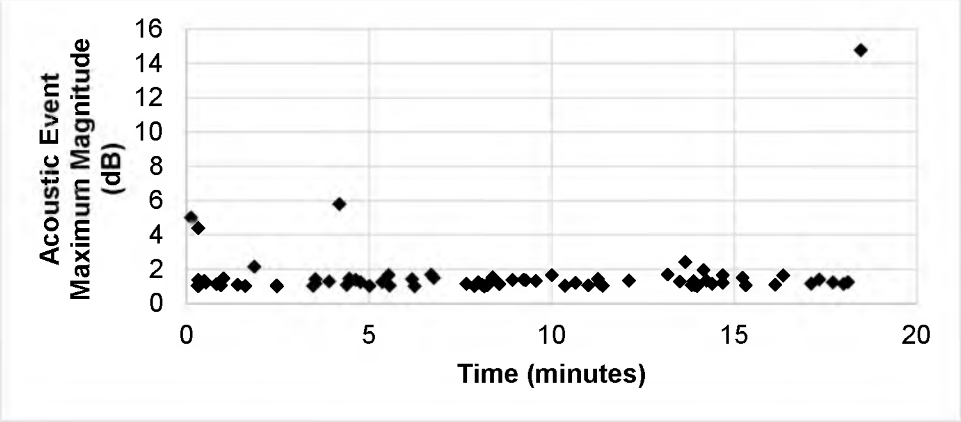

Figure B.3: Peak of all acoustic events over the threshold of 1 dB with a reference voltage of 0.3 mV after the thermal fracture of G1. 76 events were recorded with the maximum being 14.75 dB.

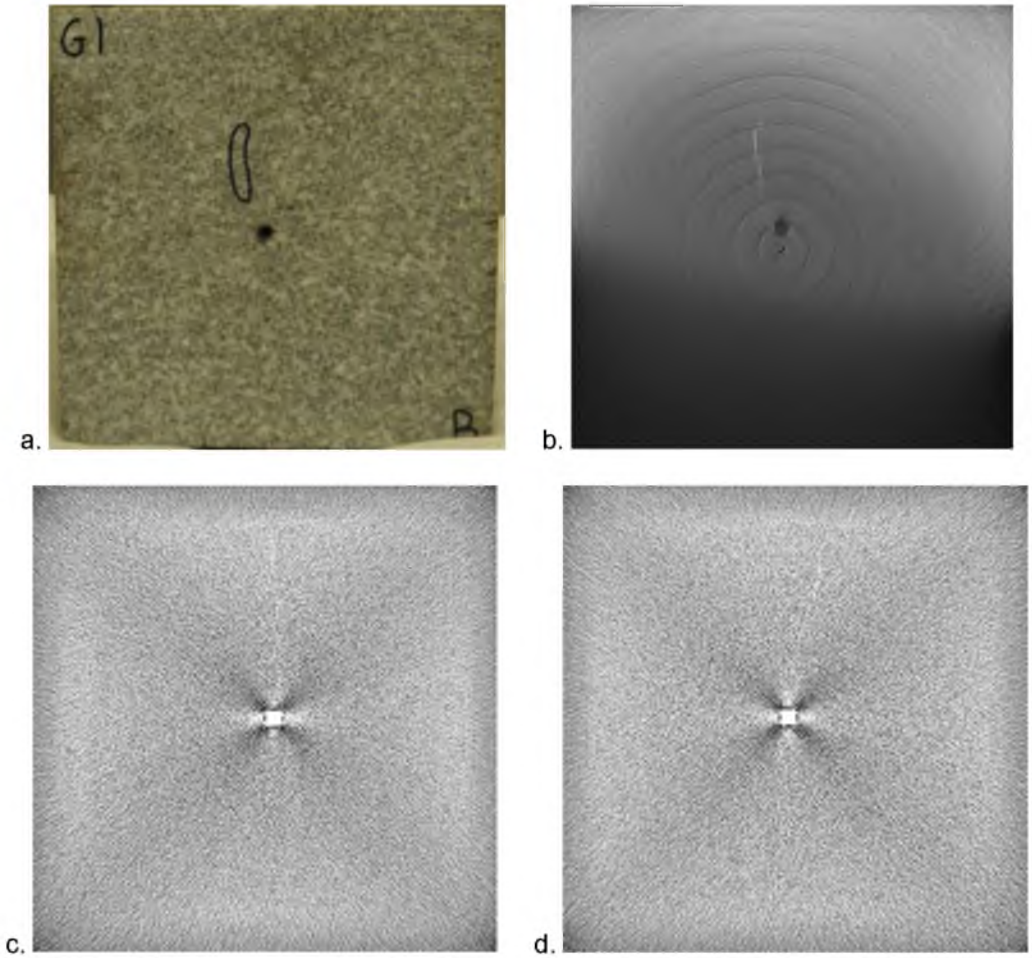

Figure B.4: Photograph and corresponding CT scans of specimen G1 injected with Indium casting alloy, after being hydraulically and thermally fractured. a) Photo of Side B with fracture encircled in black that was detected when liquid exited. b) CT scan of side B, c) CT scan 2.02 inches from side B, and d) CT scan 4.07 inches from side B.

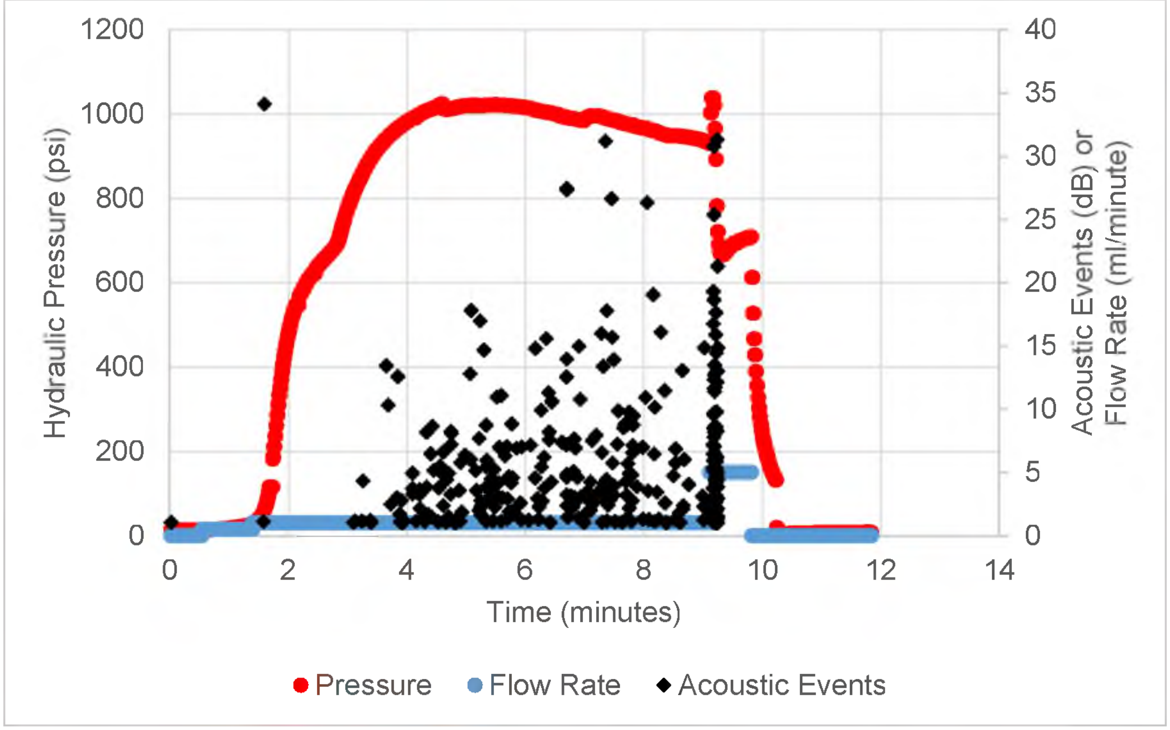

Figure B.5: Pressure, flow rate and acoustic events of the hydraulic fracture experiment of G2. Peak of all acoustic events over the threshold of 1 dB with a reference voltage of 0.63 mV during the first hydraulic fracture experiment of G2. 391 events were recorded with the maximum being 34.13 dB.

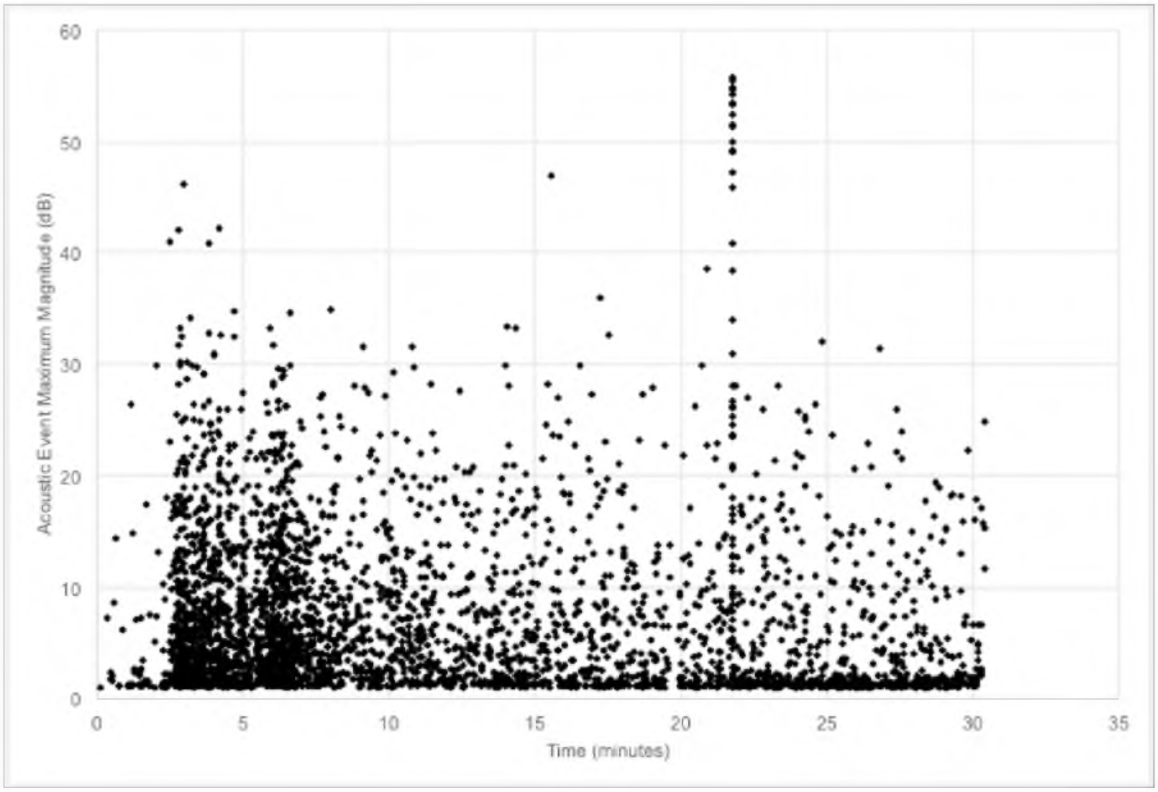

Figure B.6: Peak of all acoustic events over the threshold of 1 dB with a reference voltage of 0.3 mV during the thermal fracture experiment of G2. 3408 events were recorded with the maximum being 55.73 dB.

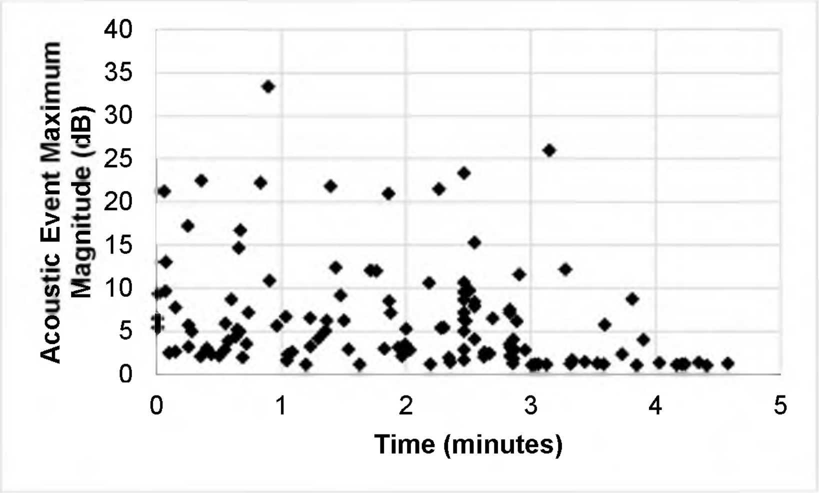

Figure B.7: Peak of all acoustic events over the threshold of 1 dB with a reference voltage of 0.3 mV after the thermal fracture experiment of G2. 125 events were recorded with the maximum being 33.38 dB.

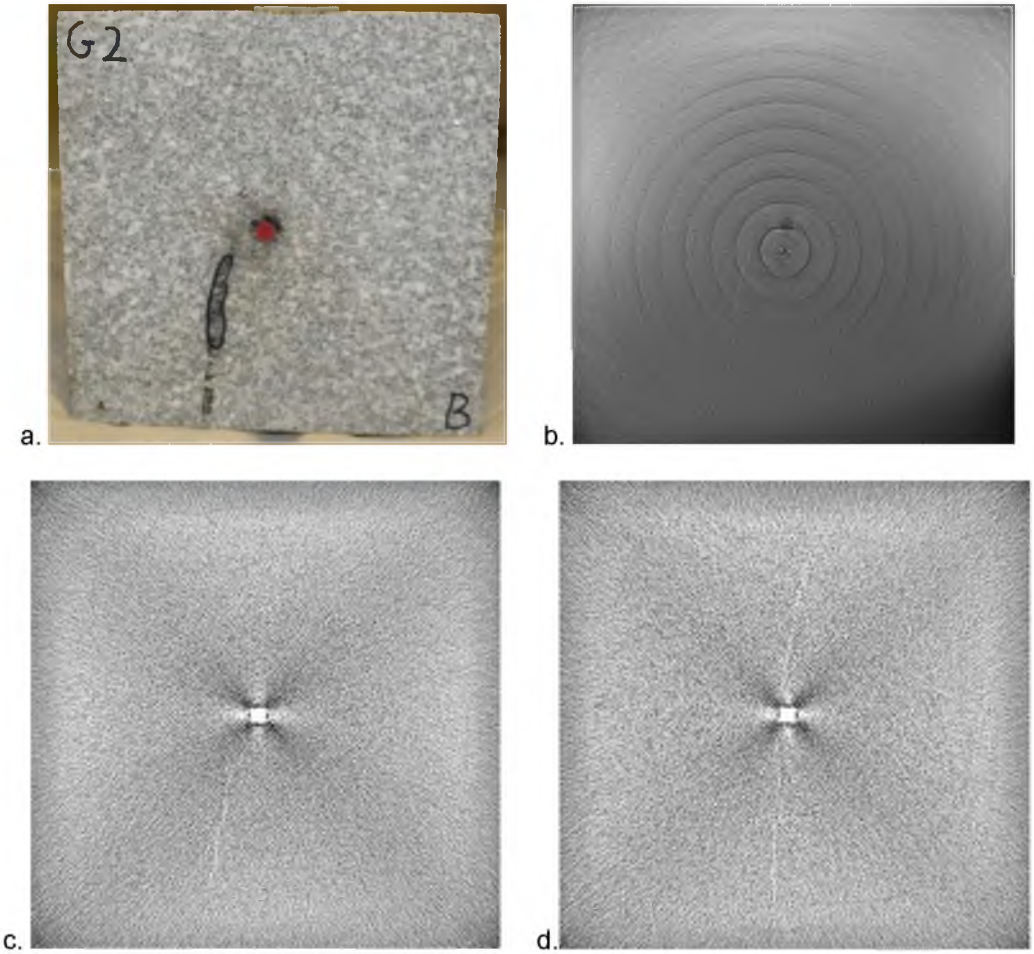

Figure B.8: Photograph and corresponding CT scans of specimen G2 injected with Indium Casting Alloy, after being hydraulically and thermally fractured. a) Photo of side B with fracture encircled in black that was detected when liquid exited. b) CT scan of side B, c) CT scan 1.52 inches from side B, and d) CT scan 4.4 inches from side B.

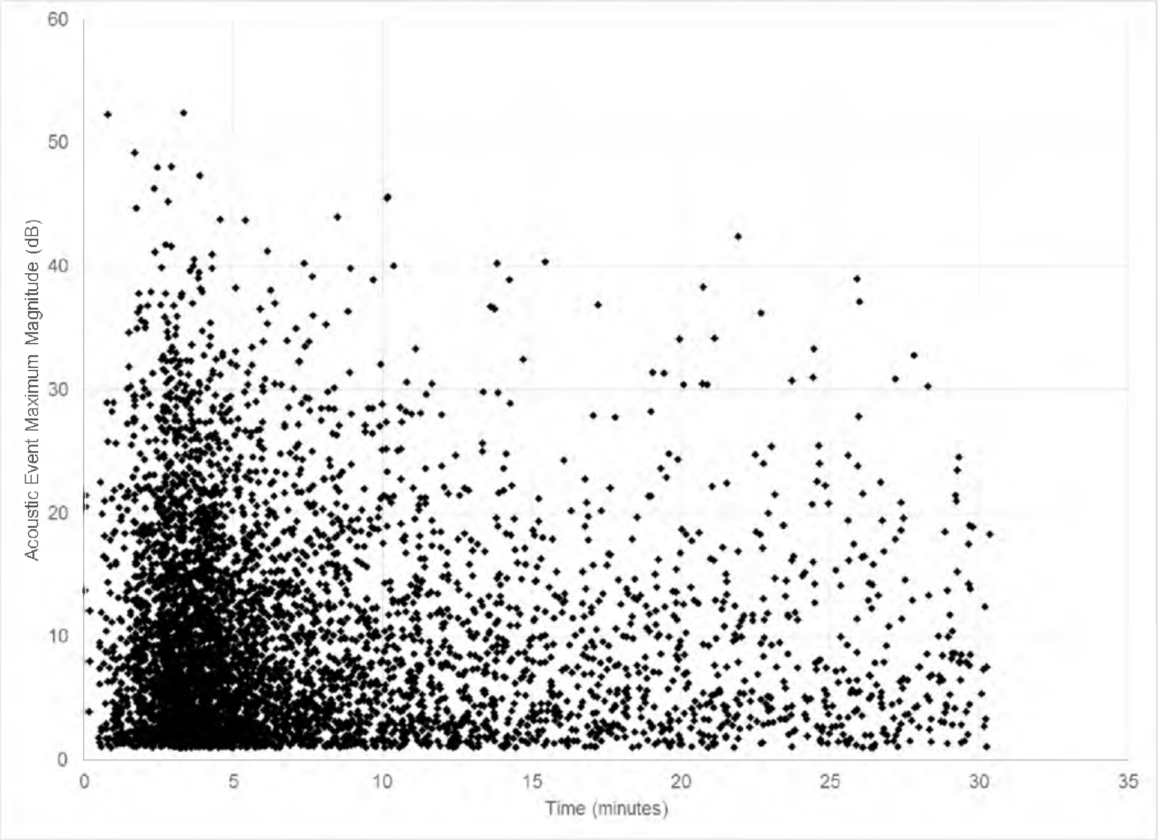

Figure B.9: Peak of all acoustic events over the threshold of 1 dB with a reference voltage of 0.35 mV during the Thermal Fracture of G3. 4859 recorded events with the maximum being 52.45 db.

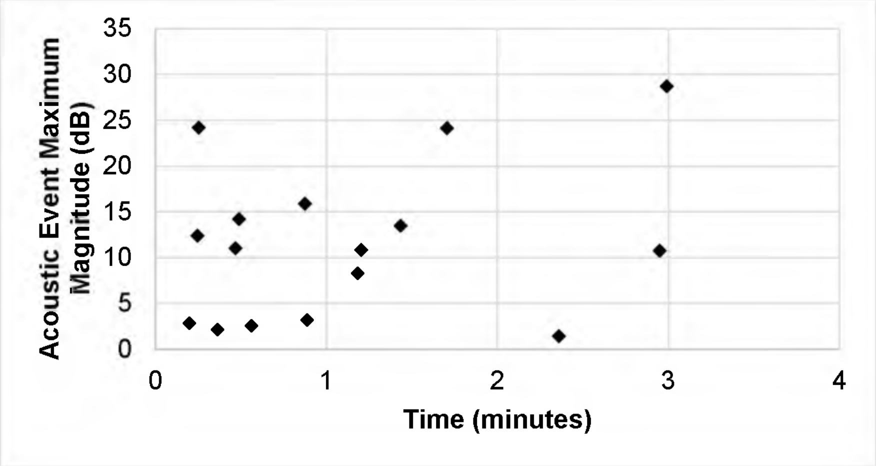

Figure B.10: Peak of all acoustic events over the threshold of 1 dB with a reference voltage of 0.35 mV after the thermal fracture experiment of G3. 16 events were recorded with the maximum being 28.72 dB.

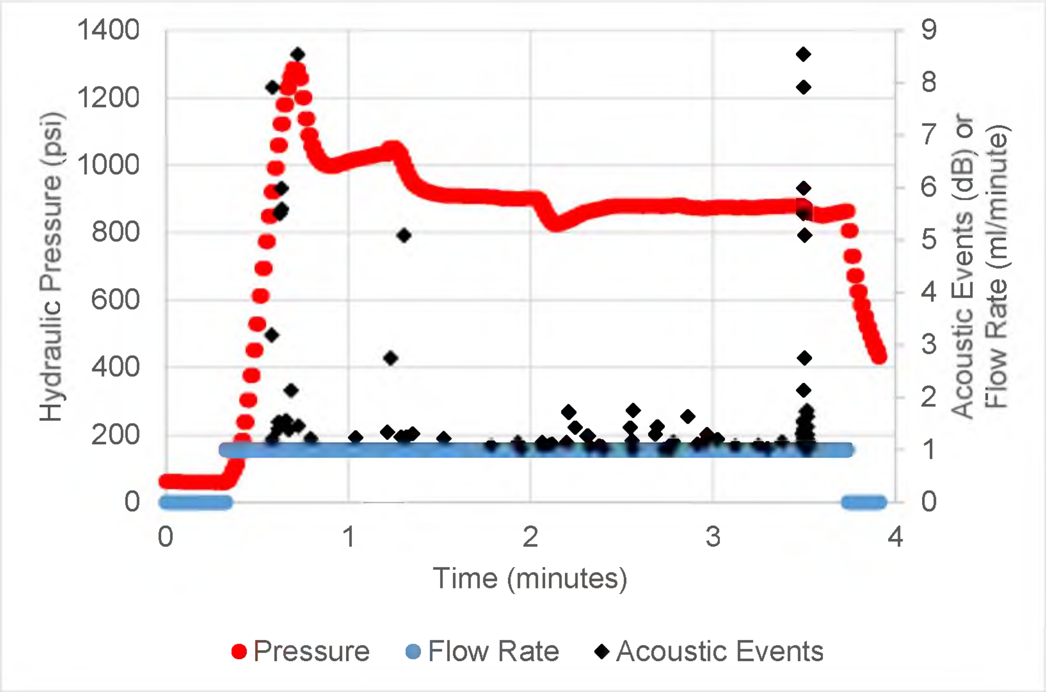

Figure B.11: Pressure, flow rate and acoustic events of the first hydraulic fracture experiment of G3. The acoustic events are the peaks over the threshold of 1 dB with a reference voltage of 0.3 mV. 109 events were recorded with the maximum being 8.54 dB. The flow rate was 1 ml/minute seen in blue. Breakdown pressure was recorded at 1285.7 psi.

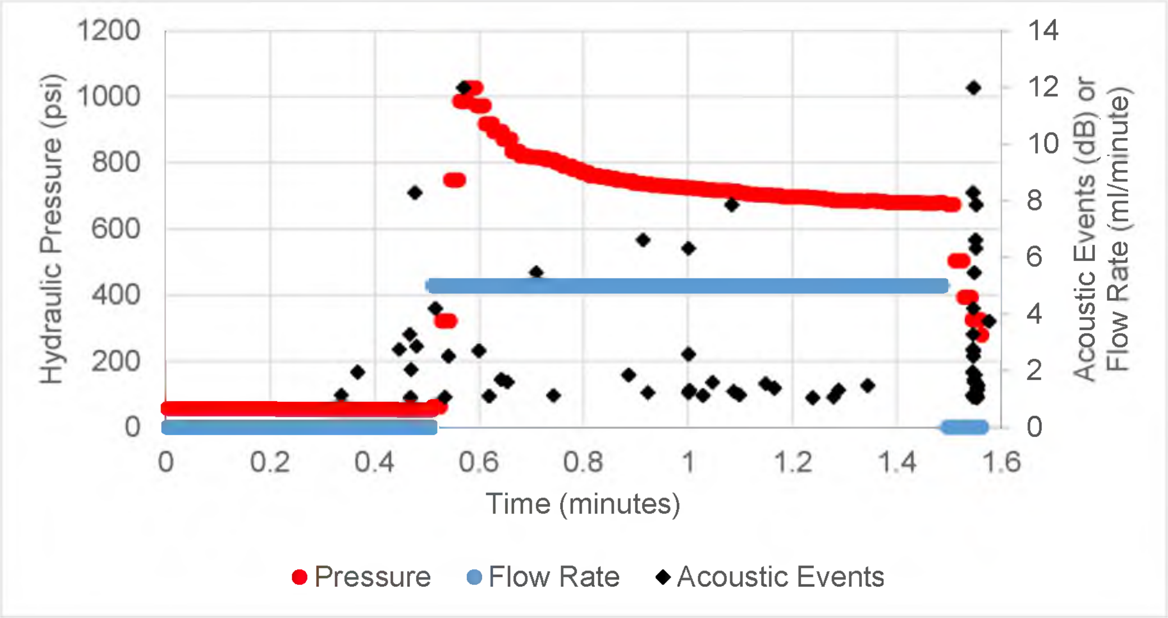

Figure B.12: Pressure, flow rate and acoustic events of the second hydraulic fracture experiment of G3. The acoustic events are the peaks over the threshold of 1 dB with a reference voltage of 0.3 mV. 66 events were recorded with the maximum being 11.98 dB. The flow rate is 5 ml/minute and is seen in blue in the figure. The breakdown pressure is 1026.8 psi.

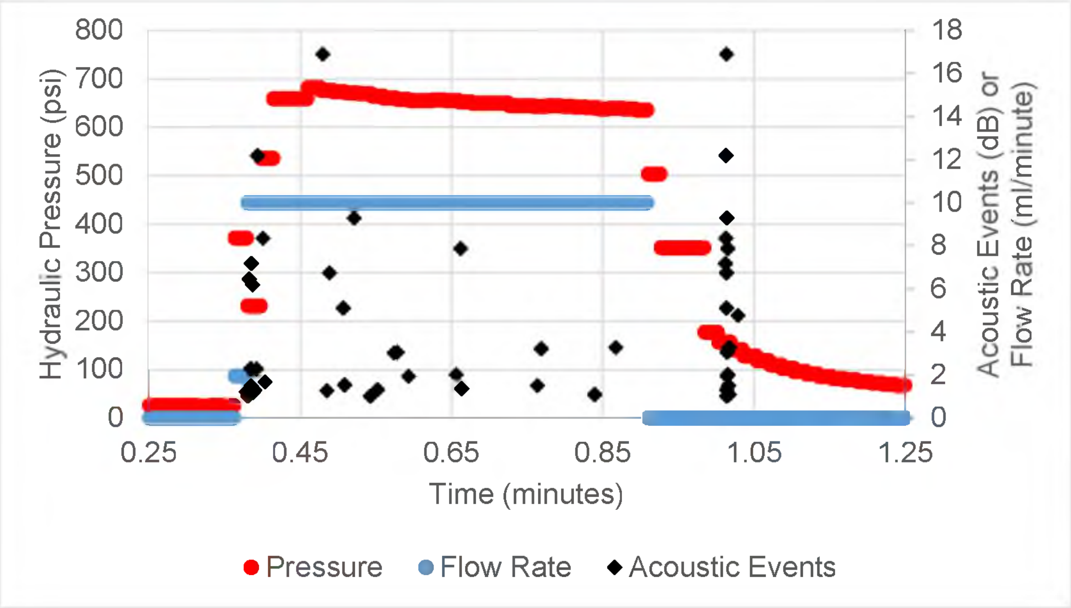

Figure B.13: Pressure, flow rate and acoustic events of the third hydraulic fracture experiment of G3. The acoustic events are the peaks over the threshold of 1 dB with a reference voltage of 0.3. 49 events were recorded with the maximum being 16.90 dB. The flow rate was 10 ml/minute and seen in blue. The breakdown pressure is 682.4 psi.

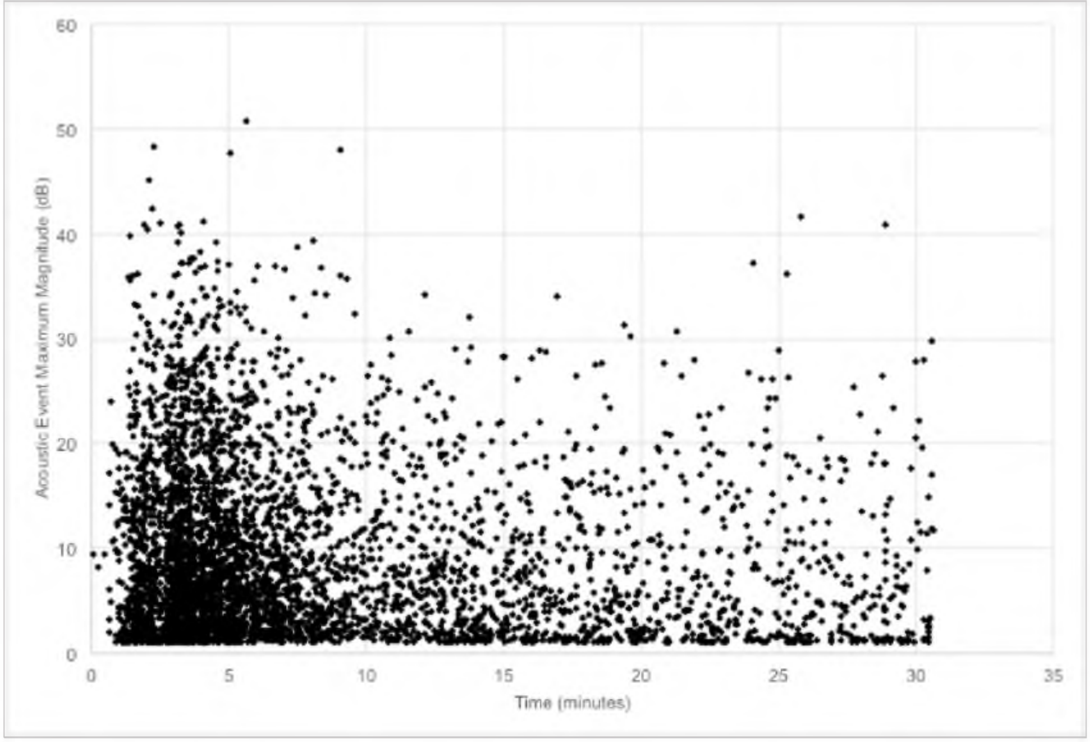

Figure B.14: Peak of all acoustic events over the threshold of 1 dB with a reference voltage of 0.35 mV during the Thermal Fracture of G4. 4305 recorded events with the maximum being 50.79 db.

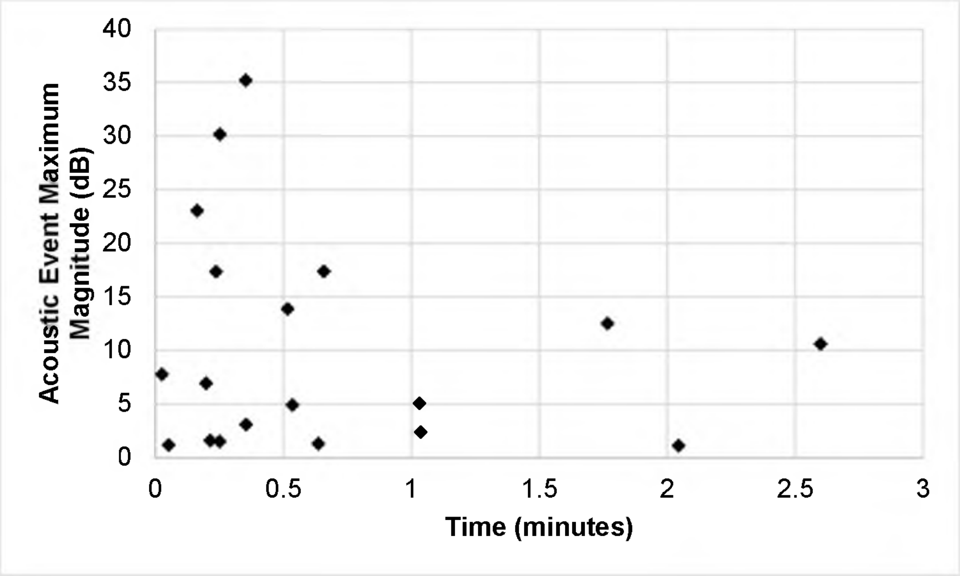

Figure B.15: Peak of all acoustic events over the threshold of 1 dB with a reference voltage of 0.35 mV after the thermal fracture experiment of G4. 19 events were recorded with the maximum being 35.22 dB.

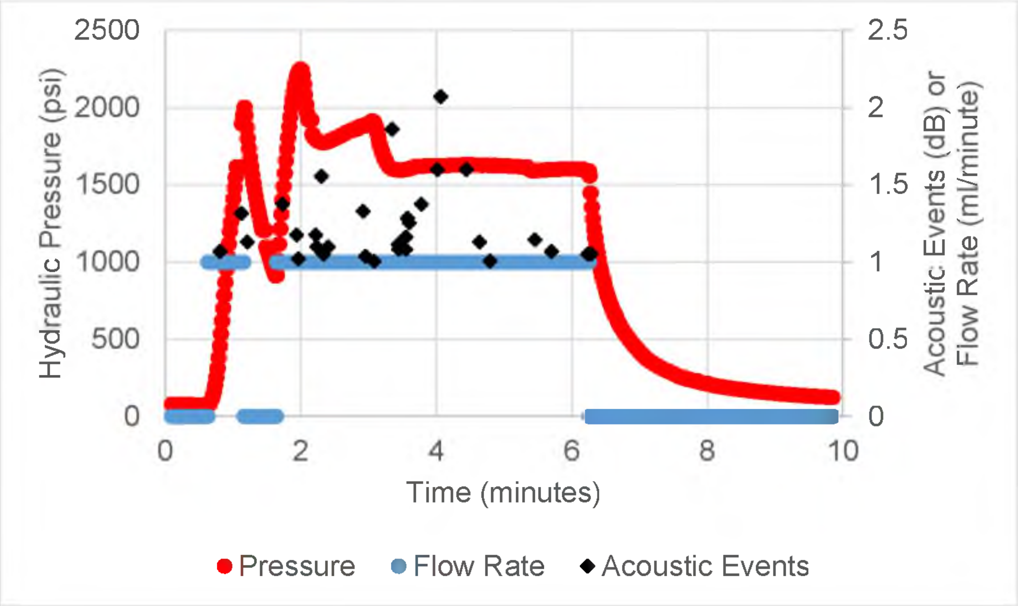

Figure B.16: Pressure, flow rate and acoustic events of the third hydraulic fracture experiment of G4. The acoustic events are the peaks over the threshold of 1 dB with a reference voltage of 0.3. 31 events were recorded with the maximum being 2.07 dB. The flow rate was 1 ml/minute and seen in blue. The breakdown pressure is 2248.4 psi.

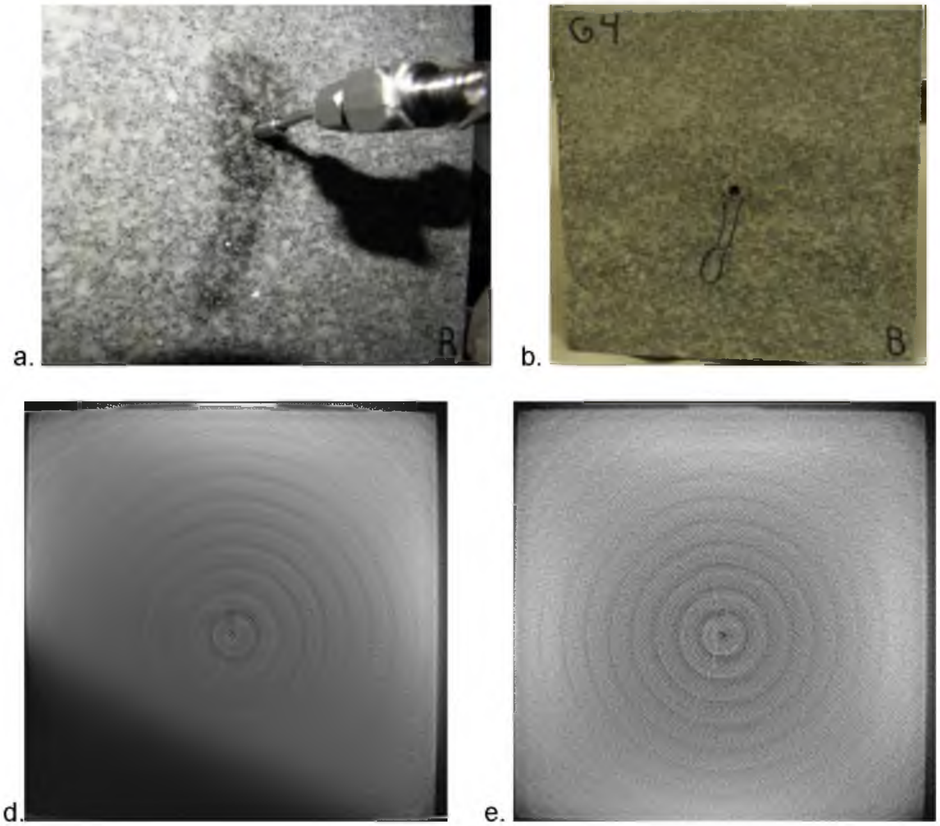

Figure B.17: Photographs and corresponding CT scans of fractured specimen G2 injected with Indium casting alloy, after being hydraulically and thermally fractured. a) Photo of side B after hydraulic fracture experiment showing the fracture surface feature being darkened by wetness. b) Photo of Side B with fracture encircled in black that was detected when liquid exited. c) CT scan of side B, d) CT scan 0.3 inch from side B, and f) CT scan 4.4 inches from side B.

APPENDIX C

ACRYLIC SPECIMEN EXPERIMENTAL RESULTS

C.1 Acrylic Specimen A1

Acrylic Specimen A1 was thermally fractured then hydraulically fractured. Figure C.1 shows A1 before it was fractured. A1 was thermally fractured with liquid nitrogen for 15 minutes. Two circumferential fractures were created (see Figure C.2). A1 was then hydraulically fractured at 3 ml/minute with a breakdown pressure of 930 psi then another at 805 psi. (see Figure C.3). The larger of the two thermally created fractures extended hydraulically (see Figure C.4).

C.2 Acrylic Specimen A2

Acrylic Specimen A2 was hydraulically fractured then thermally fractured. Figure C.5 shows A2 before it was fractured. A2 was hydraulically fractured at a breakdown pressure of 4710 psi. The breakdown flow rate was 5 ml/minute. The flow rate for the experiment was stepped up to counter act the packers leaking (see Figure C.6). A single axial fracture was formed (see Figure C.7). A2 was then thermally fracture with liquid nitrogen for 30 minutes. This resulted in very complicated fracture developing around a subcooled cage of reduced stress. Some of the fractures grew perpendicular to the maximum principal stress (see Figure C.8).

C.3 Acrylic Specimen A3

Acrylic Specimen A3 was thermally fractured then hydraulically fractured. Figure C.9 shows A3 before it was fractured. A3 was thermally fractured with liquid nitrogen for 8.5 minutes. Three circumferential fractures were created. Two axial fractures were also created in-between the two smaller and closer together circumferential cracks (see Figure C.10). A3 was then hydraulically fractured at a flow rate of 1 ml/minute and breakdown was recorded at 1,315 psi (see Figure C.11). The hydraulic fracture extended the largest thermal fracture circumferentially (see Figure C.12).

C.4 Acrylic Specimen A4

Acrylic Specimen A4 was hydraulically fractured then thermally fractured. Figure C.13 shows A4 before it was fractured. A4 was hydraulically fractured at a flow rate of 1 ml/minute and a breakdown pressure of 3,501 psi (see Figure C.14). A single axial fracture was formed (see Figure C.15). A4 was then thermally fractured with liquid nitrogen for 30 minutes. This resulted in very complicated fracture developing around a subcooled cage of reduced stress. Some of the fractures grew perpendicular to the maximum principal stress (see Figure C.16).

Figure C.1: Horizontal view of specimen A1 after machined but before experimented on.

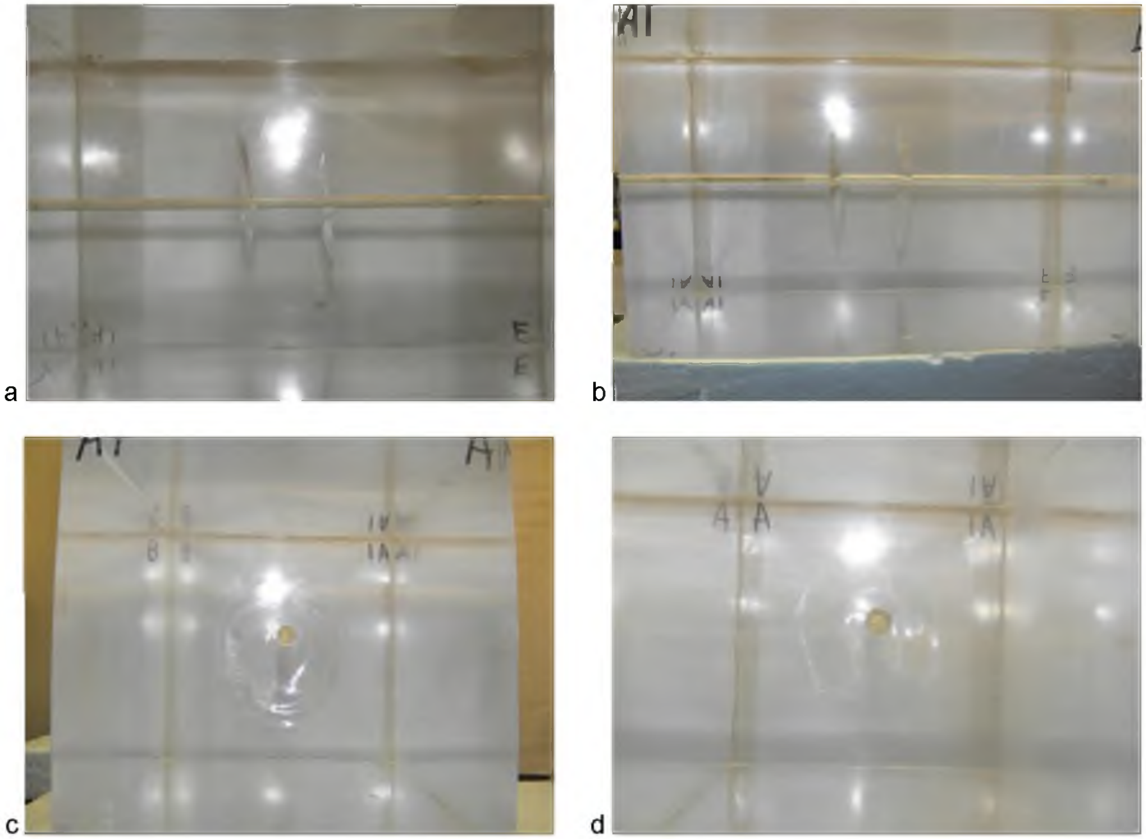

Figure C.2: A1 post thermal fracture pictures. a) Max stress view. b) Horizontal view. c) Axial view side A. d) Axial view of side B.

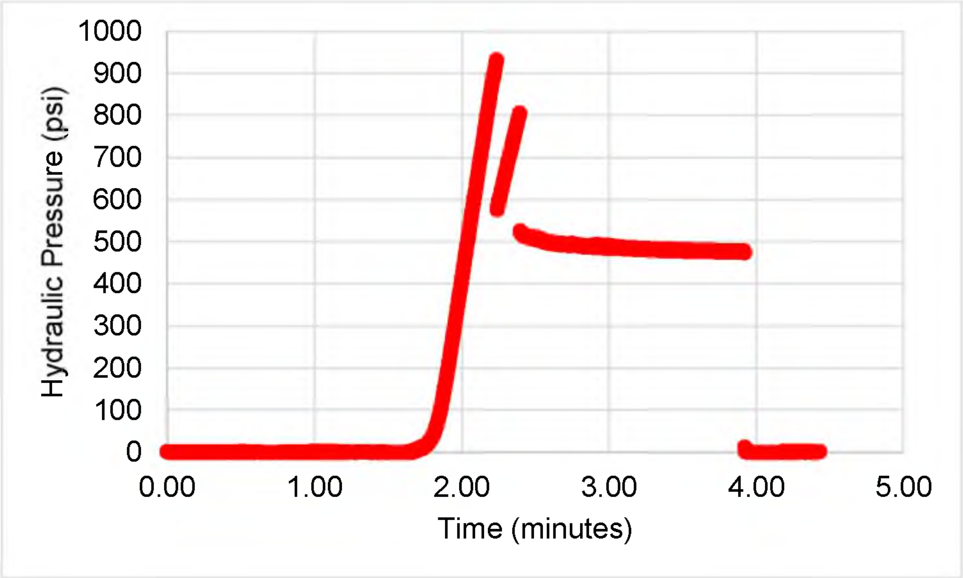

Figure C.3: Pressure data of A1 hydraulic fracture post thermal fracture. Showing two peaks at 930 psi and 805 psi.

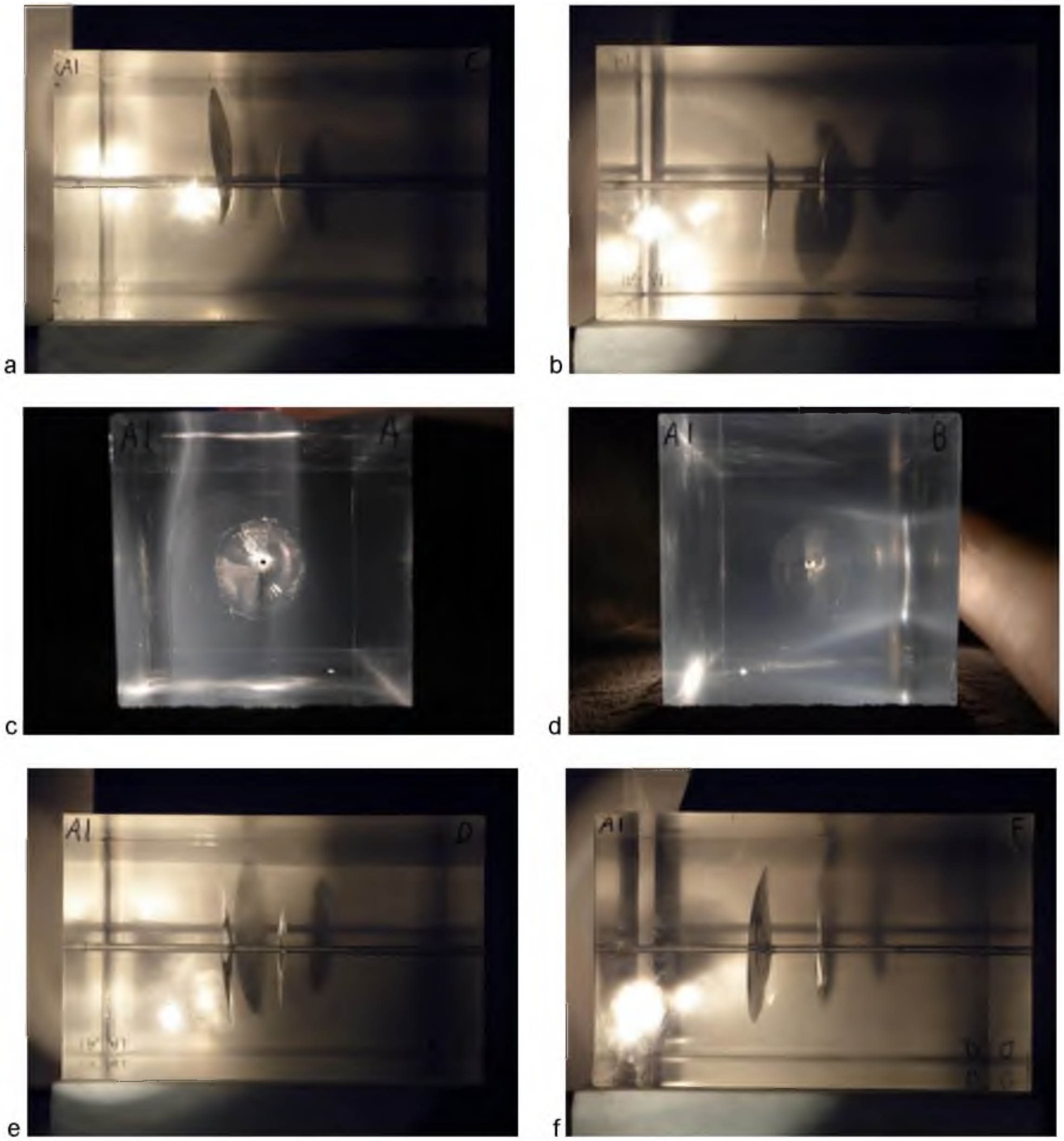

Figure C.4: A1 post thermal then hydraulic fracturing. a) Max stress view side C. b) Max stress view side E. c) Axial view side A. d) Axial view side B. e) Horizontal view side D. f) Horizontal view side F.

Figure C.5: Horizontal view of specimen A2 after machined but before experimented on.

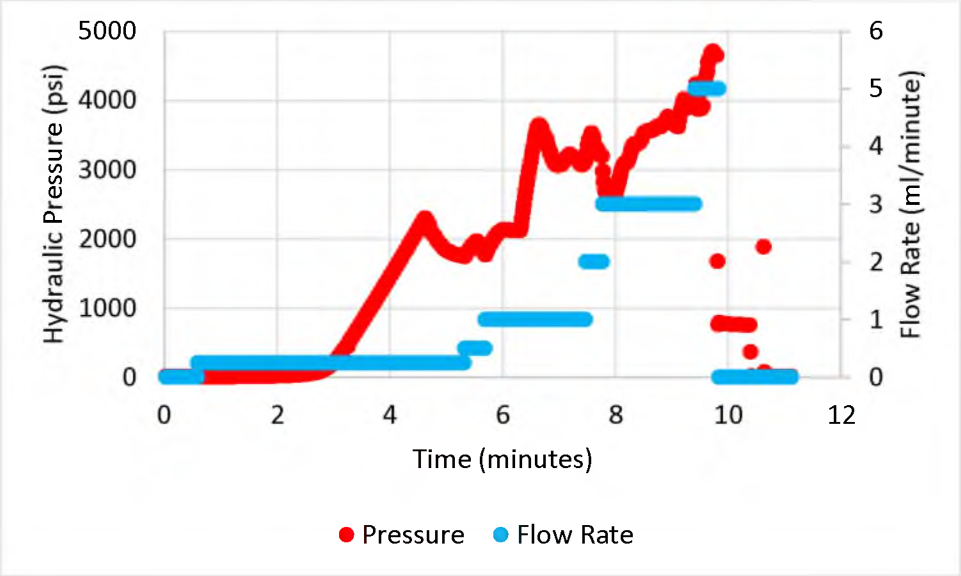

Figure C.6: Pressure and flow rate data of A2 hydraulic fracture. Showing breakdown pressure peaking at 4,710 psi.

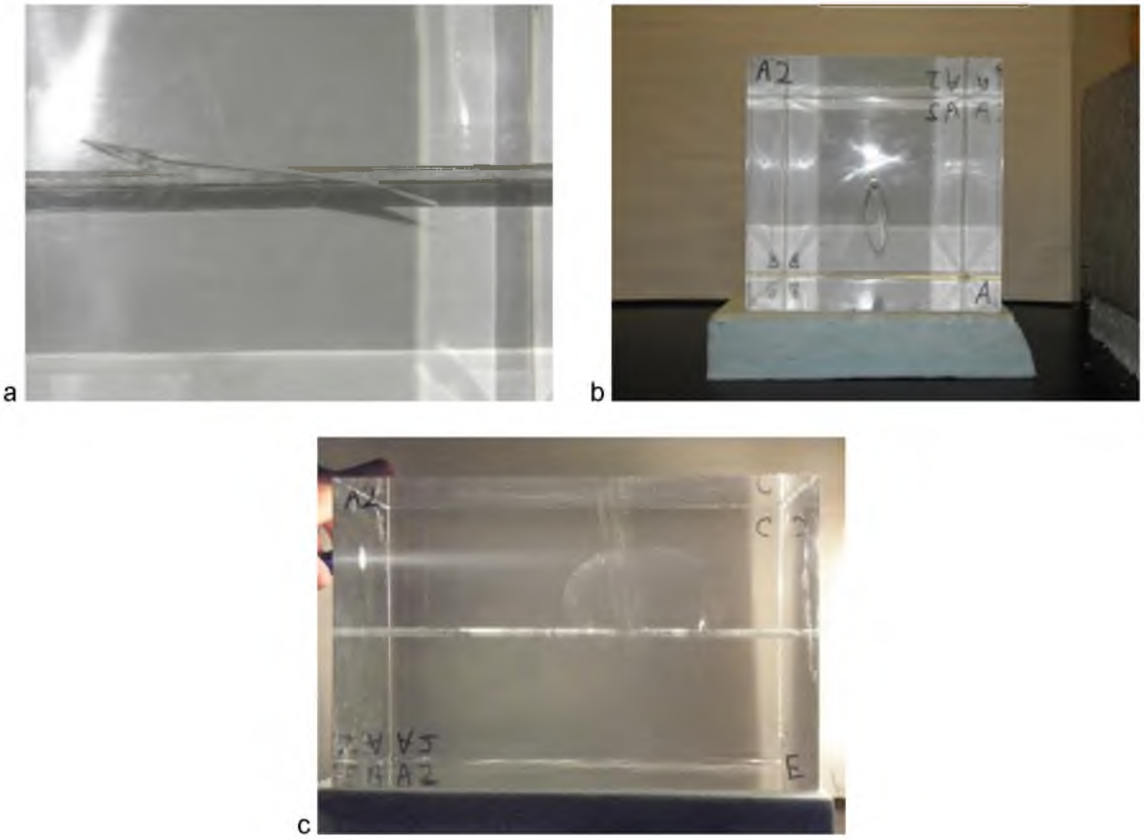

Figure C.7: A2 post hydraulic fracture pictures. One hydraulic fracture formed that is 4.62 inches long and 2.37 inches tall. It is 10.86° from the axial through hole and 3° from vertical. a) Max stress view. b) Axial view. c) Horizontal view.

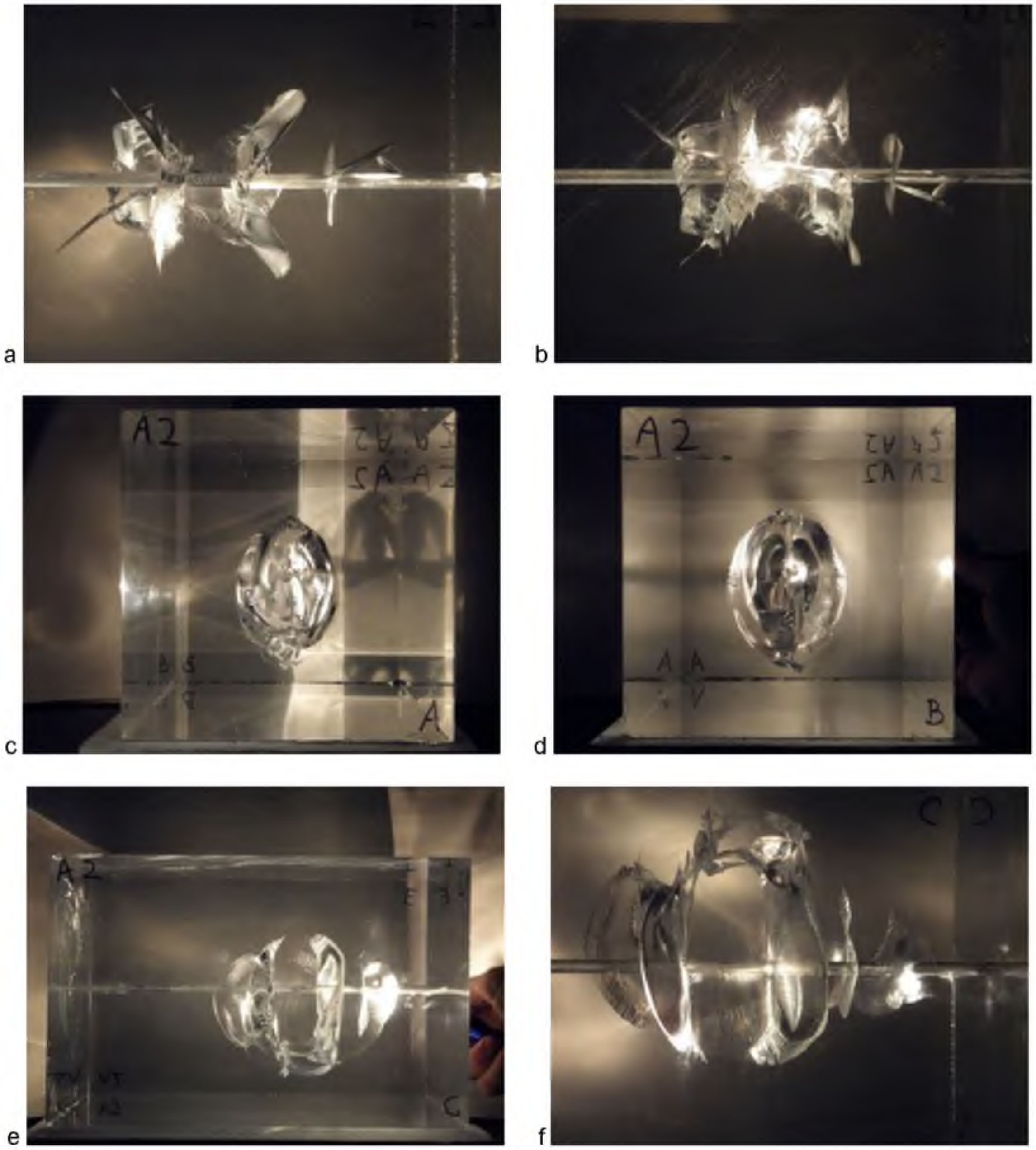

Figure C.8: A2 post hydraulic then thermal fracturing. a) Max stress view side D. b) Max stress view side F. c) Axial view side A. d) Axial view side B. e) Horizontal view side C. f) Horizontal view side E.

Figure C.9: Horizontal view of specimen A3 after machined but before experimented on.

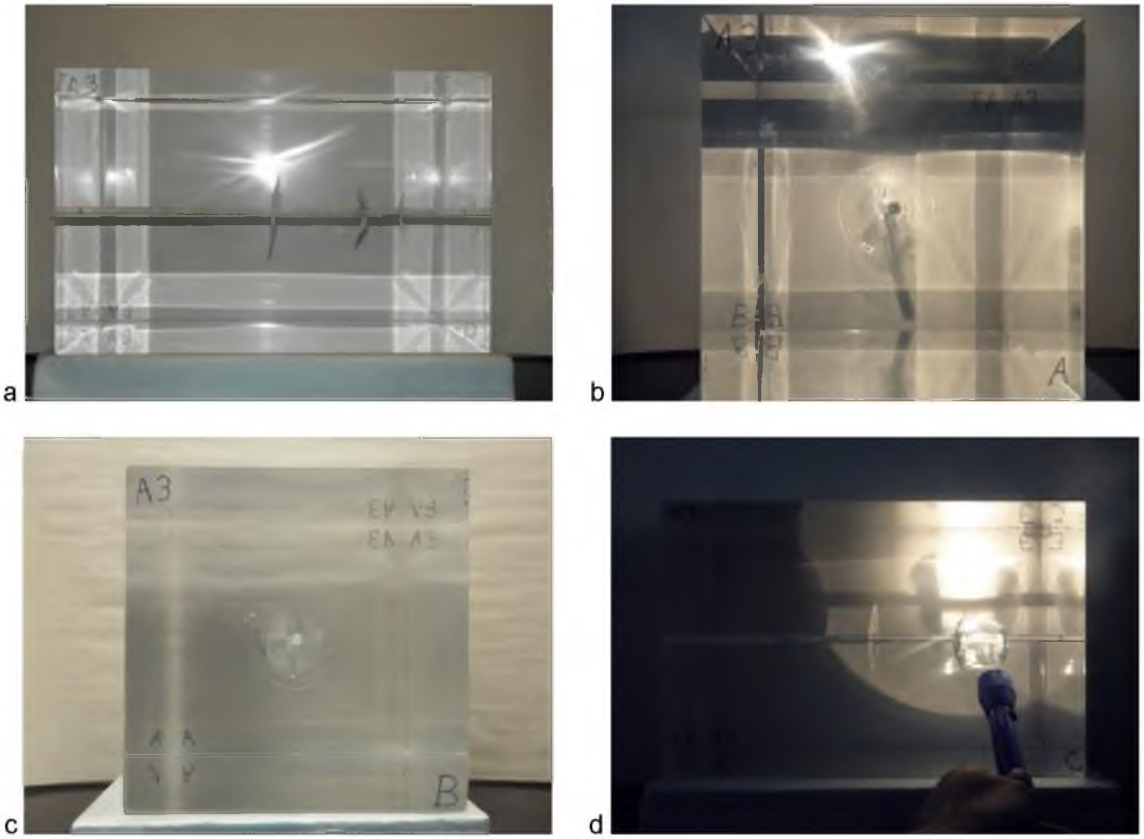

Figure C.10: A3 post thermal fracture pictures. a) Max stress view. b) Axial view side A. c) Axial view side B. d) Horizontal view.

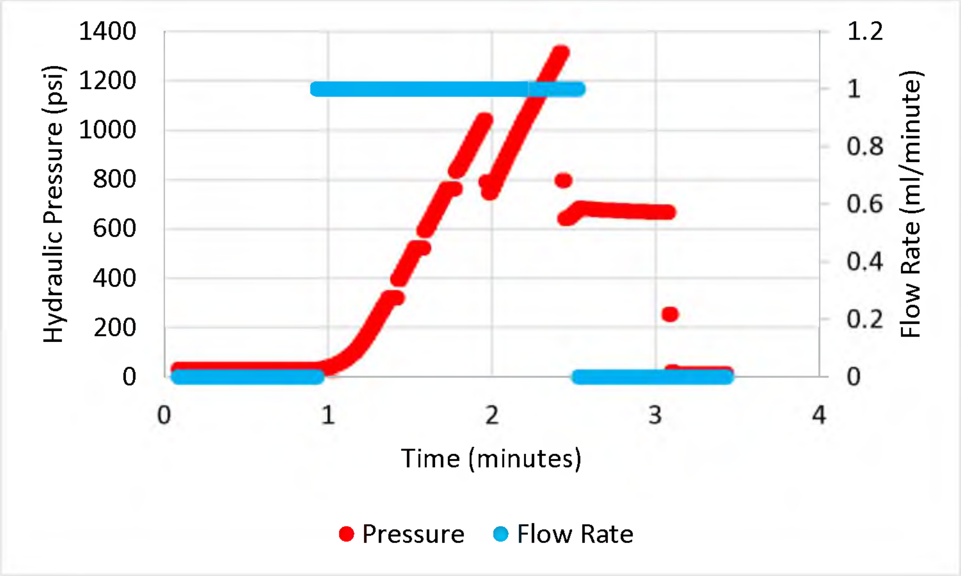

Figure C.11: Pressure and flow rate data of A3 hydraulic fracture post thermal fracture. Showing breakdown pressure peaking at 1,315 psi.

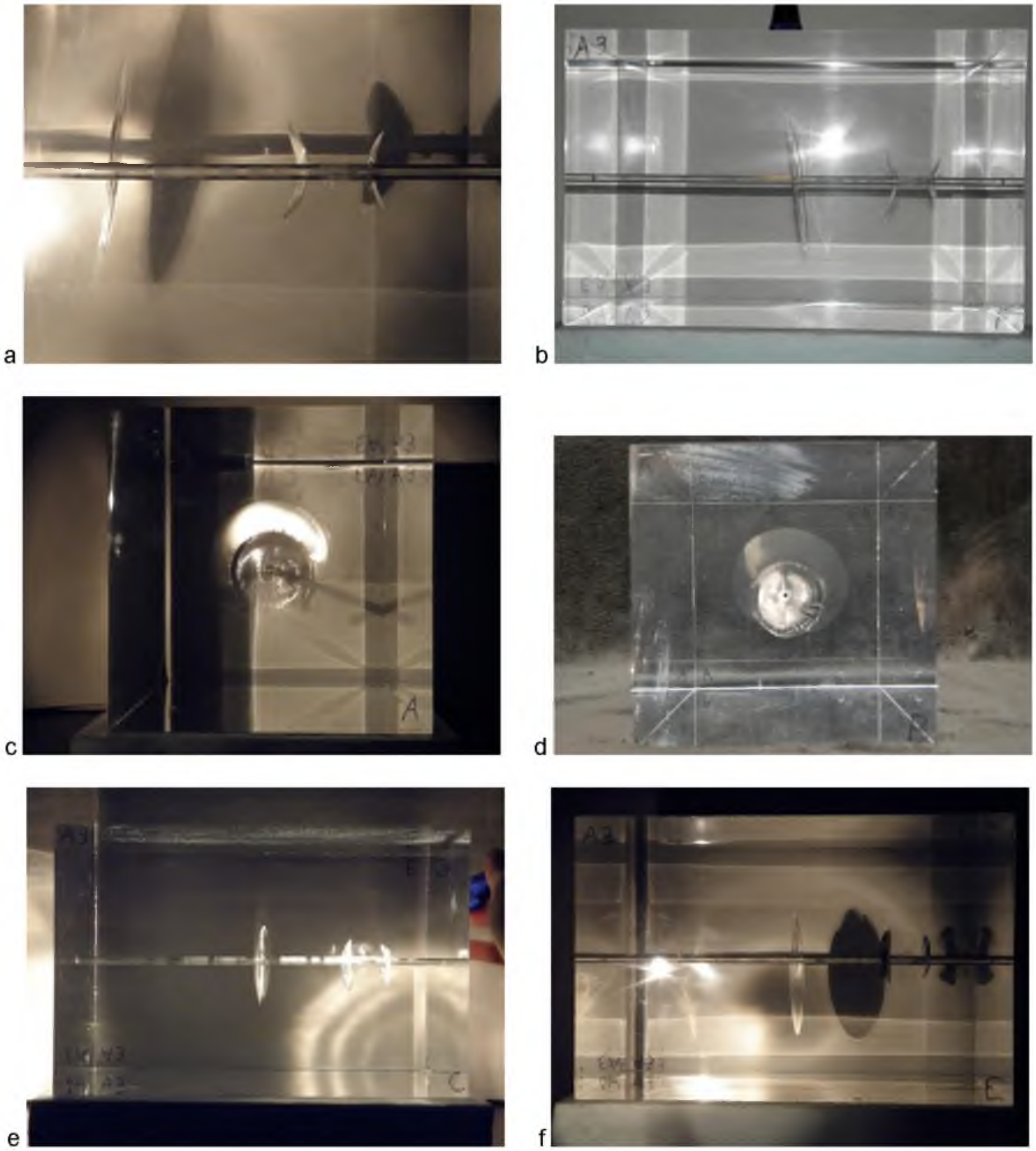

Figure C.12: A3 Post Hydraulic then Thermal Fracturing. a) Max stress view side D. b) Max stress view side F. c) Axial view side A. d) Axial view side B. e) Horizontal view side C. f) Horizontal view side E.

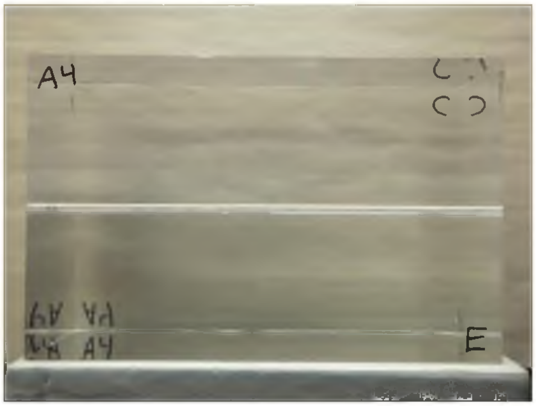

Figure C.13: Horizontal view of specimen A4 after machined but before experimented on.

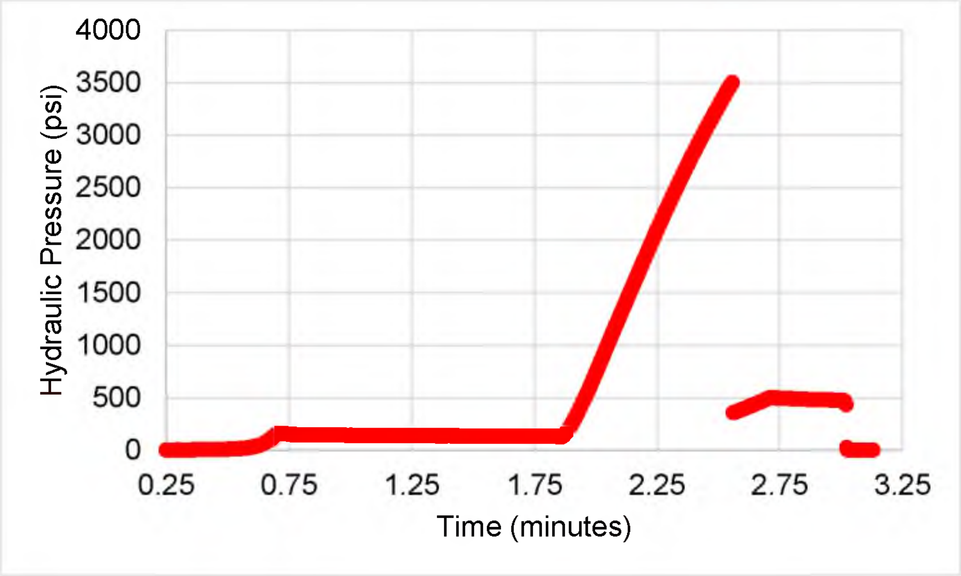

Figure C.14: Pressure data of A4 hydraulic fracture. Showing breakdown pressure peaking at 3,501 psi.

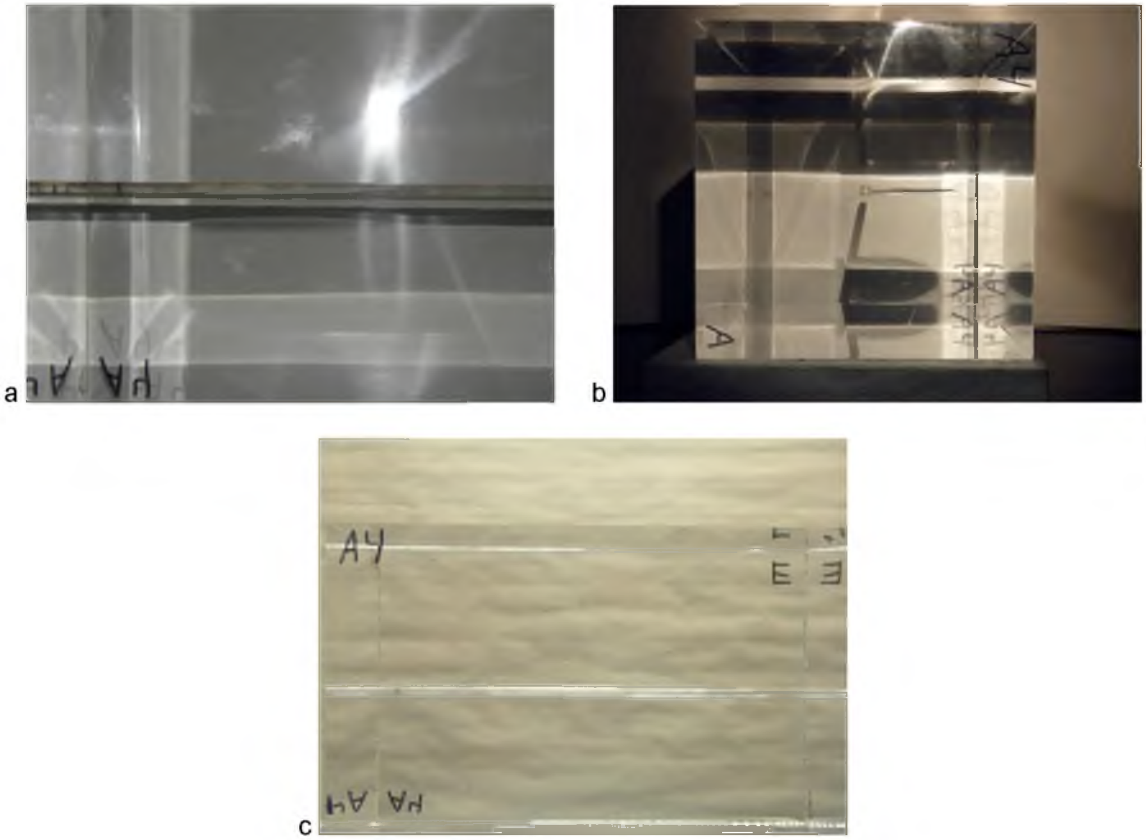

Figure C.15: Post hydraulic fracture pictures. a) Max stress view. b) Axial view. c) Horizontal view.

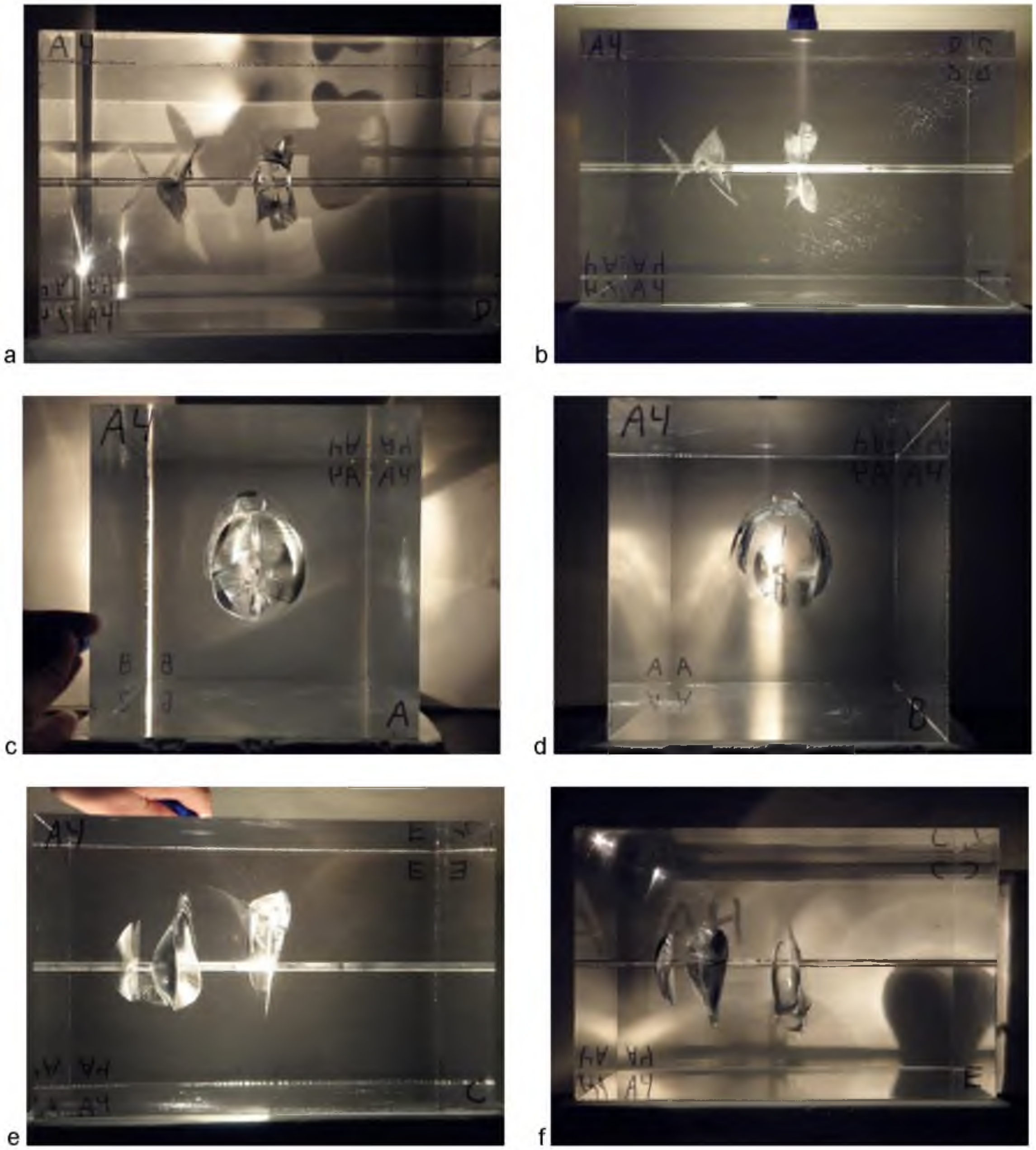

Figure C.16: A4 post hydraulic then thermal fracturing. a) Max stress view side D. b) Max stress view side F. c) Axial view side A. d) Axial view side B. e) Horizontal view side C. f) Horizontal view side E.

APPENDIX D

FINITE DIFFERENCE CODE VERIFICATION

Verifications are made with simplified analytical solutions to ascertain that the code is computing the equations correctly. Validations are made against physical experiments in order to assure that the computer code is running the correct equations. The validation for the finite difference model can be found in section 2.3.2 Numerical Simulation Methodology. The code is verified by comparing the computational model with the same inputs as known analytical solutions, then comparing the two.

D.1: Verification 1 – 1D Solid Conduction

Verification 1 compares the Finite Difference code to the analytical solution of temperature of an infinite hollow cylinder with the inner and outer radius being held at constant but different temperatures, equation D.1 [1]. This code verifies that the finite difference model is calculating conduction to steady state in the r direction correctly.

$$T(r) = \frac{T_a \ln(b/r) + T_b \ln(r/a)}{\ln(b/a)} \tag{D.1}$$

where inner radius is $r=a$, outer radius is $r=b$, T_a is the temperature at the inner radius, and T_b is the temperature at the outer radius. The relative normal error (L_2) between the model and the analytical temperature profiles is calculated to test agreement.

The verification was run with the inner annulus held at 300 K and the outer at 550 K (see Figure D.1). The outer radius is 30 cm and inner is 3 cm and the length in z is set to 10 cm. Under these inputs the numerical model calculated the time to steady state temperature at 27.667 hours. The relative normal error was 0.0002733. This showed great agreement with a difference of only 0.02733% (see Figure D.2).

D.2: Verification 2 – 2D Solid Conduction

Verification 2 is a comparison of the finite difference model with the analytical steady state solution of the temperature of a finite hollow cylinder with r = a maintained at a temperature that is a function of z, f(z), and all other boundaries held at a temperature of zero (see equations D.2 and D.3) [2]:. This verifies that the finite difference model is calculating conduction in 2-dimensions correctly.

$$T(r,z) = \frac{2}{l}\sum_{n=1}^{\infty}\frac{F_o\left({n\pi r}/_{l};{n\pi b}/_{l}\right)}{F_o\left({n\pi a}/_{l};{n\pi b}/_{l}\right)}\sin\frac{n\pi z}{l}\int_0^l f(z')\sin\frac{n\pi z'}{l}\,dz' \tag{D.2}$$

with:

$$F_o(r;z) = I_o(r)K_o(z) - K_o(r)I_o(z) \tag{D.3}$$

where *l* is the length of the cylinder, I_0 is a modified Bessel function of the first kind of order zero , K_0 is a modified Bessel function of the second kind of order zero, and F_0 is merely a simplifying function that contains within it the modified Bessel functions. Once again the relative normal error (L_2) between the model and the analytical temperature profiles are calculated to test agreement. Figures D.3 and D.4 show the temperature distributions of the numerical model and analytical solution respectively. The difference between them is mapped in Figure D.5. Figure D.6 shows the temperature distribution in the fluid flow in the annulus. L_2 was found to be 0.0087408.

D.3: Verification 3 – Heat Flux BC in Solid, Constant Temperature Walls

Verifications 1 and 2 tested the ability of the finite difference model to accurately calculate conduction in a solid impermeable finite hallow cylinder. Verification 3 compares the model with an analytical steady state solution of a heat flux (f(z)) applied to the inner radius of a finite hollow cylinder while all other boundaries are kept at a temperature of zero (see equations D.4 and D.5) [3]. This will verify the models ability to have a heat flux boundary condition.

$$T(r,z) = -\frac{2}{K\pi}\sum_{n=1}^{\infty}\frac{F_o\left({n\pi r}/{l};{n\pi b}/{l}\right)}{nF_1\left({n\pi a}/{l};{n\pi b}/{l}\right)}\sin\frac{n\pi z}{l}\int_0^l f(z')\sin\frac{n\pi z'}{l}\,dz' \tag{D.4}$$

with:

$$F_1(r;z) = I_1(r)K_o(z) + K_1(r)I_o(z) \tag{D.5}$$

where *K* is the thermal conductivity, I_1 is the modified Bessel function of the first kind of the order one, and K_1 is the modified Bessel function of the second kind of the order one. F_1 is a simplifying equation. The relative normal error (L_2) between the model and the analytical temperature profiles was found to be 0.010777 and is shown in Figure D.7.

D.4: Verification 4 – Heat Flux BC in Solid, Insulated Walls

Verification 4 is a second test that the model can accurately calculate a heat flux boundary. A heat flux is applied to the inner radius of the infinite hollow cylinder. At z = 0 and z = L the boundaries are insulated, and the outer radius is held at a constant temperature. The code is verified by comparing the given heat flux to the calculated heat flux through the solid media via Equation D.6 derived by dividing equation 3.27 from Incropera and DeWitt [4] by the area that the heat flux is applied to.

$$q" = \frac{k(T_1 - T_2)}{r_1 \ln\left({r_2}/{r_1}\right)} \tag{D.6}$$

Figure D.8 shows the temperature distribution of the numberical model. Figure D.9 shows the results of the analysis and the error to be 0.0006%.

D.5: Verification 5 – Time Dependent 1D Solid Verification

The time dependency of the solid in the model is verified against a 1-dimensional transient Heat Equation D.8. Equation D.8 is solved using a semi-infinite and line heat source boundary conditions (Equations D.9 and D.10). A constant temperature initial condition is also utilized (Equation D.11). Equation D.12 is the Boltzmann Transformation that is used to solve the problem into an exponential integral, Equation D.13.

$$\frac{\alpha}{r}\frac{\partial\left(r\frac{\partial T}{\partial r}\right)}{\partial r} = \frac{\partial T}{\partial t} \tag{D.8}$$

$$T \rightarrow T_{initial} \ \ as\, r \rightarrow \infty \tag{D.9}$$

$$\lim_{r \to 0}\left(-2\pi r h k \frac{\partial T}{\partial r}\right) = q \tag{D.10}$$

$$T(r) = T_{initial} \ \ when\, t = 0 \tag{D.11}$$

$$s = \frac{\rho c_p r^2}{4kt} \tag{D.12}$$

$$T(r,t) = T_{initial} + \frac{q}{4\pi k h}\int_{\frac{\rho c_p r^2}{4kt}}^{\infty} \frac{e^{-u}}{u}\,du \tag{D.13}$$

The exponential integral from equation D.13 is solved directly in matlab. The verification was run with the initial temperature at 361.25 K, and with a heat source of -900 W. The outer radius is set to 15 cm and the inner is 0.333 cm with a length (z) of 5 cm (see Figure D.10). The nodes per cm was set to 10. Under these inputs the model calculated the relative normal error at 0.00084554 as seen in Figure D.11 at a time of 0.2 hours.

D. 6: Verification 6 – Flow Verification

Verification 6 is a comparison of the finite difference model with the analytical steady state solution of plug flow in a pipe with a constant inlet temperature and a constant wall temperature (equation D.14) [5]. This verifies the models ability to determine the temperature profile of the fluid flow in the fracture accurately.

$$\frac{T-T_w}{T_{in}-T_w} = \sum_{n=1}^{\infty} \frac{2}{\beta_n J_1(\beta_n)} e^{-\beta_n{}^2 \frac{\alpha}{r_w v_0} * \frac{x}{r_w}} J_0\left(\beta_n \frac{r}{r_w}\right) \tag{D.14}$$

where β_n are the n^{th} roots of $J_0(\beta)=0$, J_0 and J_1 are the zero and first order Bessel functions, and v_0 is the plug flow velocity. The difference between the model and the analytical solutions is shown in Figure D.12. The L2 normalized error is 0.0038.

D.7: Verification 7 – Time Dependent Fluid Verification

The time dependency of the flow in the model is verified against a 1-dimensional transient advection-diffusion solution (Equation D.15). The partial differential Equation D.15 is transformed into an ODE using the similarity variable zeta (Equation D.16) [6]. The initial condition is that everything is set to zero temperature (Equation D.17). Equations D.18 and D.19 are the boundary conditions. Equation D.20 is a valid solution for temperature dispersion in 1-dimensional flow when zeta is greater than zero.

$$\frac{\partial T}{\partial t} + v\frac{\partial T}{\partial z} = \alpha\frac{\partial^2 T}{\partial z^2} \tag{D.15}$$

$$\zeta = \frac{(z-vt)}{2\sqrt{\alpha t}} \tag{D.16}$$

$$T = 0\, When\ \ time = 0 \tag{D.17}$$

$$T = T_{inj.}\ @\, \zeta < 0 \tag{D.18}$$

$$T = 0\, @\, \zeta = \infty \tag{D.19}$$

$$T(z,t) = \frac{T_{inj.}}{2} erfc\left(\frac{(z-vt)}{2\sqrt{\alpha t}}\right) \tag{D.20}$$

The complimentary error function in equation 31.6 is solved directly in matlab. The verification was run for two hours with the model having a length in *z*, *r* being 25 and 4 cm respectively. The width of the fracture in the *r* direction is 3 cm (Figure D.13). The model was run for a simulated 2 hours with a grid spacing of 10 nodes per cm. Under these inputs the model calculated the relative normal error at 0.015901 as seen in Figure D.14.

D.8: Verification 8 – Thermoelastic Verifications of Code

Verification 8 compares an analytical thermoelastic solution with numerical model. Equation D.21 is the analytical solution for the plane strain thermal tangential stress of a hollow cylinder with "radial temperature variation." [7] Equations D.22 and D.23 are used for the plane strain condition of equation D.21.

$$\sigma_\theta = \frac{\alpha_1 E_1}{r^2}\left[\frac{r^2+a^2}{b^2-a^2}\int_a^b Tr\,dr + \int_a^r Tr\,dr - Tr^2\right] \tag{D.21}$$

$$E_1 = \frac{E}{1-v^2} \tag{D.22}$$

$$\alpha_1 = \alpha(1+v) \tag{D.23}$$

where sigma theta is the tangential stress, or the stress perpendicular to the r-z plane, alpha is the linear coefficient of thermal expansion, and *r* is the radius. The result is shown in Figure D.15 to be 5.7% difference. The larger difference is expected because the numerical model is not in plane strain, but rather a full 2-dimensional code. Figures D.16, D.17, D.18, D.19, and D.20 are the temperature, radial displacement, axial displacement, tangential stress, and axial stress of the numerical model, respectively.

D.9: Verification 9 – Ansys Comparison

Ansys is a 2nd order finite element commercial code known for heat transfer and stress mechanic simulating. The numerical model written in Matlab was compared to an Ansys model of the same geometry. For the same heat transfer inputs and boundary conditions the tangential stress was compared between the two codes along the radius in the axial middle. The normalized error was calculated and convergence (2% error) was achieved with refined mesh sizes (see Figure D.21). Figures D.22 and D.23 show the temperature profiles and tangential stress of the two codes side by side.

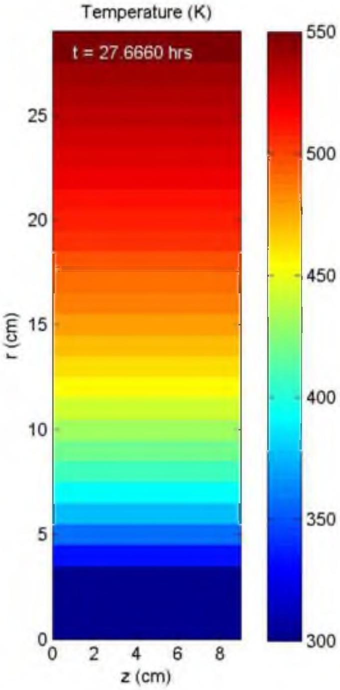

Figure D.1: Temperature profile at steady state.

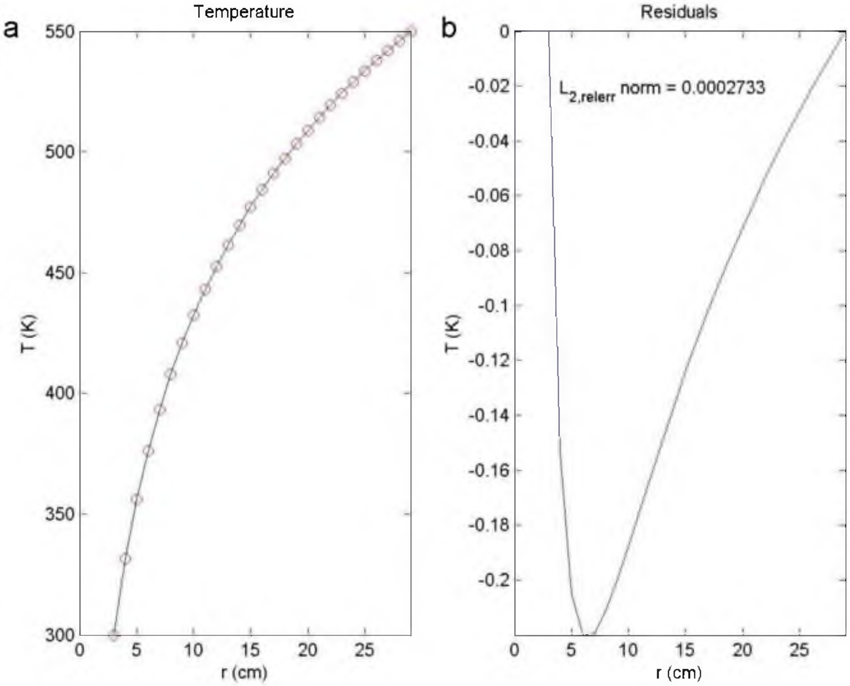

Figure D.2: Verification 1 results. a. Comparison of the analytical model (solid black line) and the FD model (red dots) b. The error along the radius.

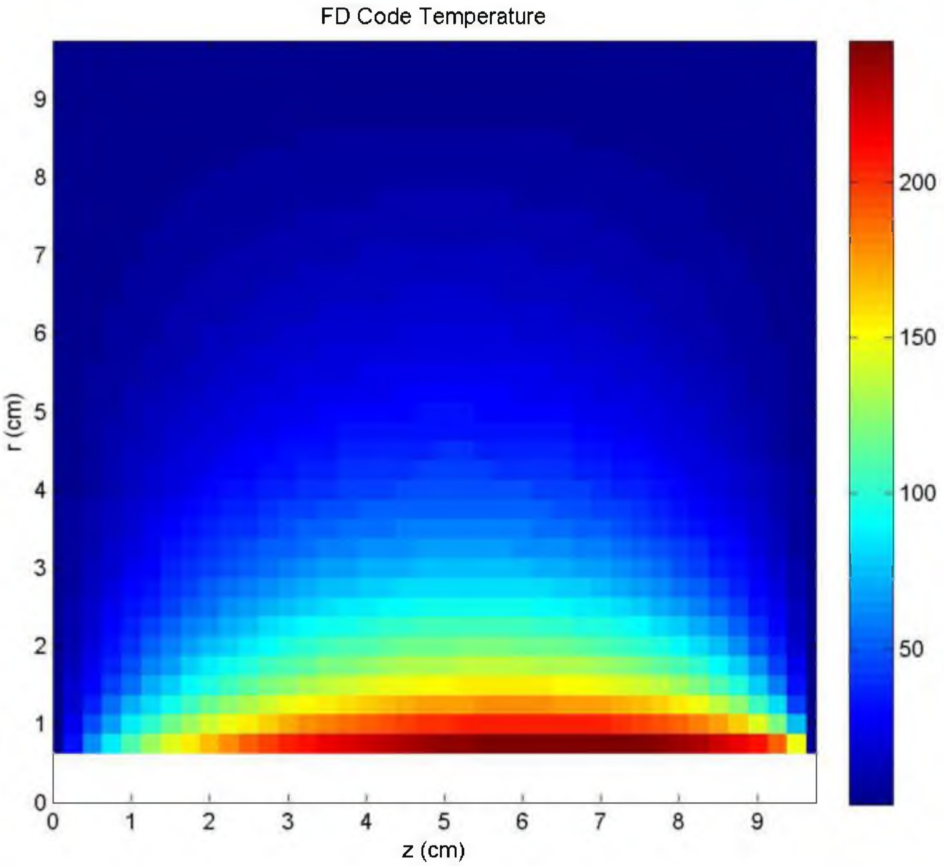

Figure D.3: The finite difference calculated steady state temperature profile the change in temperature in z is caused by simulated fluid flow. SS = 1.26 hours.

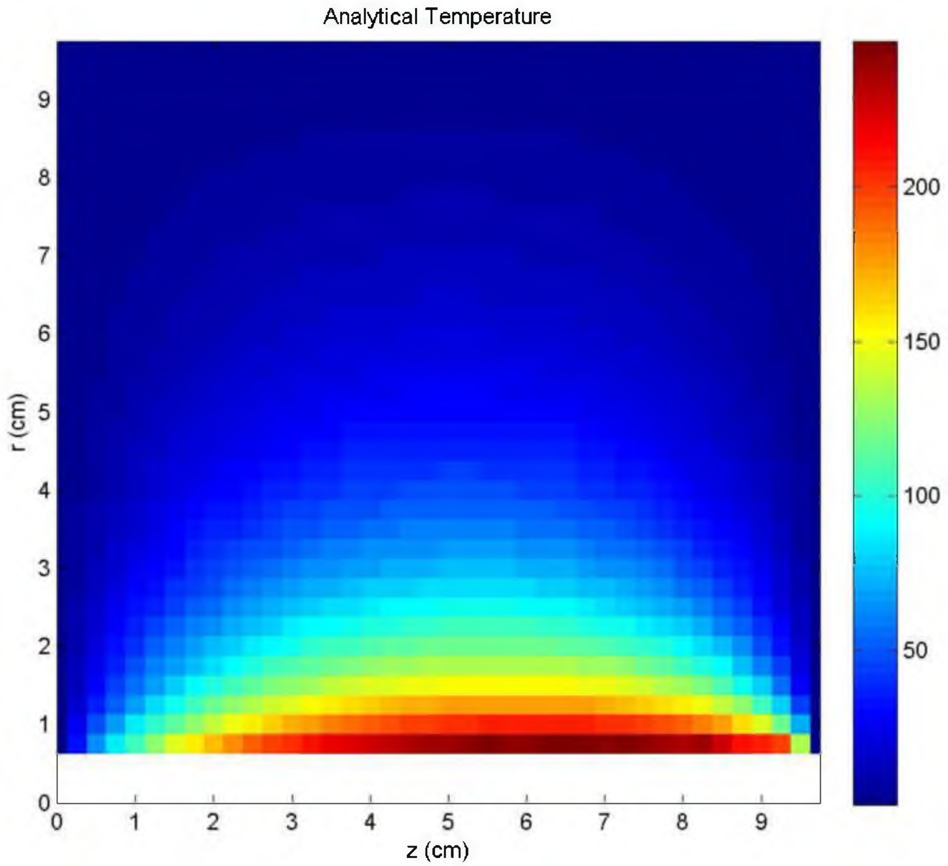

Figure D.4: The analytical solution of the 2-dimensional temperature profile caused by the function f(z) that is calculated from the rock-water (nodes 7-9) nodal temperatures found at steady state.

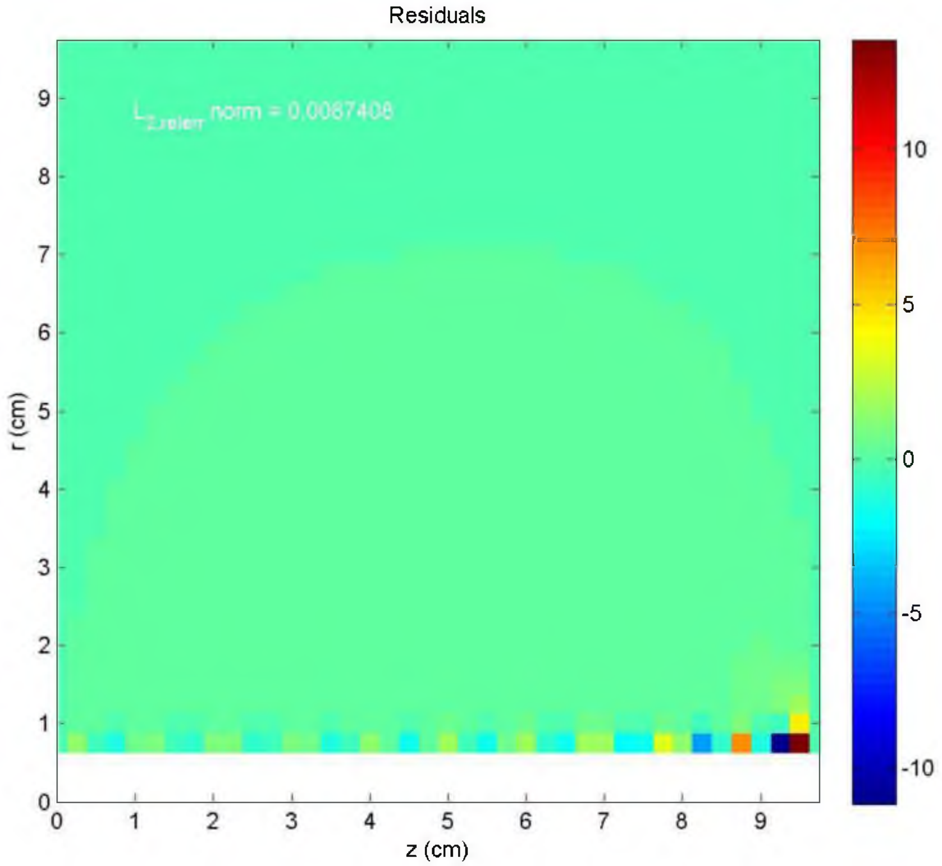

Figure D.5: The residuals of the temperature profile.

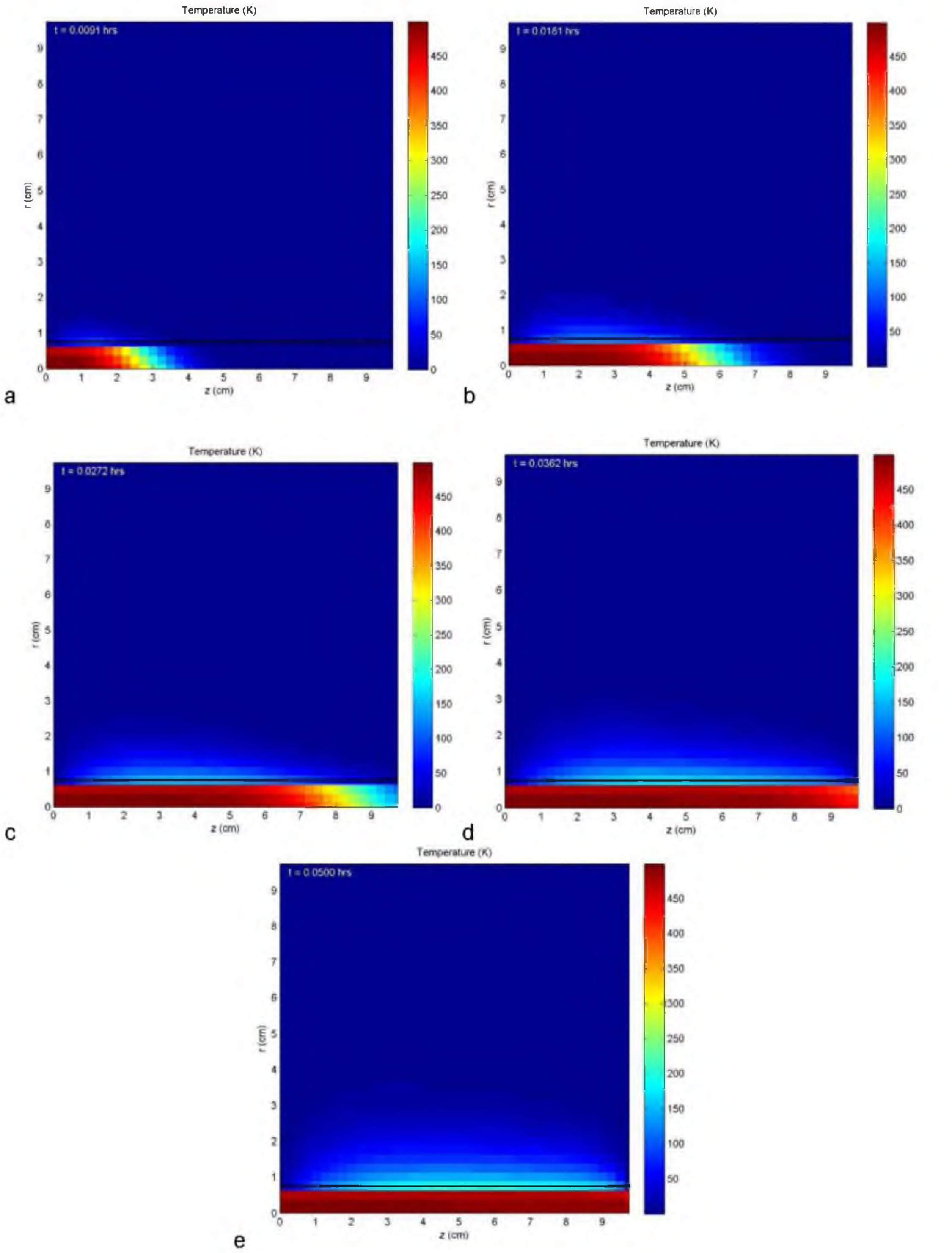

Figure D.6: The temperature profile of the finite difference code: a – e are illustrating the temperature change in the fluid filled annulus at times 0.546, 1.086, 1.632, 2.172, and 3 minutes respectively at 700 ml/hr.

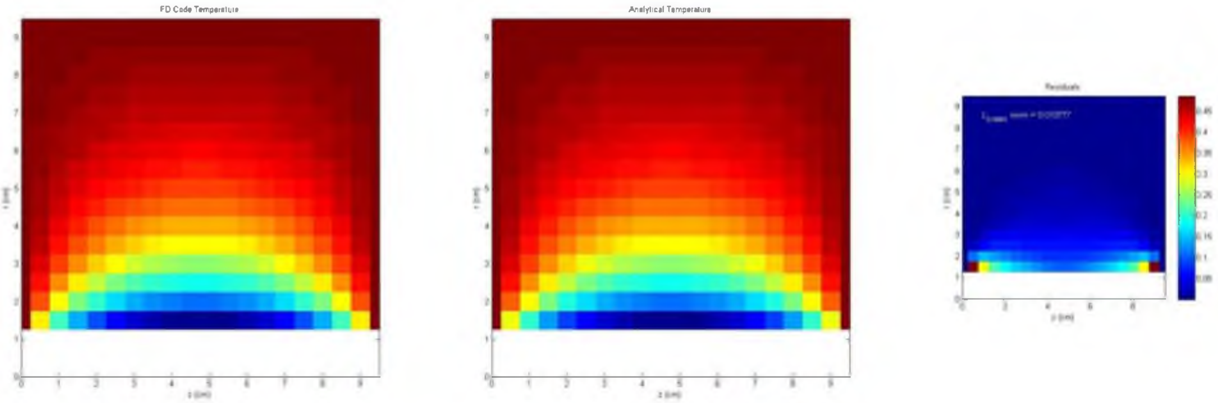

Figure D.7: Temperature profile of the finite difference code illustrating conduction in solid impermeable finite hollow cylinder.

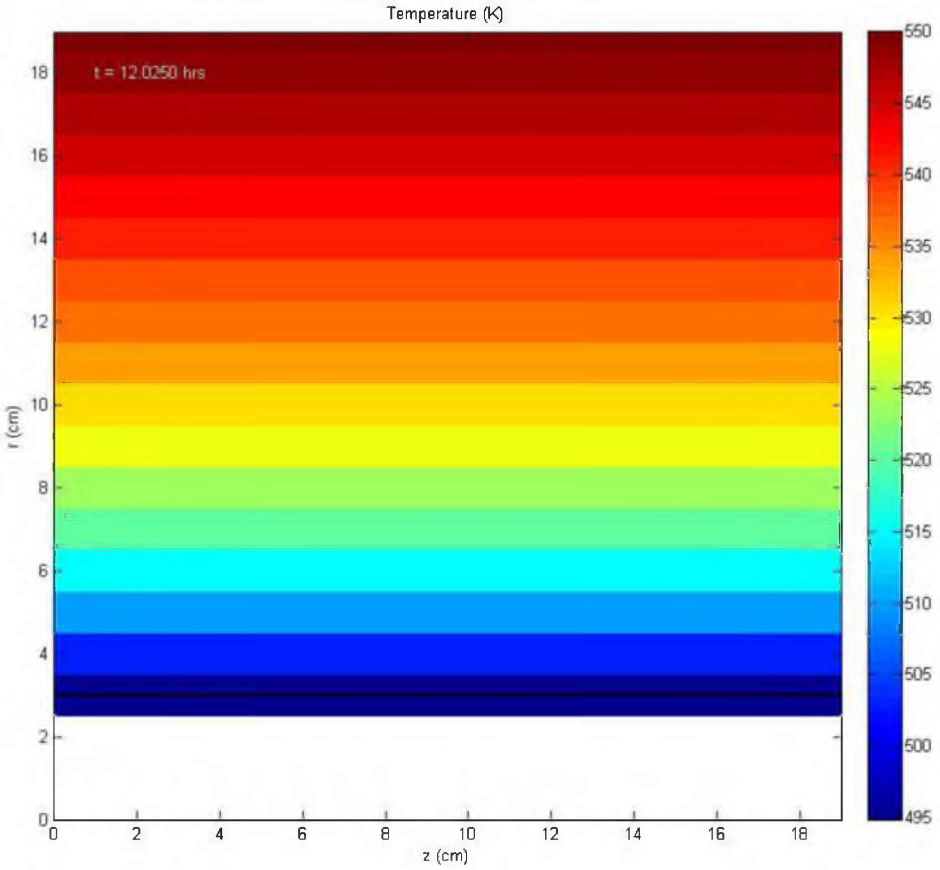

Figure D.8: Temperature profile illustrating a heat flux boundary.

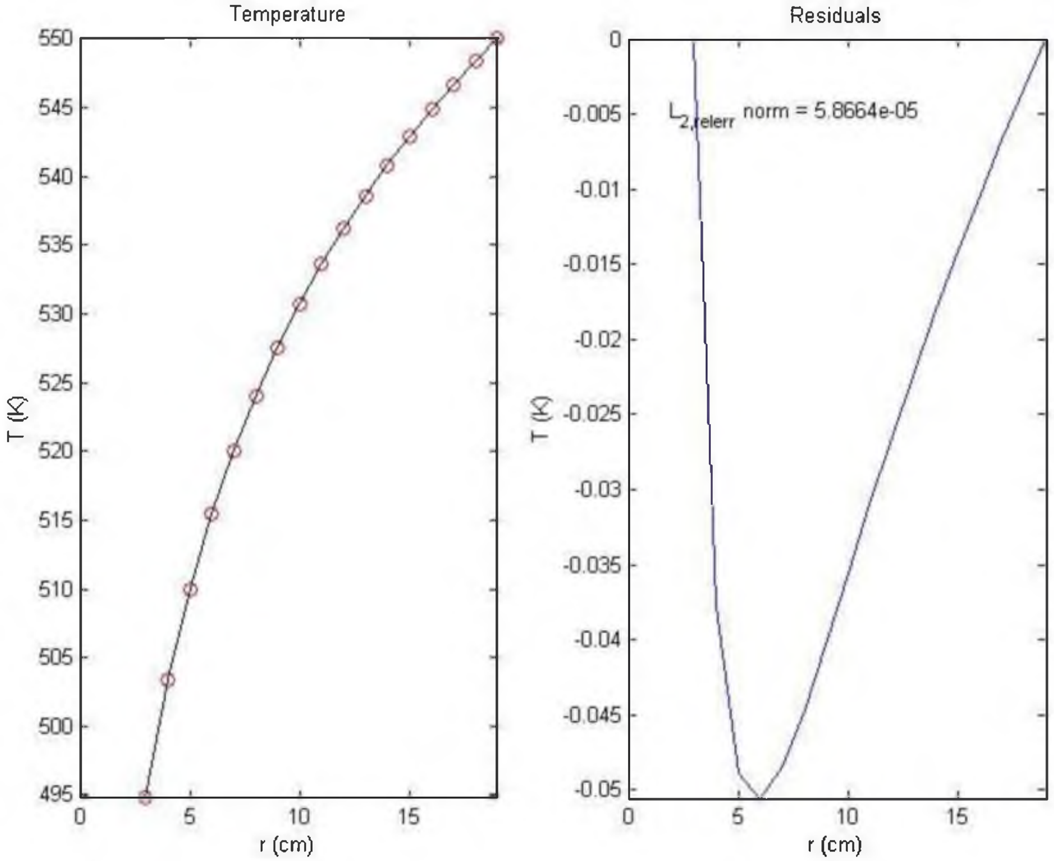

Figure D.9: A comparison of the given heat flux to the calculated heat flux.

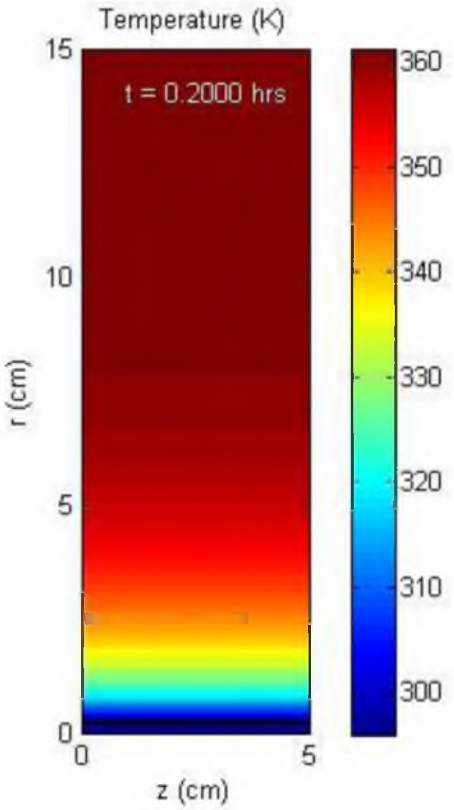

Figure D.10: Temperature profile at 0.2 hours.

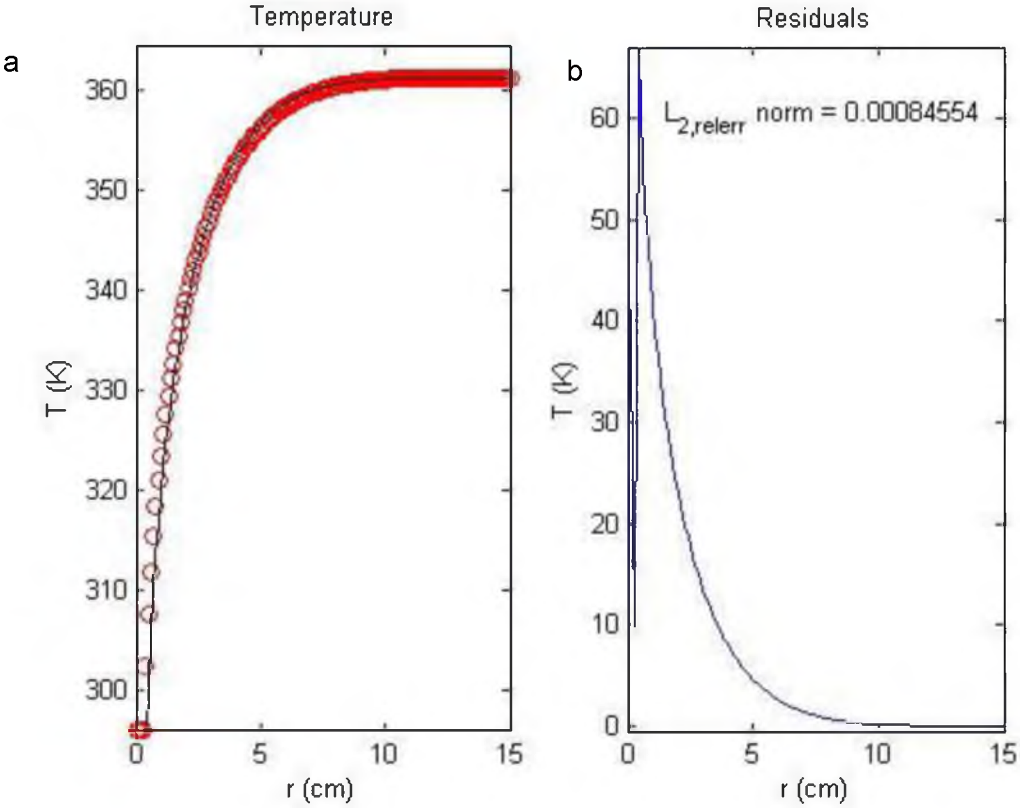

Figure D.11: Verification 5 results. a. Comparison of the analytical model (solid black line) and the FD model (red dots) b. The error along the radius.

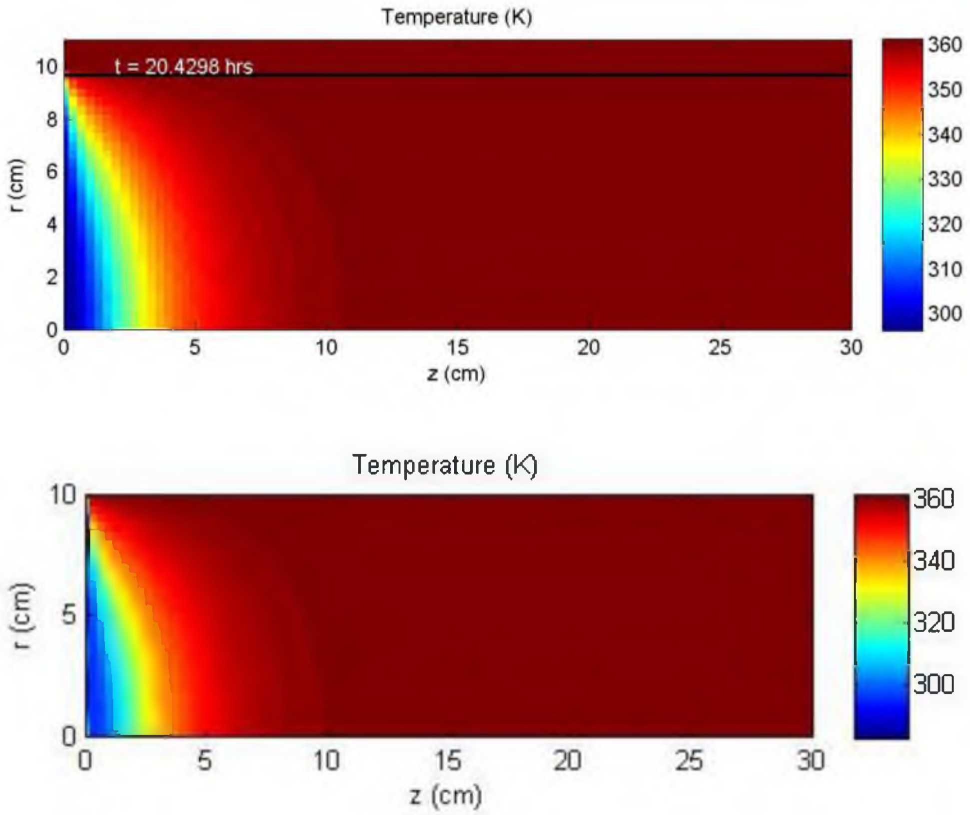

Figure D.12: Top) Finite difference model steady state solution, bottom) Analytical steady state solution

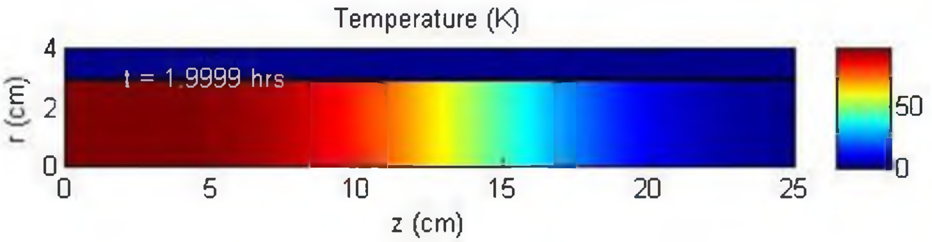

Figure D.13 Temperature profile at 2 hours of the finite difference model.

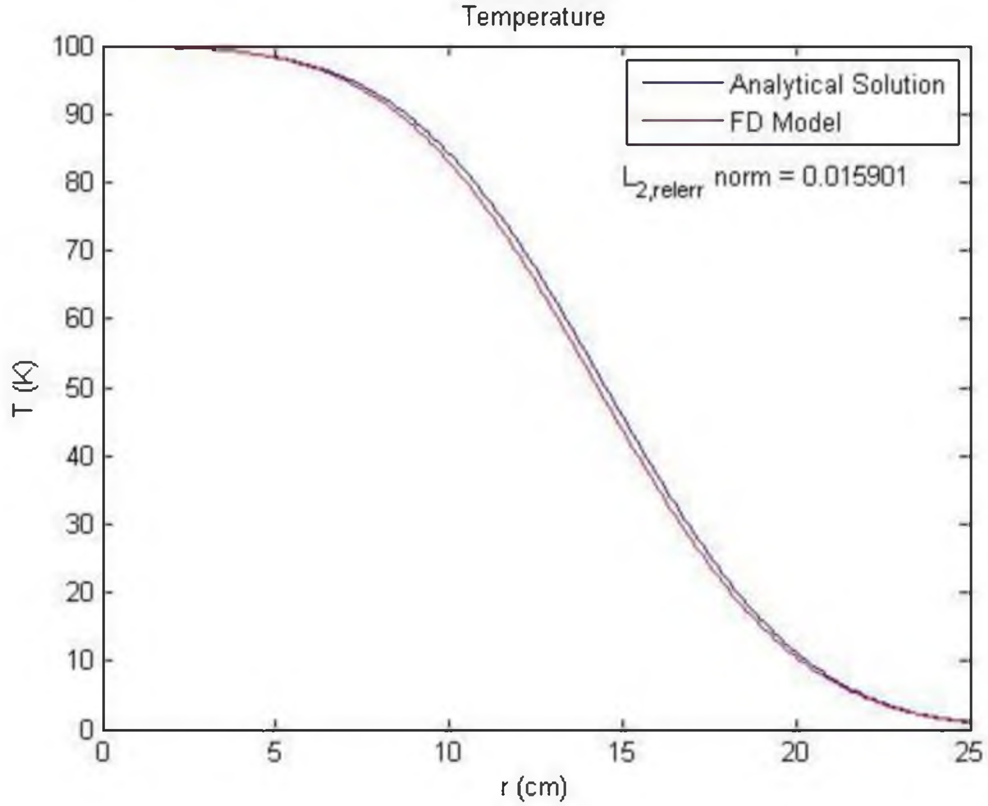

Figure D.14: Verification 7 results showing the analytical and simulated temperature profile in the r direction.

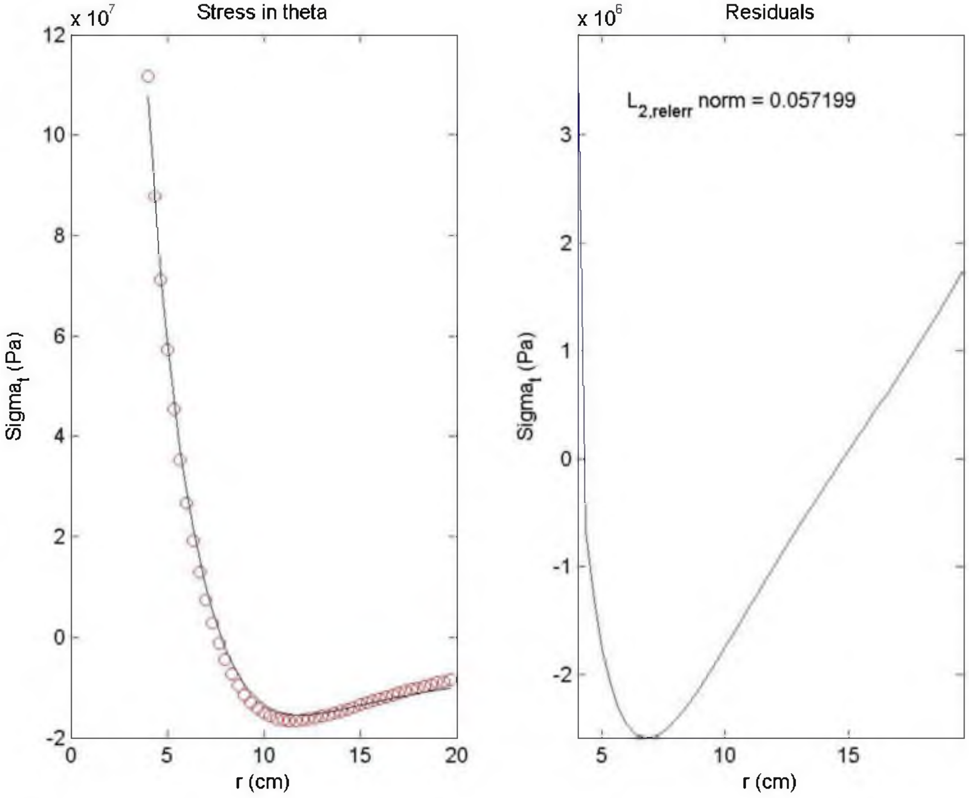

Figure D.15: Thermal tangential stress direction of a hollow cylinder

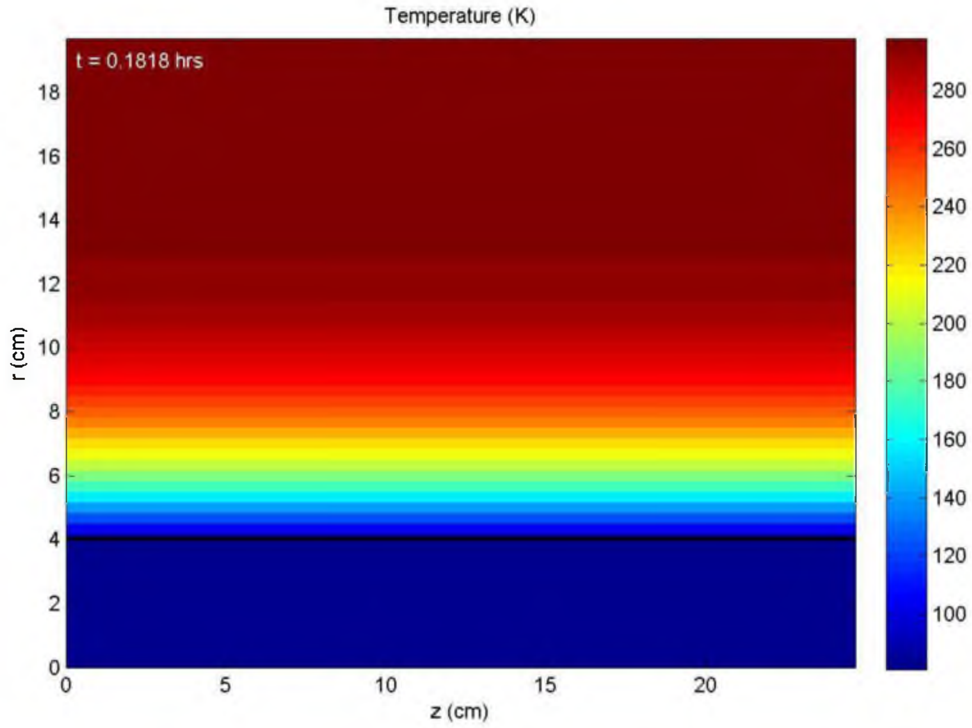

Figure D.16: Temperature distribution of the numerical model for verification 5.

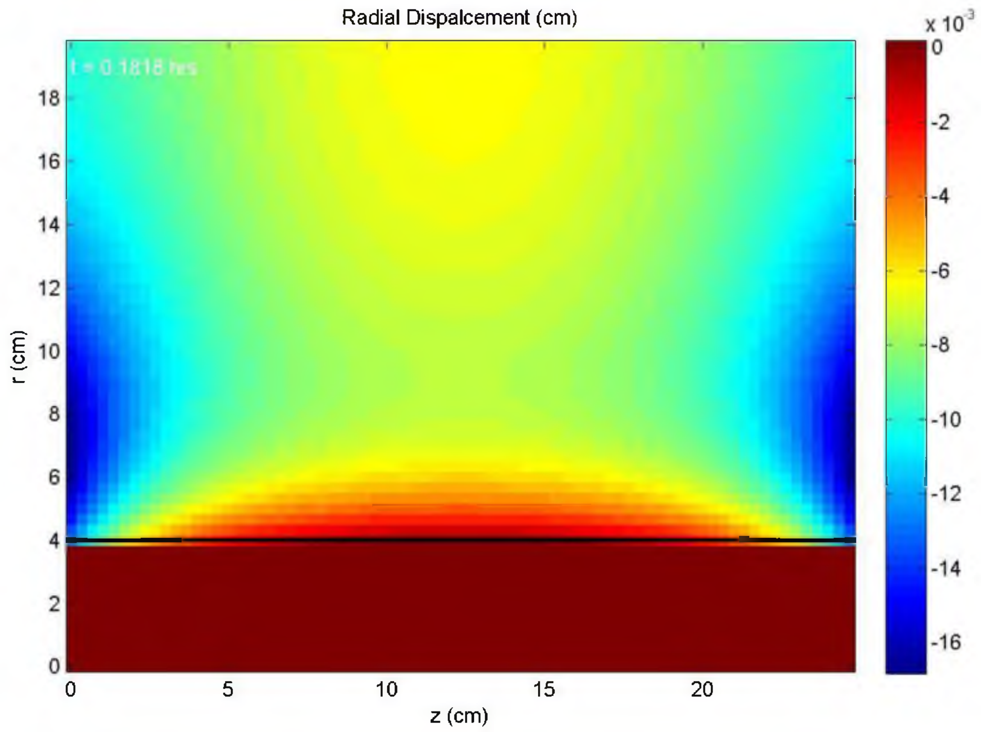

Figure D.17: Radial displacement of the numerical model for verification 5.

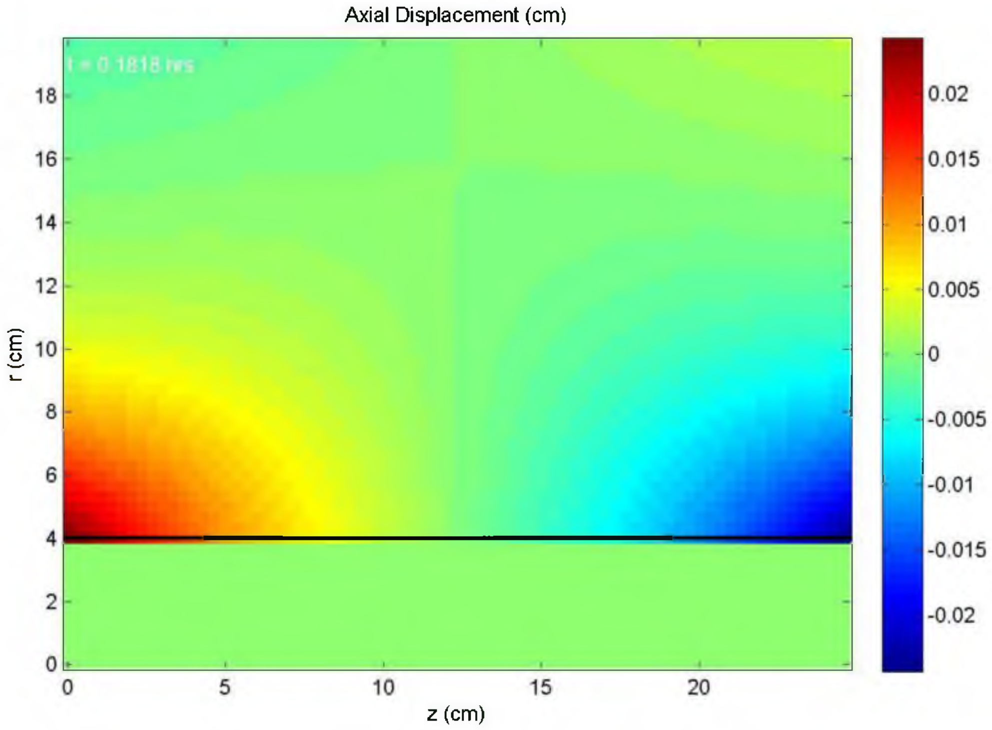

Figure D.18: Axial displacement of the numerical model for verification 5.

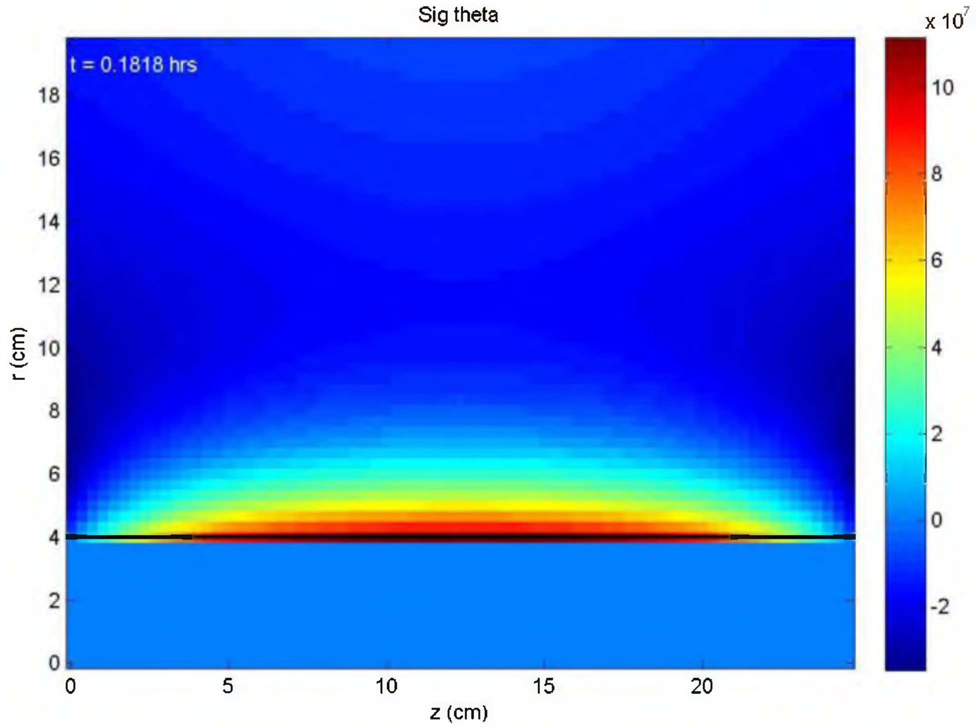

Figure D.19: Tangential stress of the numerical model for verification 5.

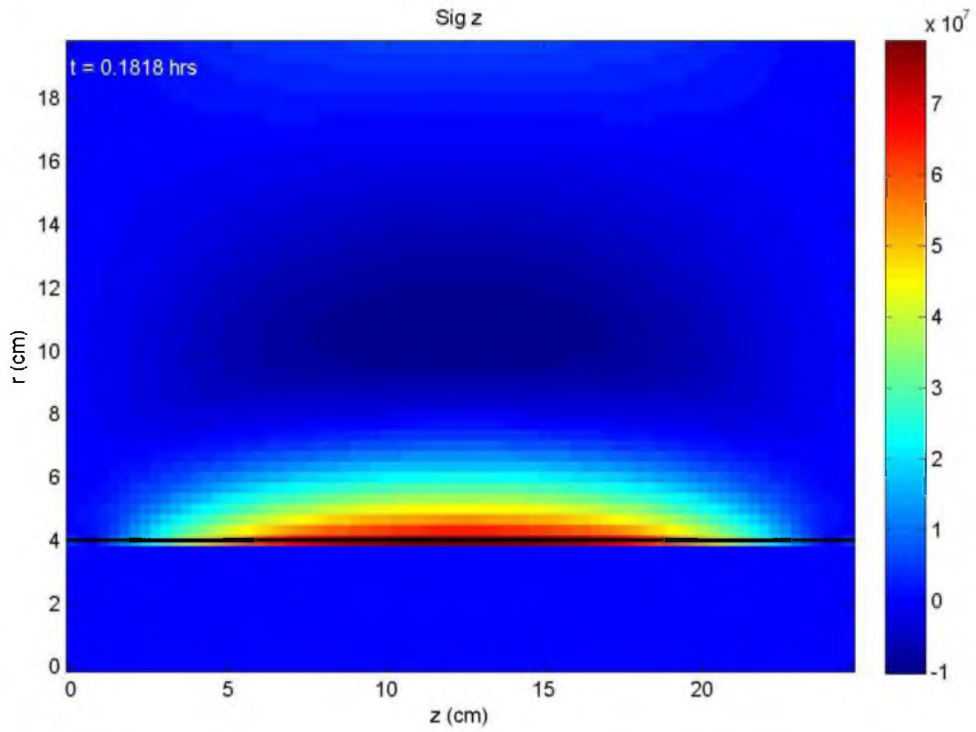

Figure D.20: Axial stress of the numerical model for verification 5.

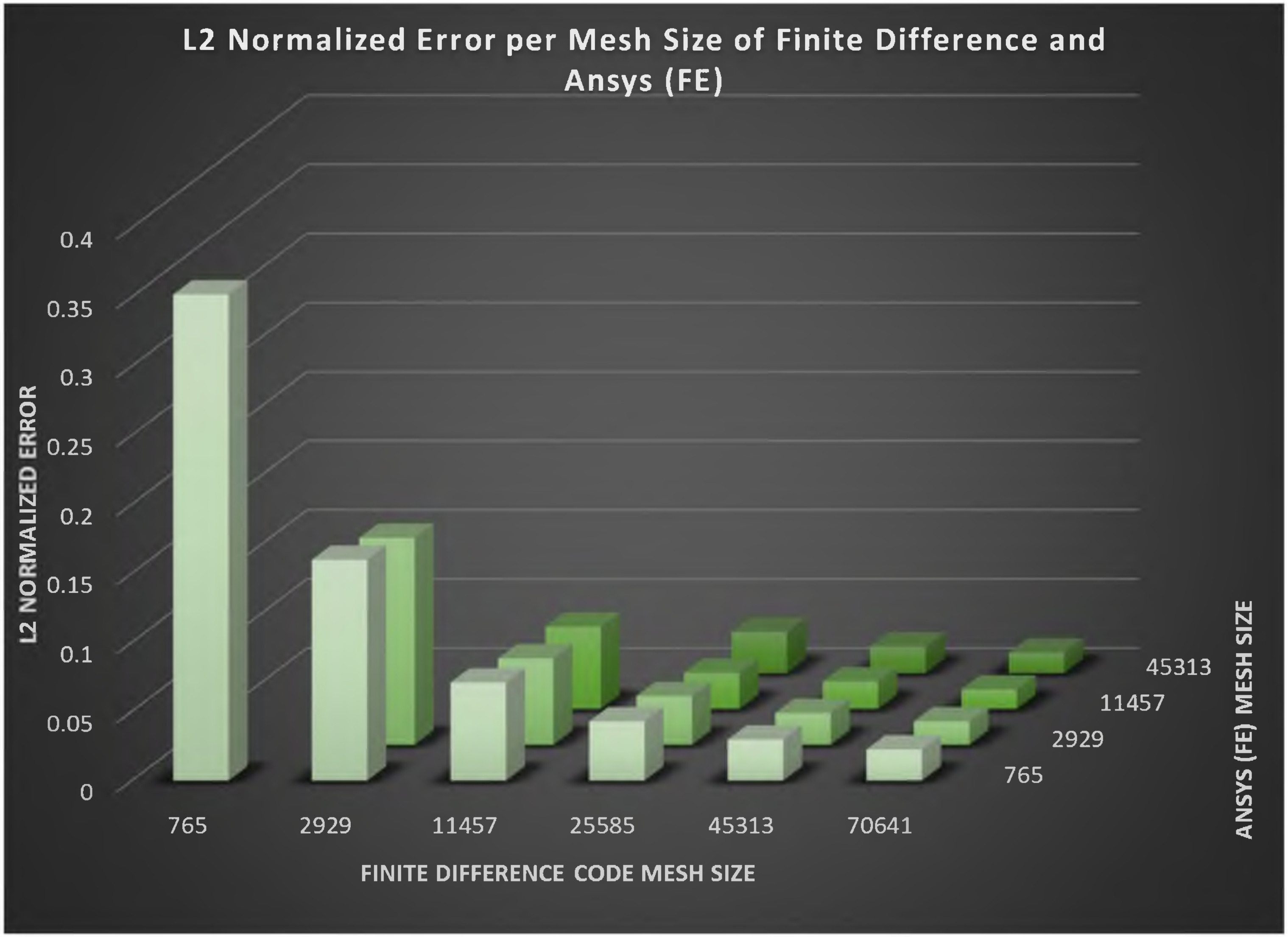

Figure D.21: Results of Ansys comparison with the numerical model.

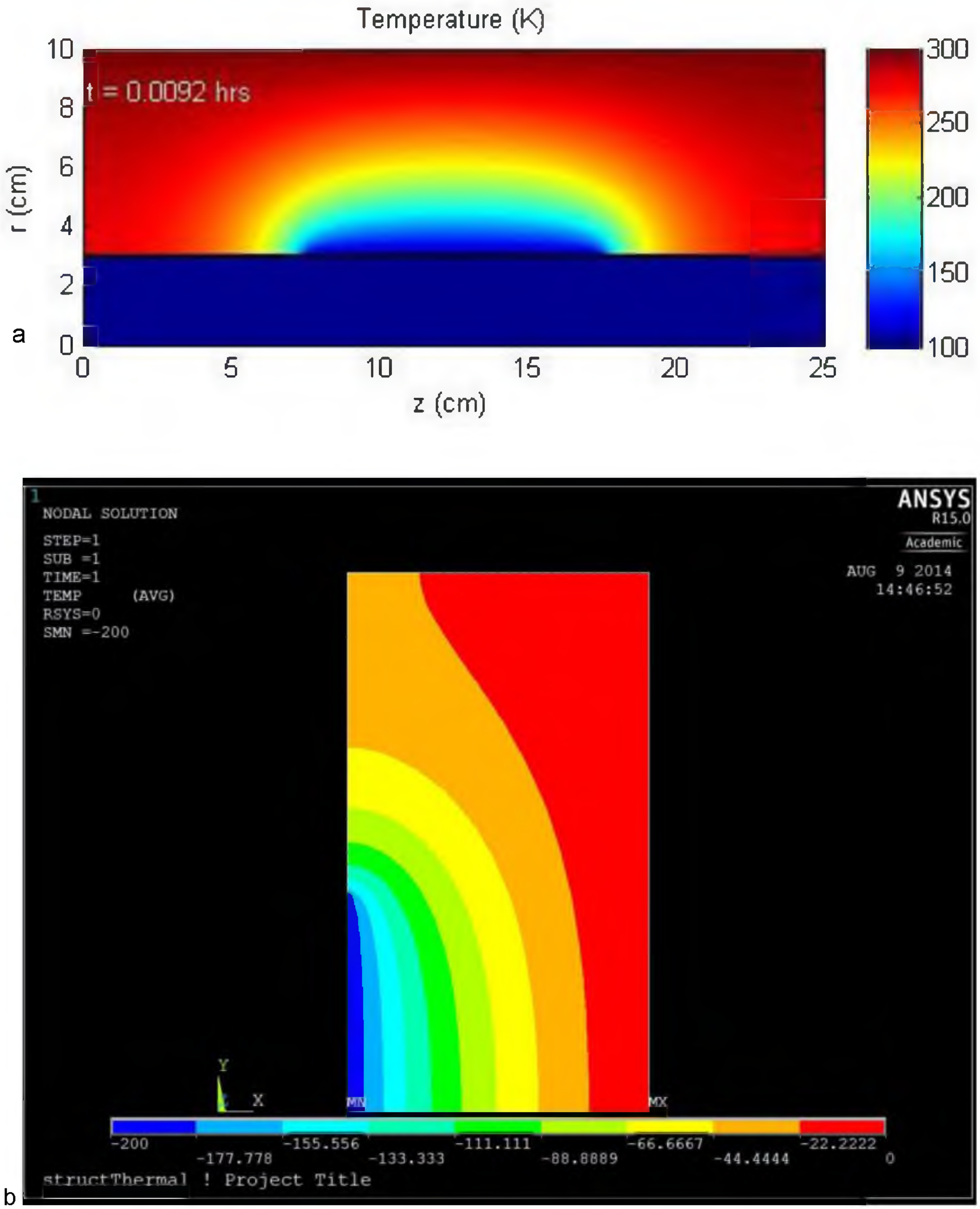

Figure D.22: Temperature profile of a. Numerical model, and b. Ansys simulation.

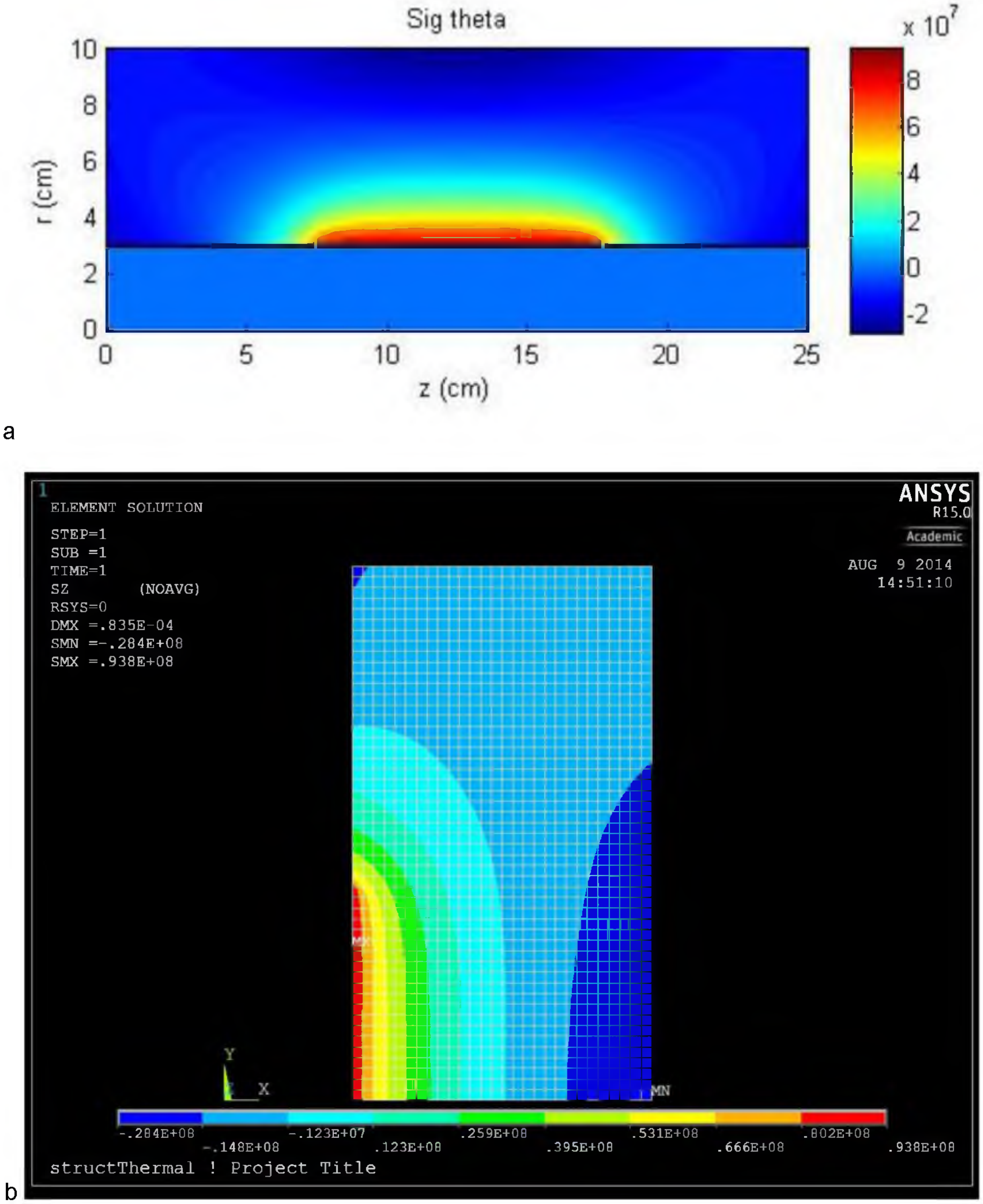

Figure D.23: Tangential stress profile of a. Numerical model, and b. Ansys simulation.

D.7 References

[1] Carslaw, H. S., and J. C. Jaeger, *Conduction of Heat in Solids*, 2nd ed., Oxford University Press, London, 1959, pp. 189.

[2] Carslaw, H. S., and J. C. Jaeger, *Conduction of Heat in Solids*, 2nd ed., Oxford University Press, London, 1959, pp. 220.

[3] Carslaw, H. S., and J. C. Jaeger, *Conduction of Heat in Solids*, 2nd ed., Oxford University Press, London, 1959, pp. 221.

[4] Incropera, F.P., and DeWitt, D.P., 2002, *Fundamentals of Heat and Mass Transfer*, 5th ed., John Wiley & Sons, Hoboken, pp. 106, Chap. 3.

[5] Jakob, M., 1962, *Heat Transfer*, Vol. 1, John Wiley & Sons, New York, pp. 459, Chap. 22.

[6] Walton, I., 2016, Research Professor, Energy and Geoscience Institute, private communication.

[7] Timoshenko, S.P., and Goodier, J.N., 1934, *Theory of Elasticity*, 3rd ed., McGraw-Hill Book Company, San Francisco, pp. 448, Chap. 13.